ADVANCED STEEL CONSTRUCTION

an International Journal

Volume 1 Number 2 September 2005

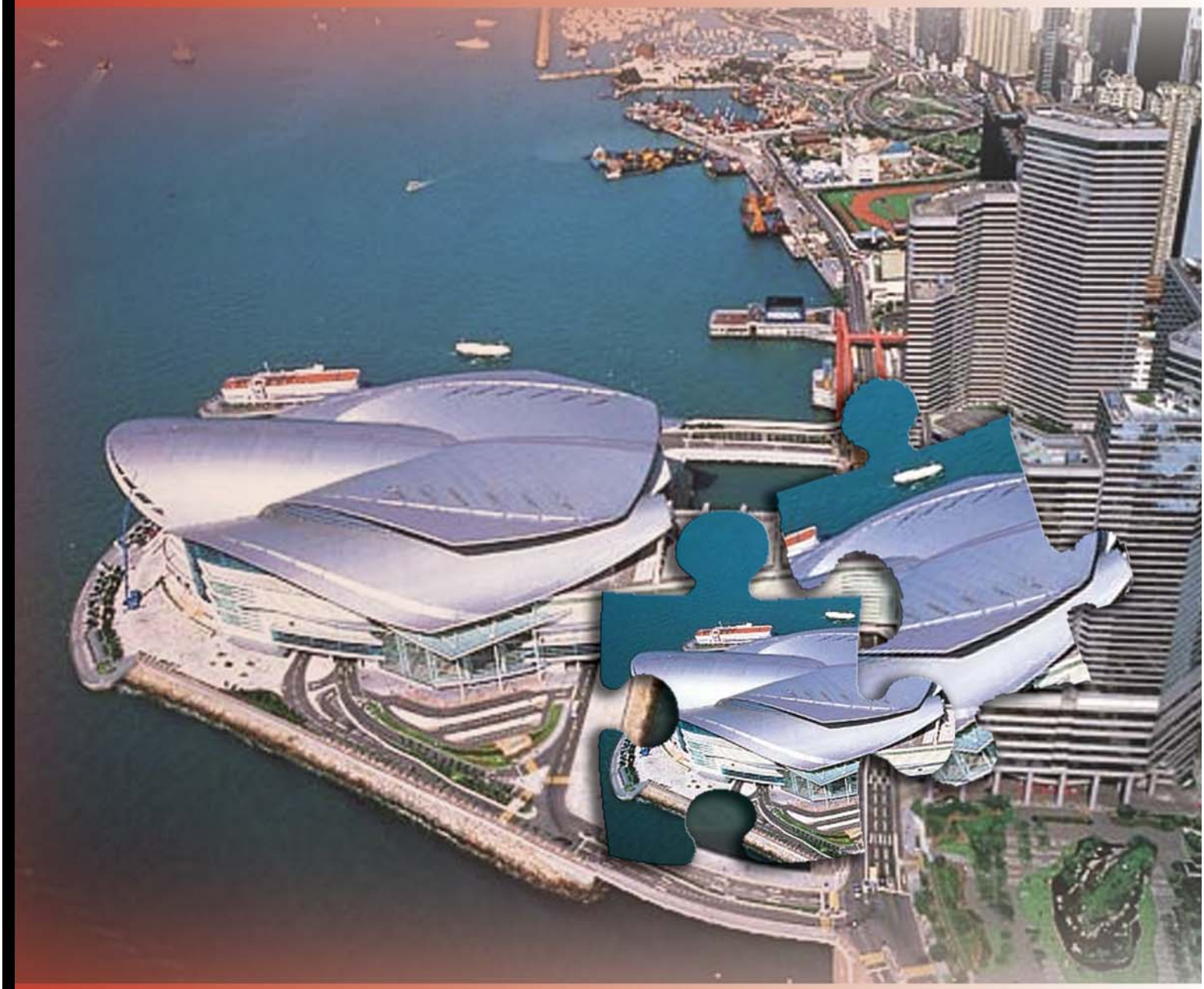

Advanced Steel Construction
an international journal

General Information
Advanced Steel Construction, an international journal

Aims and scope

The International Journal of Advanced Steel Construction provides a platform for the publication and rapid dissemination of original and up-to-date research and technological developments in steel construction, design and analysis. Scope of research papers published in this journal includes but is not limited to theoretical and experimental research on elements, assemblages, systems, material, design philosophy and codification, standards, fabrication, projects of innovative nature and computer techniques. The journal is specifically tailored to channel the exchange of technological know-how between researchers and practitioners. Contributions from all aspects related to the recent developments of advanced steel construction are welcome.

Instructions to authors

Submission of the manuscript. Authors may submit three double-spaced hard copies of manuscripts together with an electronic copy on a diskette or cd-rom in an editable format (MS Word is preferred). Manuscripts should be submitted to the regional editors as follows for arrangement of review.

Asian Pacific , African and organizing editor :	Professor S.L. Chan
American editor :	Professor W.F. Chen
European editor :	Professor R. Zandonini

All manuscripts submitted to the journal are highly recommended to accompany with a list of four potential reviewers suggested by the author(s). This list should include the complete name, address, telephone and fax numbers, email address, and at least five keywords that identify the expertise of each reviewer. This scheme will improve the process of review.

Style of manuscript

General. Author(s) should provide full postal and email addresses and fax number for correspondence. The manuscript including abstract, keywords, references, figures and tables should be in English with pages numbered and typed with double line spacing on single side of A4 or letter-sized paper. The front page of the article should contain:

a) a short title (reflecting the content of the paper);
b) all the name(s) and postal and email addresses of author(s) specifying the author to whom correspondence and proofs should be sent;
c) an abstract of 100-200 words; and
d) 5 to 8 keywords.

The paper must contain an introduction and a conclusion. The length of paper should not exceed 25 journal pages (approximately 15,000 words equivalents).

Tables and figures. Tables and figures including photographs should be typed, numbered consecutively in Arabic numerals and with short titles. They should be referred in the text as Figure 1, Table 2, etc. Originally drawn figures and photographs should be provided in a form suitable for photographic reproduction and reduction in the journal.

Mathematical expressions and units. The Systeme Internationale (SI) should be followed whenever possible. The numbers identifying the displayed mathematical expression should be referred to in the text as Eq. (1), Eq. (2).

References. References to published literature should be referred in the text, in the order of citation with Arabic numerals, by the last name(s) of the author(s) (e.g. Zandonini, R.). References should be in English with occasional allowance of 1-2 exceptional references in local languages and reflect the current state-of-technology. Journal titles should be abbreviated in the style of the Word List of Scientific Periodicals. References should be cited in the following style.

Journal: Chen, W.F. and Kishi, N., “Semi-rigid steel beam-to-column connections, data base and modeling”, Journal of Structural Engineering, ASCE, 1989, 115(1), pp.105-119.

Book: Chan, S.L. and Chui, P.P.T., "Non-linear static and cyclic analysis of semi-rigid steel frames", Elsevier Science, 2000, pp.336.

Proceedings: Zandonini, R. and Zanon, P., “Experimental analysis of steel beams with semi-rigid joints”, Proceedings of International Conference on Advances in Steel Structures, Hong Kong, 1996, vol. 1, pp.356-364.

Proofs. Proof will be sent to the corresponding author to correct any typesetting errors. Alternations to the original manuscript at this stage will not be accepted. Proofs should be returned within 48 hours of receipt by Express Mail, Fax or Email.

Copyright. Submission of an article to “Advanced Steel Construction” implies that it presents the original and unpublished work, and not under consideration for publication nor published elsewhere. On acceptance of a manuscript submitted, the copyright thereof is transferred to the publisher by the Transfer of Copyright Agreement and upon the acceptance of publication for the papers, the corresponding author must sign the form for Transfer of Copyright.

Permission. Quoting from this journal is granted provided that the customary acknowledgement is given to the source.

Page charge and Reprints. There will be no page charges if the length of paper is within the limit of 25 journal pages. A total of 30 free offprints will be supplied free of charge to the corresponding author. Purchasing orders for additional offprints can be made on order forms which will be sent to the authors. These instructions can be obtained at the Hong Kong Institute of Steel Construction, Journal website: http://www.hkisc.org

The International Journal of Advanced Steel Construction is published quarterly by non-profit making learnt society, The Hong Kong Institute of Steel Construction, c/o Department of Civil & Structural Engineering, The Hong Kong Polytechnic University, Hung Hom, Kowloon, Hong Kong.

The Hong Kong Institute of Steel Construction
HKISC
c/o Department of Civil and Structural Engineering,
The Hong Kong Polytechnic University,
Hunghom, Kowloon, Hong Kong, China.
Tel: 852- 2766 6070 Fax: 852- 2334 6389
Email: *ceslchan@polyu.edu.hk* Website: *http://www.hkisc.org/*

Advanced Steel Construction
an international journal

VOLUME 1/ NUMBER 2 SEPTEMBER 2005

Foreword for the Inaugurate Issue of the International Journal of Advanced Steel Construction

As clearly stated by professor Chen in the opening remarks to the first issue, the difficult mission of the Journal can be summarized in two words: innovation and creativity in steel construction. Research, technology and codes are considered in fulfilling this goal in the areas of design, analysis and practice.

It is not by chance that such an ambitious goal is defined for a new journal, which was born with Asia, and in particular China, in mind as the reference geographical area. The tremendous economical growth in this area represents an extraordinary challenge for the construction world. A response should be given, which should conjugate structural reliability with effectiveness and efficiency in time and cost. Such a requirement urges towards innovation and creativity and, even more important, towards the practical use of them. It is hence of great interest to the Journal to disseminate knowledge and information, which can find a significant echo within the Asian scientific community.

This second issue proceeds well along this general perspective, and deals with topics, which should be carefully considered by scientists, engineers and builders operating in the steel construction world. The papers cover important problems in fields such as frame analysis, new sections, new materials in composite systems and fatigue. Moreover, recent trends in seismic codes are presented, with reference to the 2005 Specifications of the American Institute of Steel Construction. Despite Code recommendations, by their very nature, can not be based on the most recent research findings, they provide a useful indicator of the evolution in progress in the 'philosophical' perspective, which lies behind design methods and rules.

Performance based design appears to be a powerful approach, which allows combination of reliability with economical efficiency. The basic concept has found application so far mainly in the field of seismic engineering, and, more in general, to the design of structures subject to accidental actions such as fire and explosion. Its extension to the design of structural systems under 'any' loading condition is welcome. Besides, it is foreseeable: the times are mature for that. Availability of advanced analysis methods is a necessary pre-requisite for performance based design of frame structures. They enable refined approximation of the system performance, catching all the various phases and the attainment of the relevant limit states. Despite some recent Codes, such as the Eurocode 3, provide general guidelines and data for applying nonlinear FE analysis, a greater effort is necessary to make the use of these methods more attractive and popular among practicing engineers.

Two interesting papers contribute to this line of development. The first by Aguero and Pallares presents a simplified second-order elastic analysis method to be adopted in association with equivalent geometric imperfections. The second by Chan and Chen elaborates on the comparison with traditional prescriptive design approaches and points out the advantages of advanced analysis in terms of both overall reliability and cost efficiency of the structure. Furthermore, it provides evidence of the general Authors' considerations by means of two remarkable examples, including an important recently constructed project.

Innovation in the cross-section of industrially fabricated profiles is nowadays fairly rare. However, oval hollow sections recently emerged as a new 'design option' enabling combination of architectural appeal and structural efficiency. However, their use is somehow hampered by the lack a validated set of specific design guidelines. The paper by Gardner reports on a wide series of numerical and experimental studies on elliptical sections subject to compression or in-plane bending. The results already available well agree with the preliminary design rules considered by the Author. Further work is needed for the full validation of these rules. However, the indications provided in the paper represent an important step towards a wider application of this new 'family' of sections.

Composite structural systems making efficient use of complementary properties of different materials and/or subsystems can be considered the core development, which to a large extent characterizes the future of the construction field. The design of new structural systems and the retrofitting of existing ones take both advantage of composite action. Of particular interest is the use of CFRP in strengthening steel structures. Design requires full understanding of the interaction mechanism based on the bond between steel and CFRP. The knowledge of this central aspect is not yet exhaustive, with particular reference to the potential range of relative stiffness properties of the two materials. The contribution by Fawzia et al. focuses on the influence of the CFRP modulus on the bond length and the ultimate capacity, and includes a prediction method proposed by the Authors, which appears to be rather accurate at least in the cases examined.

Finally, the paper by Xiong et al. deals with the relation between the elastic-plastic near crack tip response and the fatigue crack propagation, and demonstrates the significance of the plastic strain in compression. The ability of mastering the various aspects of fatigue in design is more and more important, due to its influence on the optimal design of a wide range of steel structures.

It is hence possible to conclude that all the papers in this issue fulfill the basic requirements inherently associated with the mission of the Journal.

R. Zandonini
Professor of Structural Engineering
University of Trento
Trento, Italy

[Blank Page]

MAJOR REVISIONS OF THE 2005 AISC SEISMIC CODE

I.H. Chen[1] and W.F. Chen[2]

[1]*Senior Project Engineer, DESIMONE Consulting Engineer, San Francisco, CA, USA*

[2]*Dean, College of Engineering, University of Hawaii, Honolulu, HI, USA*

Abstract: In this paper, the major changes of the 2005 Seismic Provisions for Structural Steel Buildings Part I will be summarized and discussed. The major topics include: Introduction of "Demand Critical Welds" and "Protected Zones"; Expansion of Scope; Integration of ASD into LRFD provisions; Introduction of New Systems and Appendices; General Revisions that applied to all Seismic Load Resisting Systems; and Specific Revisions for the Existing Systems.

1. INTRODUCTION

The AISC Seismic Provisions for Structural Steel Buildings, hereafter referred to as Seismic Provisions [1,2], which included as part of the AISC Load and Resistance Factor Design (LRFD) Specification for Structural Steel Buildings, hereafter referred to as Specification [3,4], are intended to cover the common design criteria in routine office practice under seismic demands. As new research becomes available, professional practice experiences accumulate and products gain popularity (New Structural Systems), the newly updated version of *Seismic Provisions* would become available. The languages of the 2005 Seismic Provisions are revised to be consistent with (the CPRP document) ANSI/AISC 358. The major changes of the 2005 Seismic Provisions for Structural Steel Buildings Part I-Structural Steel Buildings can be grouped into the following aspects: (1) Introduction of New Terms; (2) Scope Expansion; (3) Integration of ASD [5] into LRFD provisions; (4) Introduction of New Systems and Appendices; (5) General Revisions that applied to all Seismic Load Resisting Systems; and (6) Specific Revisions for each Existing Systems.

The new 2005 Seismic Provisions introduce new terms such as "Demand Critical Welds" and "Protected Zones" to identify critical areas and their associated requirements in seismic design. Also, the scope of the Seismic Provisions is expanded from "the design and construction" to "the design, fabrication, and erection" of structural members and connections in the seismic load resisting systems (SLRS). The allowable stress design (ASD) alternative (previous part III of 2002 Seismic Provision) has been incorporated into Part I along with Load and Resistance Factor Design (LRFD). In addition, two new systems and 3 new appendices are introduced. They include Buckling-Restrained Braced Frames (BRBF), Special Plate Shear Walls (SPSW), Seismic Design Coefficients and Approximate Period Parameters, Qualifying Cyclic Tests of Buckling-Restrained Braces, and Welding Provisions [6]. Furthermore, changes that applied to all SLRS and each existing systems are provided. These aspects will be discussed in the following sections. The provisions cited from the 2005 code in "exact code language" will be <u>underlined</u>.

2. INTRODUCTION OF NEW TERMS

In order to clarify the intention of certain seismic requirements, new terms are introduced in the new 2005 Seismic Provision. Among them, "Demand Critical Welds" and "Protected Zone" are most significant.

2.1 Demand Critical Welds

The newly introduced section replaced the "Additional Requirements in Special Moment Frames (SMF) and Intermediate Moment Frames (IMF)" for Welded Joints of previous Seismic Provisions. Since these welds are required to sustain significant demand from moment connection of SMF and IMF under inelastic deformation, the provisions emphasize the toughness properties of welds. Basically the same requirements applied, except for structures with service temperatures lower than 50 ^{o}F (10 ^{o}C), the qualification temperature is clarified as 20 ^{o}F (11 ^{o}C) above the lowest anticipated service temperature, or at a lower temperature. The Lowest Anticipated Service Temperature (LAST) is the lowest 1-hour average temperature with a 100-year mean recurrence interval.

Further, SMAW electrodes classified by AWS A5.1 as E7018 and E8018, and GMAW solid electrodes are exempted from production lot testing when the CVN toughness of the electrode equals or exceeds 20 ft-lbs (27 J) at a temperature not exceeding –20 ^{o}F (-29 ^{o}C) as determined by AWS classification test methods. The manufacture's certificate of compliance shall be considered sufficient evidence of meeting this requirement.

2.2 Protected Zone

Protected zone is defined as Area of members in which limitations apply to fabrication and attachments. In other words, it is the zone expected to undergo inelastic deformation, such as plastic hinging zone and beam-column Panel Zone. The newly introduced section combines the old sections "Other Connections" and "Discontinuities" for Welded Joints. In general, provisions are made to avoid discontinuities cause be welding, rapid change of section, penetrations, or construction caused flaws.

3. SCOPE EXPANSION

The applicability of the Seismic Provisions has been modified to depend on the response modification coefficient, R>3, (as specified in the applicable building code) regardless of seismic design category. In the absence of local building code, the ASCE [7,8] should govern. Additionally, the scope of the Seismic Provisions is expanded from "the design and construction" to "the design, fabrication, and erection" of structural members and connections in the seismic load resisting systems (SLRS). As a result a new section "Contract Documents, Shop Drawings and Erection Drawings" is added.

3.1 Contract Documents, Shop Drawings and Erection Drawings

In general all contract documents (structural design drawings and specifications), shop and erection drawings shall include items required by the Specification and the following, as applicable:

(1) Designation of the members and connections that are part of the seismic load resisting system.
(2) Connection material specifications and sizes. (Shop drawings do not required sizes; Erection drawings required field conditions.)

(3) Locations of demand critical welds.
(4) Locations and dimensions of protected zones
(5) Welding requirements as specified in Appendix W. (Erection drawings required field conditions.)

Additional requirements for each of the three documents are listed in Section 3.1.1 to 3.1.3.

3.1.1 Structural Design Drawings and Specifications:

(1) Designation of the seismic load resisting system (SLRS)
(2) Configuration of the connections
(3) Lowest anticipated service temperature (LAST) of the steel structure, if the structure is not enclosed and maintained at a temperature of 50 ^{o}F (10 ^{o}C) or higher.
(4) Locations where gusset plates are to be detailed to accommodate inelastic rotation.

For connections and applications not specifically addressed by the Provisions (Code of Standard Practice listed in Specification), the appropriate requirements should be included, such as nondestructive testing requirements beyond Appendix Q, bolt hole fabrication requirements, bolting requirements, and welding requirements.

3.1.2 Shop Drawings:

(1) Gusset plates drawn to scale when they are detailed to accommodate inelastic rotation.

For connections and applications not specifically addressed by the Provisions, the appropriate requirements should be included, such as bolt hole fabrication requirements, bolting requirements, and welding requirements.

3.1.3 Erection Drawings:

(1) Locations of pretensioned bolts.

For connections and applications not specifically addressed by the Provisions, the appropriate requirements should be included, such as bolting requirements, and welding requirements.

4. ALLOWABLE STRESS DESIGN (ASD) INTEGRATION

In the past, the allowable stress design (ASD) alternative [2,5] has always been documented separately as Part III of Seismic Provisions, while the Part I is for LRFD. However, in the 2005 version, the ASD has been incorporated into Part I along with Load and Resistance Factor Design (LRFD). Generally the conversion factors from strength level to allowable stress level is 1.5 or 0.67 (=1/1.5), except certain controlling limit states “1.67” is specified. Please see Table 4.1 for tabulated conversions between LRFD and ASD when 1.67 Factor is applied.

Table 4.1. LRFD and ASD Conversion Factors

Code Section	Description	LRFD	ASD
8.3	Columns Strength	$P_u/\phi_c P_n > 0.4$, $\phi_c = 0.9$	$\Omega_c P_a/P_n > 0.4$, $\Omega_c = 1.67$
12.3	Required Axial Strength in Chord of STMF	$0.45\phi P_n$, $\phi = 0.9$	$0.45P_n/\Omega$, $\Omega = 1.67$
15.2b	Link Shear Strength of EBF	$\phi_v V_n$, $\phi_v V_{pa}$, $2\phi_v M_{pa}/e$, $\phi_v = 0.9$	V_n/Ω_v, V_{pa}/Ω_v, $2(M_{pa}/e)/\Omega_v$, $\Omega_v = 1.67$
16.2a	Brace Design Axial Strength of BRBF	ϕP_{ysc}, $\phi = 0.9$	P_{ysc}/Ω, $\Omega = 1.67$
17.2	SPSW Web Shear	$\phi V_n = 0.42F_y t_w L_{cf} \sin 2\alpha$, $\phi = 0.9$	$V_n = 0.42F_y t_w L_{cf} \sin 2\alpha/\Omega$, $\Omega = 1.67$

Please note that when 1.67 is specified for ASD conversion, the reduction factor $\phi = 0.9$ always accompanied. In other words, 1.5 conversion factor still prevails, because 1.67 = 1.5/0.9.

5. INTRODUCTION OF NEW SYSTEMS AND APPENDICES

Two new structural systems and 3 new appendices are introduced into the 2005 Seismic Provisions. The two new structural systems are "Buckling-Restrained Braced Frames (BRBF)" and "Special Plate Shear Walls (SPSW)". The three new appendices are "Seismic Design Coefficients and Approximate Period Parameters", "Qualifying Cyclic Tests of Buckling-Restrained Braces", and "Welding Provisions". Among them, the "Welding Provisions" is non-mandatory and will later be replaced by AWS D1.8. These new sections will be discussed in the following sections.

5.1 Buckling-Restrained Braced Frames (BRBF)

Buckling-restrained braced frames are a special class of concentrically braced frames, where the bracing members can yield in compression without buckling, see Figure 1. Therefore, these braces can dissipate energy through stable tension-compression yield cycles.

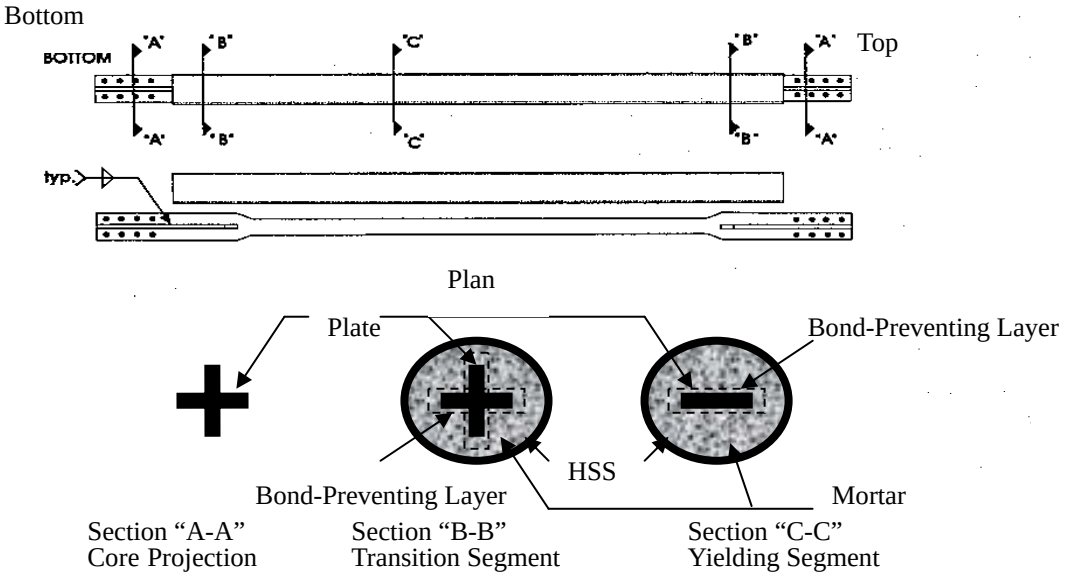

Figure 1. Details of a Buckling Restrained Brace

Bracing members shall be composed of a structural steel core and a system that restrains the steel core from buckling. The brace design axial strength should solely rely on the steel core, $\phi P_{ysc}=F_y A_{sc}$, where A_{sc} is the net area of steel core. When steel core's plates are 2" (50mm) or thicker, notch toughness requirements for heavy sections in the code should apply. Buckling-restraining system shall ensure no buckling of steel core, including both local and overall buckling, for deformations corresponding to 2.0 times the design story drift. Bracing connections shall have minimum strength of 1.1 times the adjusted brace strength in compression. The qualifying cyclic tests should conform to Appendix T.

For bracing configurations, V-type and inverted-V-type shall be allowed only if 1) the supporting beams are continuous between columns and laterally brace at both flanges; 2)all gravity loadings including dead and live load can be supported without the braces. K-type braced frames are not permitted.

For beams and columns, they are to be designed for standard load combinations and meet typical width-thickness limitations. Splices shall have shear strength and 50% flexural strength of the smaller connected member determined from the limit state of yielding.

5.2 Special Plate Shear Walls (SPSW)

Special Plate Shear Walls are constructed of slender unstiffened steel plates (Webs) connected to surrounding horizontal and vertical boundary elements, see Figure 2. (i.e. HBEs and VBEs). All HBEs are rigidly connected to VBEs with moment connections able to develop the expected plastic moment of the HBEs. SPSW are designed to withstand significant inelastic deformations in the webs under design earthquakes. While the HBEs and VBEs adjacent to the webs are designed to remain essentially elastic under the maximum forces that can be generated by the fully yielded webs, except that plastic hinging at the ends of the HBEs is permitted. In order to achieve the intended behavior, the criteria for Webs, Boundary Elements, and Connections are provided.

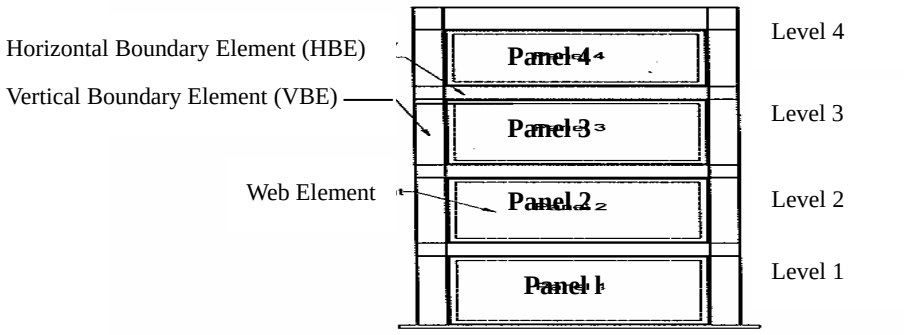

Figure 2. Schematic of Special Plate Shear Walls

5.2.1 Webs

The aspect ratio of web panel Length to Height, L/h, shall be limited to 0.8 to 2.5. Any openings in webs shall be bounded on all sides by HBE's and VBE's extending the full width and height of the panel respectively. The panel shear strength ϕV_n (LRFD) and V_n/Ω (ASD) shall be determined as

$V_n = 0.42F_y t_w L_{cf} \sin 2\alpha$, $\phi = 0.9$, $\Omega = 1.67$

where

t_w = thickness of web, in. (mm)

L_{cf} = clear distance between VBE flanges, in.

α is the angle of web yielding in radians, as measured relative to the vertical, and it is given by:

$$\tan^4 \alpha = \frac{1 + \frac{t_w L}{2A_c}}{1 + t_w h\left(\frac{1}{A_b} + \frac{h^3}{360 I_c L}\right)}$$

h = distance between HBE centerlines, in. (mm)

A_b = cross-sectional area of a HBE, in.^{2} (mm^2)

A_c = cross-sectional area of a VBE, in.^{2} (mm^2)

I_c = moment of inertia of a VBE taken perpendicular to the direction of the web plate line, in.^{4} (mm^4)

L = distance between VBE centerlines, in. (mm)

5.2.2 Horizontal and Vertical Boundary Elements

The combination of HBEs and VBEs can be used as the moment frame for a dual system. Therefore, the beam-column moment ratio requirement of Special Moment Frames (SMF) shall be met for all HBE/VBE intersections without considering the effects of webs. Same panel zone and width-thickness requirements as SMF shall be met.

HBE's shall be laterally braced at all intersections with VBE's and at a spacing not to exceed $0.086 r_y E_s / F_y$ (same as SMF). The minimum required brace strength shall be 2% of flange nominal strength.

The required VBE's strength shall meet seismic column requirements, except the expected yield strength, in tension, of the web calculated at an angle α should also be considered. The stiffness of VBE shall have moment of inertia about an axis perpendicular to the direction of the web plate, I_c, not be less than $0.00307 t_w h^4 / L$.

5.2.3 Connections

Connections of Webs to Boundary Elements shall have required strength of the expected yield strength, in tension, of the web calculated at angle α.

Connections of HBE-to-VBE shall satisfy the requirement of Ordinary Moment Frame (OMF), except the required shear strength V_u. The required shear strength V_u shall not be less than the shear corresponding to moments at each end equal to $1.1 R_y M_p$ (LRFD) of $(1.1/1.5) R_y M_p$ (ASD), as appropriate, together with the shear resulting form the expected yield strength in tension of the webs yielding at an angle α.

5.3 Seismic Design Coefficients and Approximate Period Parameters (Appendix R)

This appendix contains design coefficients, system limitations and design parameters for seismic load resisting systems included in Seismic Provisions but not yet defined in the applicable building codes. Therefore, the values presented in this appendix shall only be used where neither the applicable building code nor ASCE 7 contain such values. These values are taken from the 2003 NEHRP [9,10].

Table 5.3-1. Design Coefficients and Factors for Basic Seismic-Load-Resisting Systems

Basic Seismic Load-Resisting System	**Response Modification Coefficient R**	**System Overstrength Factor Ω_o**	**Deflection Amplification Factor C_d**	**Height Limit (ft)**			
				Seismic Design Category			
				B & C	**D**	**E**	**F**
Building Frame Systems							
Buckling-Restrained Braced Frames, non-moment-resisting beam-column connections	7	2	5½	NL	160	160	100
Special Plate Shear Walls	7	2	6	NL	160	160	100
Buckling-Restrained Braced Frames, moment-resisting beam-column connections	8	2½	5	NL	160	160	100
Dual Systems with Special Moment Frames Capable of Resisting at Least 25% of the Prescribed Seismic Forces							
Buckling-Restrained Braced Frames	8	2½	5	NL	NL	NL	NL
Special Plate Shear Walls	8	2½	6½	NL	NL	NL	NL

Table 5.3-2. Values of Approximate Period Parameters C_t and x

Approximate Fundamental Period $T_a=C_t h_n^x$, where h_n is the height		
Structure Type	**C_t**	**x**
Buckling-Restrained Braced Frames	0.03	0.75
Special Plate Shear Walls	0.02	0.75

5.4 Qualifying Cyclic Tests of Buckling-Restrained Braces (Appendix T)

The Buckling-Restrained Braces is the heart of the newly introduced Buckling-Restrained Braced Frames. Therefore, this appendix is included to regulate the qualifying cyclic tests for individual buckling-restrained braces and buckling-restrained brace subassemblages. It addresses test specimens for subassemblage and brace, material testing requirements, instrumentation, loading history criteria, test reporting requirements and acceptance criteria.

5.5 Welding Provisions (Appendix W)

This is a non-mandatory Appendix that will later be replaced by AWS D1.8. It provides additional details regarding welding and welding inspections. It covers the minimum required information for Contract Documents, Shop and Erection Drawings. It also address the qualification of welding personnel, including QC Welding Inspector, QA Welding Inspectors, and Nondestructive Testing Technicians. General procedure guidelines and special welding provisions are also provided, such as nondestructive testing procedures, filler metals requirements, maximum interpass temperatures, and additional welding provisions for demand critical welds, etc.

6. GENERAL REVISIONS FOR ALL SEISMIC LOAD RESISTING SYSTEMS

For all seismic applications, there are basic parameters that applied to all structural systems. These serve as minimum requirements for any seismic performance. If improved performances are desired for specific structural systems, more stringent and/or additional requirements are then added. These basic requirements in Seismic Provisions include: materials; connections, joint, and fasteners; and members. Modifications to these requirements will be discussed in the following sections.

6.1 Materials

Additional materials are added in the new 2005 Seismic Provisions. There are A913/A913M Grade 60, A1011 SS Grade 55, or A1011 HSLAS Grade 55. Other steels and non-steel materials in buckling-restrained braced frames are permitted to be used when subject to the associated requirements of BRBF.

The new Seismic Provisions further clarifies how to determine the available strength of element (a member or a connection), and the values of R_y (material yield overstrength) and R_t (overstrength of material tensile strength) for different type of materials.

The available strength of the elements shall be ϕR_n for LRFD and R_n/Ω for ASD, where R_n is the nominal connection strength, which shall be equal to or greater than the required strength. The required strength shall be determined form expected yield stress, R_yF_y, of an adjoining member. The expected tensile stress, R_tF_u and the expected yield stress R_yF_y are permitted to be used in lieu of F_u and F_y, respectively, in determining the nominal strength, R_n, of fracture and yield limit states within the same member that expected strength is determined. In the absence of qualifying test results, R_y and R_t are tabulated in Table 6.1.

Table 6.1. R_y and R_t Values for Different Member Types

Application	R_y	R_t
Hot-rolled structural shapes and bars:		
ASTM A36/A36M	1.5	1.2
ASTM A572/572M Grade 42 (290)	1.3	1.1
ASTM A572/572M Grade 50 (345) or Grade 55 (380), A913/A913M, A588/A588M, A992/A992M, A1011SS Grade 55(380), A1011 HSLAS Grade 55 (380)	1.1	1.1
ASTM A529 Grade 50 (345)	1.2	1.2
ASTM A529 Grade 55 (380)	1.1	1.2
Hollow structural sections (HSS): ASTM A500 (Grade B or C), A501, A618, and A847	1.4	1.3
Steel pipe ASTM A53/A53M	1.6	1.2
Plates:		
ASTM A36/A36M	1.3	1.2
ASTM A572/A572M Gr. 50, A588/A588M	1.1	1.2

6.2 Connections, Joints, and Fasteners

It is emphasized in the "scope" that the connection for a member of SLRS shall be designed such that a ductile limit state controls. Previously similar statements only appear in the bolted joints sections, which might be misleading in such way that same requirements do not apply to welded joints. Majority of the requirements remain the same for both bolted and welded joints, except as follows.

6.2.1 Bolted Joints

In order to expand prohibition of sharing of forces between bolts and welds from same faying surfaces to all cases, the provision "Bolts and welds shall not be designed to share the force in a joint" is added. However, bolted webs combined with welded flanges in moment connections and column splices are still permitted based on deformation compatibility. The desirable ductile limit states are yielding or bearing deformation.

For brace diagonals, oversized holes shall be permitted when the connection is designed as a slip-critical joint, and the oversized hole is in one ply only.

6.2.2 Welded Joints

For welded joints, same welding requirements are demanded, except that Welding shall also be performed in accordance with Appendix W. The concept of "Demand Critical Welds" and "Protected Zone" are introduced to welded joints and discussed previously.

In order to avoid welding into the k-region of hot-rolled shapes, a section regarding Continuity Plates and Stiffeners is added to regulate the corner clip when used in the webs of rolled shape. See Figure 3 for dimension requirements.

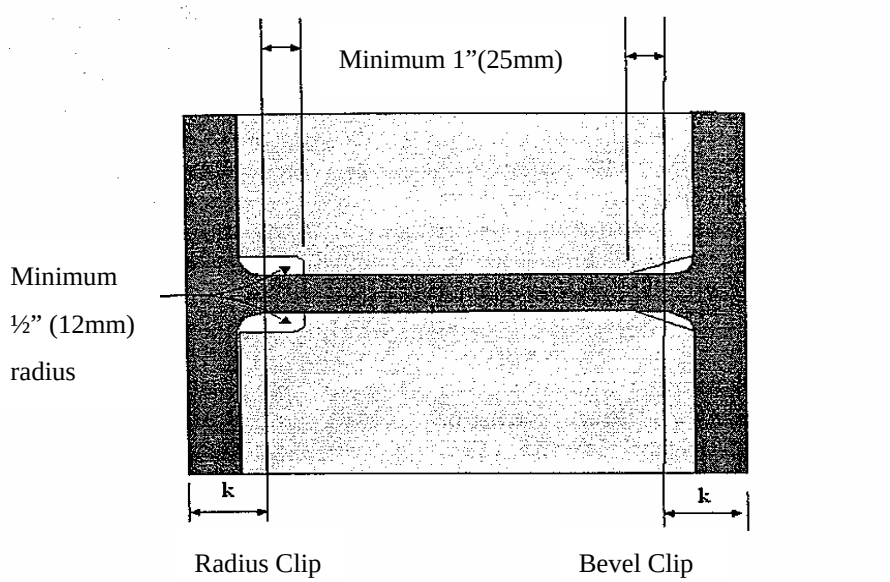

Figure 3. Clip Dimension Requirements

6.3 Members

In this section, width-thickness ratio for SLRS and requirement for columns are specified. The contents are essentially the same, except the language modifications and the following clarifications.

For width-thickness ratio, Table B4.1 of the main specification no longer includes values for combined flexure and axial compression, so it is inserted into footnote j of the new Seismic Provisions.

For Column Splices, to emphasize other special requirements applied, the new Seismic Provisions further list column splice sections number for SMF(8.3), IMF(9.9), OMF(11.9), SCBF(13.5), and BRBF(16.5b).

For Column Bases, unlike the existing specification which only contain general statement, the new specification specifically stated the column base are to be designed for: Required Axial Strength, Shear Strength ($2R_yF_yZ_x/H$ includes R_y factor), and Flexural Strength ($1.1R_yF_yZ$).

7. SPECIFIC REVISIONS FOR EXISTING SYSTEMS

Existing structural systems include Special Moment Frames (SMF), Intermediate Moment Frames (IMF), Ordinary Moment Frames (OMF), Special Truss Moment Frames (STMF), Special Concentrically Braced Frames (SCBF), Ordinary Concentrically Braced Frames (OCBF), and Eccentrically Brace Frames (EBF). Depending on the performance of the existing structural systems, modifications are made. Among these existing systems, OCBF section is one of the most improved provisions.

7.1 Special Moment Frames (SMF)

Special moment frames are one of the most ductile and promoted system. They are very well understood and regulated [11-13]. Therefore, not many changes are made, except for further clarifications.

The special requirements of "Demand Critical Welds" and "Protected Zones" are emphasized. For beam-to-column connection, beam flanges, and continuity plates, it is added that connections designed in accordance with ANSI/AISC 358 is satisfactory.

For column-beam moment ratio requirement exceptions, it is clarified that only "moment frame columns" should be accounted in the available shear strength calculations. The language "Restraint" in beam-to-column connection is changed to "Lateral Bracing". It is further clarify that lateral bracing is required only at the top beam flange level of column flanges in beam-to-column connections, when the webs of the beams and column are co-planar.

7.2 Intermediate Moment Frames (IMF)

In order to improve the behavior of Intermediate Moment Frames, additional requirements similar to SMF are added [11-13]. These include discontinuities requirements and lateral beam bracing requirements.

To avoid discontinuities, it is added that abrupt changes in beam flange area are not permitted in plastic hinge regions. Drilling of flange holes or trimming of beam flange width is permitted if testing or qualification demonstrates that the resulting configuration can develop stable plastic hinges that meet the requirements in Section 10.2b by tests.

For Lateral Bracing of Beams, same provision as SMF is added, except that the unbraced length between lateral braces shall not exceed $0.17r_yE_s/F_y$ ($0.086r_yE_s/F_y$ for SMF).

7.3 Ordinary Moment Frames (OMF)

The Ordinary Moment Frames (OMF) provisions were primarily developed for use with wide flange shapes, however, they may be applied to other shapes such as channels, built-up sections, and hollow structural sections (HSS shapes). Main changes for OMF are regarding connections. It is clarified that the connections in conformance with SMF, or IMF shall be permitted without meeting additional requirement for FR moment connections and Continuity Plates in OMF [11-13]. For FR connection, weld access holes are prohibited in the beam web adjacent to the end-plate in bolted moment end-plate connections. The new provisions further emphasize that Complete-joint-penetration groove welds of beam flanges to column flanges and welds of shear plates and beam webs to columns shall be demand critical welds. For one-sided connections, continuity plate thickness is relaxed to be at least one half of the thickness of beam flange. (Previously, the continuity plate thickness is always greater or equal of beam flange thickness.)

7.4 Special Truss Moment Frames (STMF)

Special Truss Moment Frames are expected to withstand significant inelastic deformation within the

special segments, while other segments remain elastic under design earthquake. Therefore, requirements for the special segment are further clarified and toughened to ensure the desirable behavior.

To avoid confusion, the "design strength" and "axial force" used in previous Seismic Provisions are replaced by "required strength" and "the required axial strength". It is further clarify the contribution of diagonal compressive members in shear strength should be 0.3 times the available compressive strength.
The special segment shall be a protected zone meeting the associated requirements. Diagonal web members within the special segment shall be made of flat bars of identical sections. The required strength of lateral bracing at the end and within the special segment is increased to 6% R_yP_{nc} (5% in previous version), and outside of the special segment is decrease to 2% R_yP_{nc} (2.5% in previous version).

7.5 Special Concentrically Braced Frames (SCBF)

Special Concentrically Braced Frames has more ductility over OCBF due to its brace performance. Therefore, the requirements are slightly modified for bracing member, bracing connections, bracing configurations and column splices. In addition, the protected zones for the system are specified.

For Bracing Members, slenderness KL/r limit is change to $\leqq 4(E/E_y)^{0.5}$ from $5.87(E/E_y)^{0.5}$; except that $4(E/E_y)^{0.5} <KL/r<200$ are permitted, when the available column strength is at least equal to R_y times nominal strength of connecting brace elements. For required brace strength, the compressive strength requirement is removed; and the tensile strength requirements (when effective net area is less than gross area) are added to be the lesser of the expected tension yield strength $R_yF_yA_g$ and maximum load effect that can be transferred to the brace by the system.

For bracing connections, the required compressive strength based on buckling limit state is increase to $1.1R_yP_n$, while previously only R_yP_n is required.

For bracing configuration, it is further clarified that "As a minimum, one set of lateral braces is required at the point of intersection of the V-type (or inverted V-type) bracing, unless the beam has sufficient out-of –plane strength and stiffness to ensure stability between adjacent brace points."

The protected zone of bracing members in SCBF shall include the center 1/4 and a zone adjacent to each connection equal to the brace depth in the plane of buckling.
The protected zone of SCBF shall include elements that connect braces to beams and columns.

7.6 Ordinary Concentrically Braced Frames (OCBF)

To be consistent with other systems, the required member strength from previous code that required the amplified seismic load was dropped and replaced with reduction in R factor without seismic load amplification. The Slenderness KL/r for bracing members in K, V, or inverted-V configurations is further limited to 4 from $4.23(E/F_y)^{0.5}$ in order to prevent undesirable post-buckling behavior resulting from the high difference between compression and tension strength.

Additional requirements are included to eliminate the liberal usage of OCBF. They include Special

Bracing Configuration Requirements same as SCBF, except that K-type bracing is allowed when meeting the same requirements for V-type and Inverted-V-type Bracing. For bracing connections, "bolt slip" are allowed when designing for a lower force level than is required for other limit states. Bolt slip is not an ultimate limit state and its associated energy dissipation can serve to reduce seismic response [14].

7.7 Eccentrically Braced Frames (EBF)

The specifications for Eccentrically Braced Frames are essentially the same as previous, except minor additional clarifications as follows:

(1) Bracing Connections (15.6c): Additional requirements are added such that the diagonal brace connections shall also satisfy the similar required axial tensile and compressive strength of SCBS, including the expected yield strength in tension $R_yF_yA_g$, and $1.1R_y$ times the nominal compressive strength P_n.
(2) Beam-to-Column Connections (15.7): If moment connections are required away from the link, the requirement for beam-to-column connections for OMF shall be met.
(3) The Protected Zone (15.9): Links are identified as Protected Zones and shall satisfy the associated requirements.
(4) Demand Critical Welds: (15.10) Locations of Demand Critical Welds are identified as welds attaching the link flanges and the link web to the column, and shall satisfy the associated requirements.

8. CONCLUSIONS

In the new 2005 AISC Seismic Provisions, the scope is expanded to cover the "design, fabrication, and erection" of structural members and connections in the seismic load resisting systems (SLRS). The Seismic Provisions become more concise by incorporating the ASD alternatives into LRFD sections. The existing Seismic Provisions are improved and clarified. New terms, such as "Protected Zones" and "Demand Critical Welds", are introduced to clarify the concept of seismic design – that is to ensure ductile limit state at critical elements. Two new structural systems (1) Buckling Restrained Braced Frames and (2) Special Plate Shear Walls are introduced and codified. Accordingly, improved seismic designs should be expected in routine office practice. Hopefully, the expected performance level of steel building under seismic events could be ensured.

REFERENCES

[1] AISC, “Seismic Provisions for Structural Steel Buildings”, American Institute of Steel Construction, Chicago, IL, 2005.

[2] AISC, “Specification for Structural Steel Buildings”, ANSI/AISC 360, Chicago, 2005.

[3] AISC, “Prequalified Connections for Special and Intermediate Steel Moment Frames for Seismic Applications”, AISC 353, Chicago, IL, 2005.

[4] AISC, “Seismic Provisions for Structural Steel Buildings”, American Institute of Steel Construction, Chicago, IL, 2002.

[5] AISC, “Load and Resistance Factor Design Specification”, American Institute of Steel Construction, 3rd Ed., Chicago, IL, 2001.

[6] AISC, “Specification for Structural Steel Buildings, Allowable Stress Design and Plastic Design”, American Institute of Steel Construction, Chicago, IL, 1989.

[7] ASCE, “Minimum Design Loads for Buildings and Other Structures”, ANSI/ASCE 7-2002, American Society of Civil Engineers, Reston, VA, 2002.

[8] ASCE, “Minimum Design Loads for Buildings and Other Structures”, ANSI/ASCE 7-1998, American Society of Civil Engineers, Reston, VA, 1998.

[9] AWS, “Structural Welding Code Steel”, ANSI/AWS D1.1:2002, American Welding Society, Miami, FL, 2000.

[10] FEMA, “NEHRP (National Earthquake Hazards Reduction Program) Recommended Provisions for Seismic Regulations for New Buildings”, Federal Emergency Management Agency, Washington, DC, 2003.

[11] FEMA, “Recommended Seismic Design Criteria for New Steel Moment-Frame Buildings”, FEMA350, Federal Emergency Management Agency, Washington, DC, 2000.

[12] FEMA, “Recommended Specifications and Quality Assurance Guidelines for Steel Moment-Frame Construction for Seismic Applications”, FEMA353, Federal Emergency Management Agency, Washington, DC, 2000.

[13] FEMA, “NEHRP (National Earthquake Hazards Reduction Program) Recommended Provisions for Seismic Regulations for New Buildings”, Federal Emergency Management Agency, Washington, DC, 2000.

[14] Sabelli, R., “EERI/FEMA NEHRP Professional fellowship report: Research on improving the seismic behavior of earthquake-resistant steel braced frames”, Earthquake Engineering Research Institute, Oakland, CA, 2001.

BOND CHARACTERISTICS BETWEEN CFRP AND STEEL PLATES IN DOUBLE STRAP JOINTS

S. Fawzia[1], X.L. Zhao[1,*], R. Al-Mahaidi[1] and S. Rizkalla[2]

[1]*Department of Civil Engineering, Monash University, Clayton, Victoria 3800, Australia*

[2]*North Carolina State University, Raleigh, North Carolina, USA*

*(*Corresponding Author, Email: ZXL@eng.monash.edu.au)*

Abstract: This paper describes a series of double strap shear tests loaded in tension to investigate the bond between CFRP sheets and steel plates. Both normal modulus (240 GPa) and high modulus (640 GPa) CFRPs were used in the test program. Strain gauges were mounted to capture the strain distribution along the CFRP length. Different failure modes were observed for joints with normal modulus CFRP and those with high modulus CFRP. The strain distribution along the CFRP length was found to be similar for the two cases. A shorter effective bond length was obtained for joints with high modulus CFRP whereas larger ultimate load carrying capacity can be achieved for joints with normal modulus CFRP when the bond length is long enough. The Hart-Smith Model was modified to predict the effective bond length and ultimate load carrying capacity of joints between the normal modulus CFRP and steel plates. The Multilayer Distribution Model developed by the authors was modified to predict the load carrying capacity of joints between the high modulus CFRP and steel plates. The predicted values agreed well with experimental ones.

Keywords: CFRP (Carbon Fibre Reinforced Polymer), Bond Failure, Double Strap Joints, Effective Bond Length, Steel Plate.

1. INTRODUCTION

Carbon fibre reinforced polymers (CFRP) are relatively new materials used in retrofitting, that is, to prolong the life of structural members and increase their load carrying capacity (Intelligent Sensing for Innovative Structures Canada (ISIS) [1], Moy [2], American Concrete Institute (ACI) Committee 440 [3], Teng *et al.* [4], Ohelers and Seracino [5]). The evolution of CFRP technologies and their versatility for applications in civil constructions require comprehensive and reliable codes of practice. Guidelines are available on the rehabilitation and retrofit of concrete structures with advanced composite materials. However, the practice for concrete can not be directly used for steel structures due to the fact that concrete and steel are very different materials [6]. There is a need to develop appropriate design guidelines for CFRP strengthened steel structures. It is important to understand the bond characteristics between CFRP and steel plates.

This paper describes a series of double strap shear tests loaded in tension to investigate the bond between CFRP sheets and steel plates. Both normal modulus (240 GPa) and high modulus (640 GPa) CFRPs were used in the test program. Strain gauges were mounted to capture the strain distribution along the CFRP length. Discussions are made on failure modes, strain distribution along the CFRP, ultimate load carrying capacity and effective bond length. Two theoretical models are proposed in this study for joints with normal and high modulus CFRPs, respectively. The Hart-Smith [7,8] model was originally developed for double strap adhesive joints. This model was modified to predict the ultimate load carrying capacity and effective bond length of steel plates bonded with multi-layer normal modulus CFRP. This proposed model is called "Modified Hart-Smith Model" in this paper. A Multilayer Distribution Model was developed by Fawzia *et al.* [9] for high modulus CFRP bonded to steel tubes. This model was modified to predict the load carrying capacity of joints between the high modulus CFRP with steel plates. The new model was called

"Modified Multilayer Distribution Model" in this paper. The predicted values agreed well with experimental ones.

2. MATERIALS

In the present research, MBrace fibre CF530 and CF130 were chosen. MBrace CF530 is called high modulus CFRP in this paper. It has a nominal modulus of elasticity of 640 GPa. CF130 is called normal modulus CFRP in this paper with a nominal modulus of elasticity of 240 GPa. The nominal ultimate tensile strength of CFRP is 2650 MPa for CF530 and 3800 MPa for CF130. Araldite 420 adhesive was chosen. Steel plates with a thickness of 5 mm are used in the test program. The yield stress of the steel plate is around 360 MPa.

3. SPECIMENS AND TEST SET UP

A total of eight specimens were prepared. All steel plates have a dimension of 210 mm in length and 50 mm in width. The steel plates were ground with linisha in the area to be bonded to ensure a better mechanical interlocking. The surfaces were cleaned with acetone to remove grease, oil and rust. Two steel plates were alinged in position in a jig before applying adhesives and CFRP. Three layers of CFRP sheets were applied on both sides of the plate. The specimens were cured for 7 days and postcured for one day at 70^{o}C. A schematic view of a specimen is shown in Figure 1 where the length L_1 is always less than L_2 to aim that the failure occurs on one end only. Several foil strain gauges were attached to the CFRP bonded length. One was located at the joint and others were located every 15 mm along the the bonded length. Each specimen was loaded in tension in a 500 kN capacity Baldwin universal testing machine with a loading rate of 2 mm/min in a similar way as reported in Fawzia *et al.* [9], Jiao and Zhao [10]. Figure 2 shows a typical test set up.

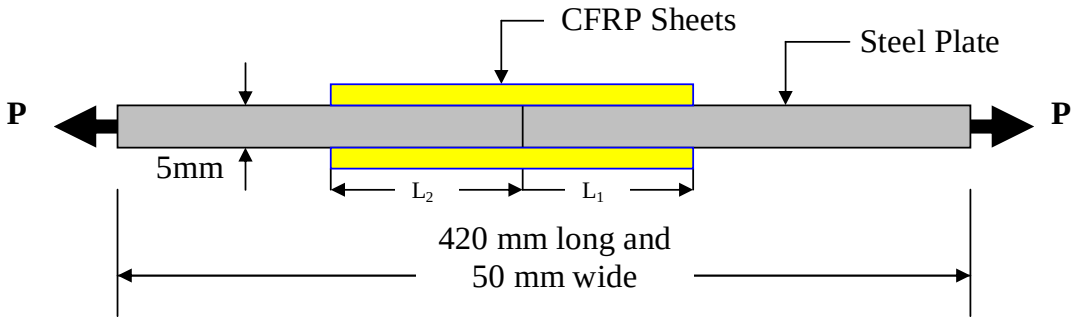

Figure 1. A schematic view of specimen (not to scale)

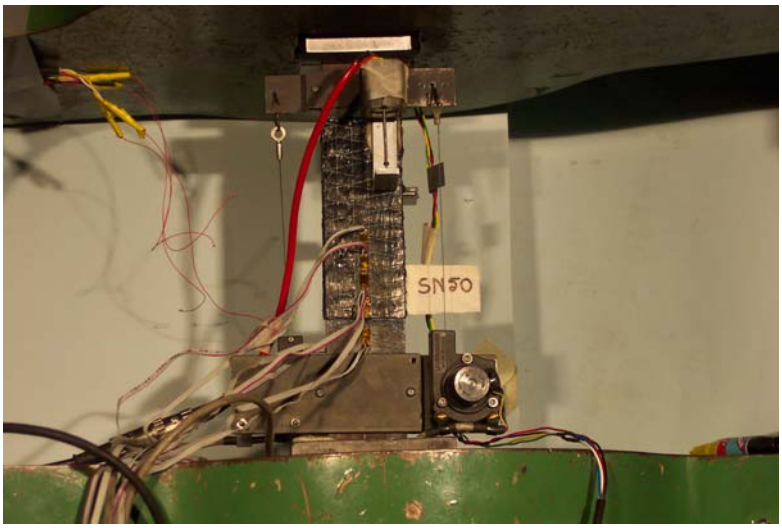

Figure 2. A typical test set up

4. TEST RESULTS

4.1 Failure Modes

The failure mode for joints with normal modulus CFRP was found to be bond failure whereas fibre break failure was observed for joints with high modulus CFRP. This is similar to those observed previously from similar tests on CFRP and steel tubes [9,10]. Typical failure modes are presented in Figure 3.

(a) Steel plates with normal modulus CFRP (this paper)

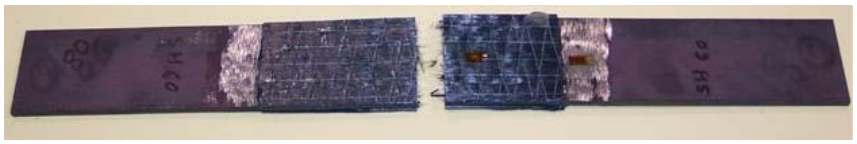

(b) Steel plates with high modulus CFRP (this paper)

(c) Steel tubes with normal modulus CFRP (Jiao and Zhao (2004))

(d) Steel tubes with high modulus CFRP (Fawzia et al (2004b))

Figure 3. Typical failure modes

4.2 Strain Distribution along the Bonded Length

The distribution of strain along the bonded length can be found from the gauge readings at the top layer. These readings are plotted in Figure 4 under different load level. The load level is defined as a ratio of applied load to the maximum load (P_{ult}) achieved in the test. Only the average readings from all specimens are shown in Figure 4. It is clear from the figure that strain generally decreases with the distance away from the joint between the two plates. The distribution for normal modulus CFRP joints seems to be nonlinear whereas that for high modulus CFRP joints seems to be linear. As expected, smaller strain values were obtained for joints with high modulus CFRP.

4.3 Ultimate Load

The ultimate load carrying capacity (P_{ult}) obtained in the tests are summaried in Table 1. The first letter (S) in a specimen label means specimen. The second letter (N) indicates normal modulus CFRP or (H) means high modulus CFRP. The numbers (20, 40, 50, 60, 70 or 80) indicates the bonding length (L_1) defined in Figure 1.

Table 1. Test results

Specimen Label	Bond Length L_1 (mm)	Ultimate Load P_{ult} (kN)	Failure Mode
SN20	20	33.7	Bond Failure
SN40	40	49.9	Bond Failure
SN50	50	69.8	Bond Failure
SN70	70	80.8	Bond Failure
SN80	80	81.3	Bond Failure
SH20	20	42.8	Fibre Break
SH40	40	53.1	Fibre Break
SH60	60	52.2	Fibre Break

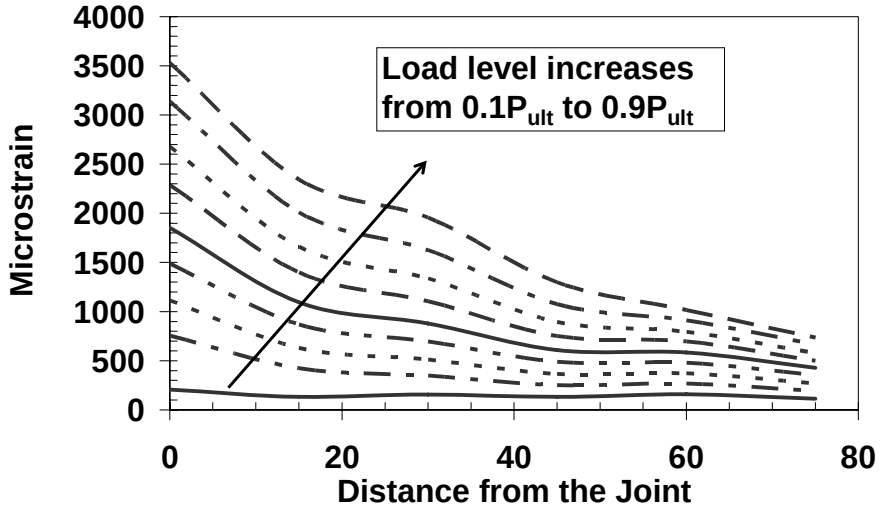

(a) normal modulus CFRP

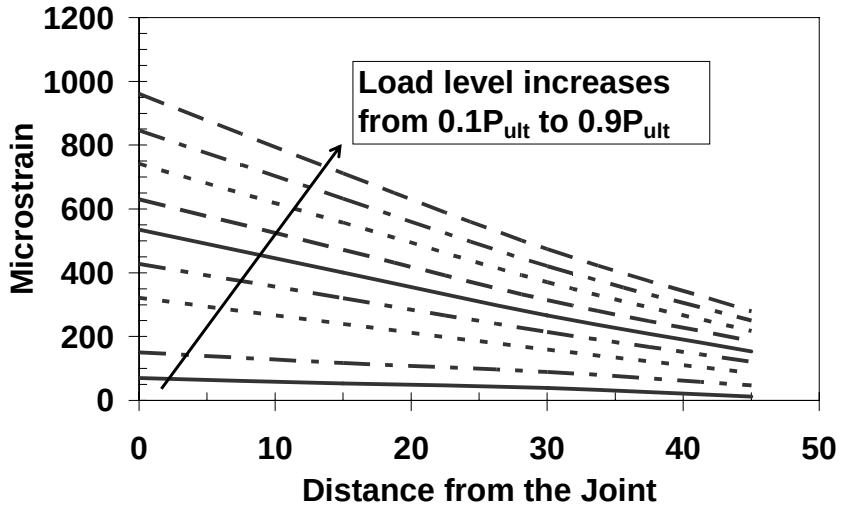

(b) high modulus CFRP

Figure 4. Distribution of strain along the bonded length

4.4 Effective Bond Length

The ultimate load carrying capacity is plotted in Figure 5 against the bond length (L_1). It can be seen from Figure 5 that the load carrying capacity reaches a plateau after the bond length exceeds a certain value. This length, beyond which no significant increase in load carrying capcaity will occur, is called the effective bond length. A similar concept was used by Teng *et al.* [4] and Jiao and Zhao [10]. It seems that the effective bond length for joints with high modulus CFRP (about 40 mm) is

smaller than that for joints with normal modulus CFRP (about 75 mm). This matches the failure mode shown in Figure 3, i.e. a longer bond length is required for normal modulus to build up the full strength of the joint through bond capacity. This may be due to the fact that the use of high modulus CFRP results in lower shear strain deformations in the epoxy layer. The effective bond length of 75 mm for joints with normal modulus CFRP is almost the same as that reported in Jiao and Zhao [10] for joints between steel tubes and normal modulus CFRP. It seems that the curved surface of steel tubes does not affect the effective bond length between steel and normal modulus CFRP.

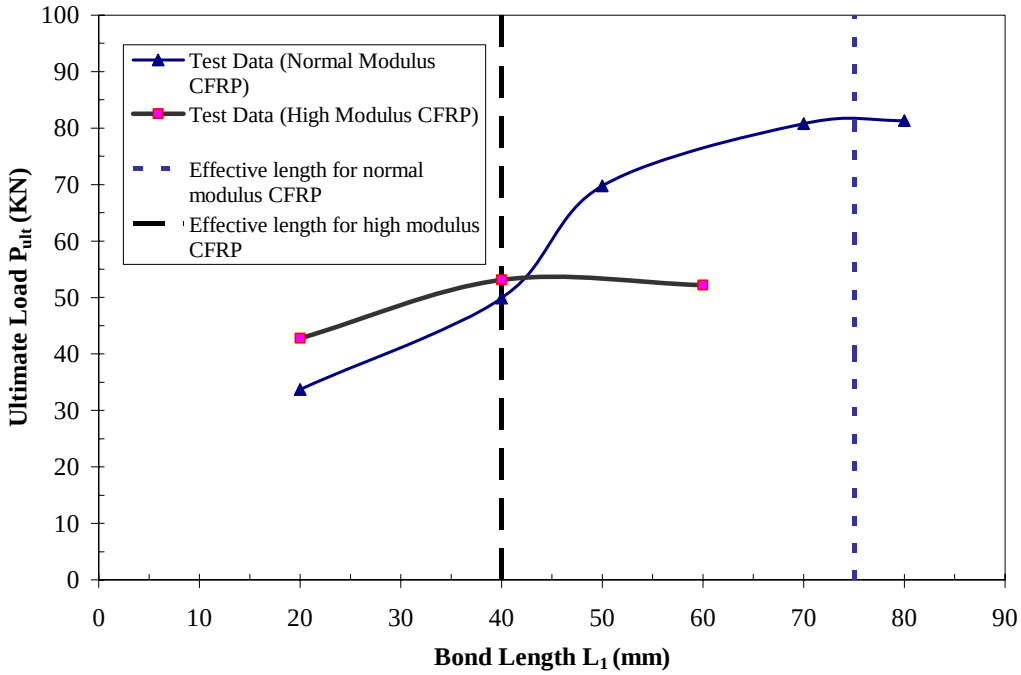

Figure 5. Effective bond length for joints with normal and high modulus CFRP

Another interesting phenomenon shown in Figure 5 is that the load carrying capacity of joints with normal modulus CFRP is lower than that of joints with high modulus CFRP when the bond length is short, around 40 mm in this case. This is most likely because the normal modulus CFRP has not become fully effective yet. When the bond length increases further the load carrying capacity of joints with normal modulus CFRP becomes larger. This is due to the fact that the normal modulus CFRP has a higher tensile strength than the high modulus CFRP. Designers may utilize this phenomenon to select different CFRP and bond length to acheive certain load carrying capacity.

5. MODEL FOR JOINTS BETWEEN STEEL PLATES AND NORMAL MODULUS CFRP

5.1 Hart-Smith Model for Double Strap Joints

Various theoretical analyses of adhesively bonded joints were carried out by many researchers. Double-Strap joint was treated as a symmetrical configuration consisting of two Double-Lap joints [8]. Detailed explanation on the stress and strain distribution can be found in Hart-Smith [8]. The non-uniform distribution of the strains and stresses in the Double-Strap joints is illustrated in Figure 6 [11]. For the short overlap joints, the minimum adhesive stress and strain are as high as maximum values. While for the long overlap joints, the load transfer is confined to two end zones

with a lightly-loaded elastic trough in between. This section summarizes the formulae for the effective bond length and the ultimate load carrying capacity per unit width for Double-Strap Joints. Detailed derivations can be found in Hart-Smith [7,8]. The effective bond length (L_e) is expressed as:

$$L_e = \frac{\sigma_{ult} \cdot t_i}{\tau_p} + \frac{2}{\lambda} \qquad \text{where} \quad \lambda = \sqrt{\frac{G_a}{t_a}\left(\frac{1}{E_o t_o} + \frac{2}{E_i t_i}\right)} \tag{1}$$

in which, σ_{ult} is the ultimate tensile strength of the inside adherent, τ_p is the adhesive shear strength in the idealized elastic-plastic stress-strain curve, G_a is the adhesive shear modulus, t_a is the adhesive thickness, E is the Young's modulus of adherent and t is thickness of the adherent while the subscripts o and i represent outside and inside adherents, respectively.

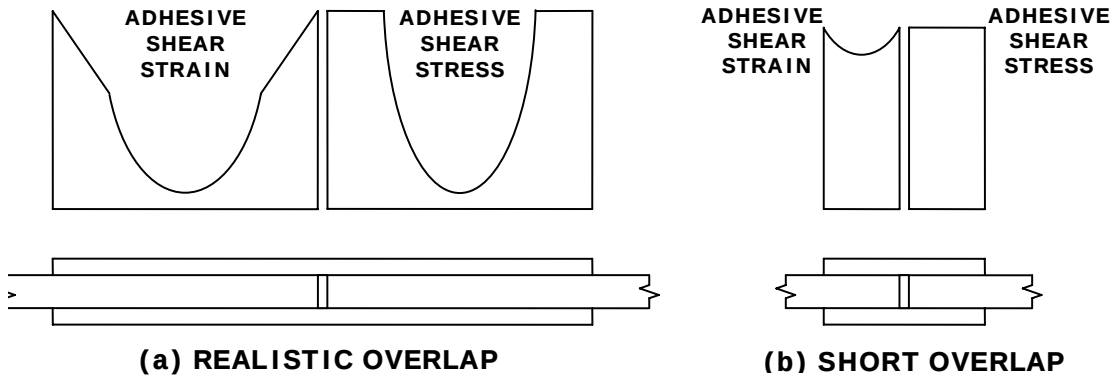

Figure 6. Non-uniform strains and stresses in double strap joints (Hart-Smith 2001)

The ultimate load carrying capacity per unit width is taken as the lesser of P_i and P_o:

$$P_i = \sqrt{\left[2 \cdot \tau_p \cdot t_a \cdot (\frac{1}{2} \cdot \gamma_e + \gamma_p) \cdot 2 \cdot E_i \cdot t_i \cdot \left(1 + \frac{E_i \cdot t_i}{2 \cdot E_o \cdot t_o}\right)\right]} \tag{2a}$$

$$P_o = \sqrt{\left[2 \cdot \tau_p \cdot t_a \cdot \left(\frac{1}{2} \cdot \gamma_e + \gamma_p\right) \cdot 4 \cdot E_o \cdot t_o \cdot \left(1 + \frac{2 \cdot E_o \cdot t_o}{E_i \cdot t_i}\right)\right]} \tag{2b}$$

where γ_e and γ_p represent elastic and plastic adhesive shear strains, respectively.

5.2 Modified Hart-Smith Model (MHSM)

The Hart-Smith model presented above was derived for double-strap joints with one layer of outside adherent. For the joint between steel plates and CFRP defined in Figure 1, more than one layer of CFRP was applied with adhesives between each layer. Some modification is necessary before using the Hart-Smith model.

Obviously the steel plate is the inside adherent. It is assumed in this paper that the adhesive to be used for the model is the adhesive between the steel plate and the first layer of CFRP. The rest of the material above this layer of adhesive is considered as the outside adherent. The modulus of elasticity E_o is approximately taken as that of CFRP (E_{CFRP}). Therefore the thicknesses t_i, t_o, t_a and modulus E_o can be determined as follows based on equal thickness epoxy between the CFRP and steel and between each of the CFRP layers:

$$t_i = t_{steel} \tag{3a}$$

$$t_a = \frac{\frac{1}{2}\cdot(T - t_{steel})}{n} - t_{CFRP} \tag{3b}$$

$$t_o = n \cdot t_{CFRP} + (n-1)\cdot t_a \tag{3c}$$

$$E_o = E_{CFRP} \tag{3d}$$

in which, t_{steel} is the thickness of the steel plate, t_{CFRP} is the thickness of the CFRP sheet, T is the average total thickness of the specimen at the joint and n is the number of CFRP layers on one side of the joint.

The modulus of elasticity E_i is that of steel. The adhesive shear modulus G_a is taken as 1000 MPa as adopted by Matta [12]. The adhesive shear strength τ_p is that for Araldite 420 given by the manufacturer.

The parameters used in calculating the effective bond length are summarized in Table 2. The value of $L_{e,MHSM}$ (stands for effective bond length based on modified Hart-Smith model) so calculated is 73 mm.

Table 2. Parameters used in the calculations for the modified Hart-Smith model

T (mm)	t_{steel} (mm)	t_{CFRP} (mm)	t_i (mm)	t_a (mm)	t_o (mm)	σ_{ult} (MPa)	τ_p (MPa)	G_a (MPa)	E_o (GPa)	E_i (GPa)	n
7.5	5.1	0.176	5.1	0.224	0.976	430	36	1000	240	200	3

The ultimate load carrying capacity predicted by the modified Hart-Smith model ($P_{ult,MHSM}$) for the joint shown in Figure 1 (a) becomes:

$$P_{ult,MHSM} = b \cdot \min\{P_i, P_o\} \tag{4}$$

where b is the width of the joint which is 50 mm in this case, P_i and P_o are defined in Eq (2).

The elastic adhesive shear strain γ_e is equal to τ_p/G_a. The value of the plastic adhesive shear strain γ_p is taken as 3 times γ_e in this paper to allow certain amount of shear deformation for the joint shown in Figure 1. The ultimate load obtained using Eq (4) is about 83 kN.

The load carrying capacity for any bond length (L_1) can be expressed as follows if one assumes that the load is linearly proportional to the bond length:

$$P_{CFRP,MHSM} = L_1 \cdot \frac{P_{ult,MHSM}}{L_{e,MHSM}} \qquad \text{if } L_1 \le L_e \tag{5a}$$

$$P_{CFRP,MHSM} = P_{ult,MHSM} \qquad \text{if } L_1 > L_e \tag{5b}$$

where $P_{ult,MHSM}$ is given by Eq (4) and $L_{e,MHSM}$ is given by Eq (1) with modifications defined in Eq (3). The modified Hart-Smith model is compared with the test results in Figure 7 where good

agreement is evident. More details about the modified Hart-Smith model and other empirical models can be found in Liu *et al.* [13].

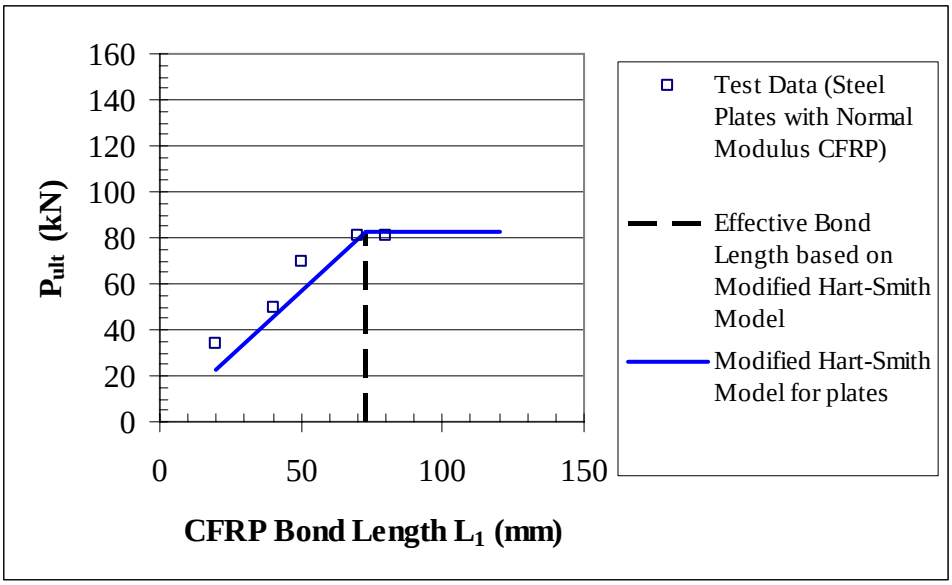

Figure 7. Results of modified Hart-Smith model for steel plates and normal modulus CFRP

6. MODELS FOR JOINTS USING HIGH MODULUS CFRP

6.1 Multilayer Distribution Model (MDM) for Steel Tubes by Fawzia et al (2004b)

A theoretical model was developed by the authors [9] to estimate the maximum load for multilayer high modulus CFRP bonded to circular hollow sections. The model was based on the measured strain distribution across the CFRP layers. The formula can be summarized as:

$$P_{p,MDM} = \sum_{i=1}^{n} A_i \cdot E_{CFRP} \cdot \frac{\varepsilon_{u,CFRP}}{\sqrt{i}} \qquad (6)$$

where i is the layer number, A_i is the area of CFRP at layer i, E_{CFRP} is the modulus of CFRP, $\varepsilon_{u,CFRP}$ is the measured ultimate tensile strain of CFRP and n is the number of CFRP layers. The predicted ultimate load was found [9] to be very close (within 0.5% on average) to that experimentally obtained.

6.2 Modified Multilayer Distribution Model (MMDM) for Steel Plates and High Modulus CFRP

The model developed for steel tubes and CFRP can be modified for the case with steel plates and CFRP. The total area of CFRP at layer i on both sides of the plate can be expressed as $A_i = 2 \times t_{CFRP} \times b$. Therefore the ultimate load using the modified multilayer distribution model (MMDM) can be written as:

$$P_{ult,MMDM} = 2 \cdot \sum_{i=1}^{n} t_{CFRP} \cdot b \cdot E_{CFRP} \cdot \frac{\varepsilon_{u,CFRP}}{\sqrt{i}} \qquad (7)$$

where t_{CFRP} = 0.19 mm, b = 50 mm, $\varepsilon_{u,CFRP}$ = 2113 x 10^{-6} (measured value from Ref. [9]) and E_{CFRP} = 508,386 MPa (measured value from Ref. [9]) and n = 3.

The predicted ultimate load is compared in Figure 8 with the experimental data. It can be seen that the predicted value is about 10% lower than the experimental ones when the bond length exceeds the effective bond length.

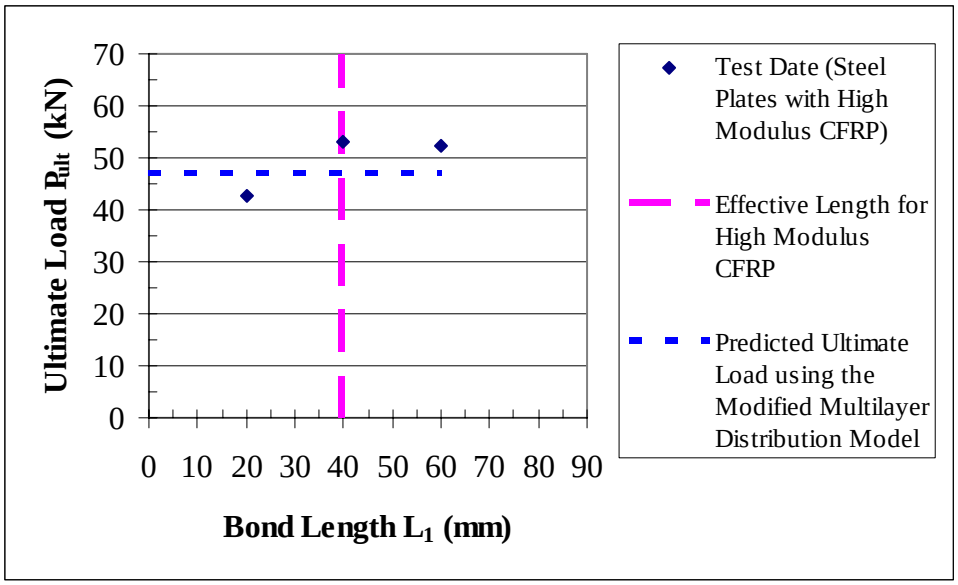

Figure 8. Results of modified multilayer distribution model for steel plates and high modulus CFRP

7. CONCLUSIONS

A series of tests on double strap joints were carried out to investigate the bond between CFRP sheets and steel plates. Both normal modulus (240 GPa) and high modulus (640 GPa) CFRPs were used in the test program. The following conclusions and observations are made based on the limited test results.

1. Different failure modes were observed for joints with normal modulus CFRP (bond failure) and those with high modulus CFRP (fibre break).
2. The strain distribution along the CFRP length was found to be similar irrespective of the CFRP modulus although much smaller strains were generated in joints with high modulus CFRP.
3. The load carrying capacity of joints with normal modulus CFRP is lower than that of joints with high modulus CFRP when the bond length is short. Larger ultimate load carrying capacity can be achieved for joints with normal modulus CFRP when the bond length is long enough.
4. A shorter effective bond length was obtained for joints with high modulus CFRP.
5. The load carrying capacity estimated by the Modified Hart-Smith Model for steel plate bonded with normal modulus CFRP was found to be in close agreement with that obtained experimentally.
6. The load carrying capacity predicted by the Modified Multilayer Distribution Model for steel plates bonded with high modulus CFRP agreed reasonably with the experimental results.

ACKNOWLEDGEMENTS

This project was sponsored by an Australian Reseach Council Discovery Grant. The authors wish to thank Mr. Graeme Rundle and Mr. Kevin Nievaart for their assistance in carrying out the tests. Degussa Construction Chemicals Australia Pty Ltd provided partial support in supplying the CFRP. The advice provided by Mr Andrew Sarkady of Degussa Construction Chemicals is gratefully acknowledged. Thanks are given to Dr. L.J. Hart-Smith for providing necessary information about his model. Thanks are also given to Ms. HongBo Liu for her assistance in deriving the modified Hart-Smith model.

NOTATION

A_i = Area of CFRP at layer i
E = Modulus of elasticity
E_{CFRP} = Modulus of CFRP sheet
E_i = Modulus of inside adherent
E_o = Modulus of outside adherent
G_a = Adhesive shear modulus
L_1 = Short bond length
L_2 = Long bond length
L_e = Effective bond length
P = Tensile load
P_i = Ultimate load of inside adherent
P_o = Ultimate load of outside adherent
P_p = Predicted load
P_{ult} = Ultimate load
T = Total thickness of specimen
b = Width of steel plate
i = 1, 2 and 3
n = Number of CFRP layers
t_a = Thickness of adhesive
t_{CFRP} = Thickness of CFRP sheet
t_i = Inside adherent thickness
t_o = Outside adherent thickness
t_{steel} = Thickness of steel plate
τ_p = Adhesive shear strength
λ = Effective parameter to calculate effective bond length
γ_e = Elastic adhesive shear strain
γ_p = Plastic adhesive shear strain
$\varepsilon_{u,CFRP}$ = Ultimate strain of CFRP
σ_{ult} = Ultimate tensile strength

REFERENCES

[1] ISIS, “Reinforcing Concrete Structures with Fiber Reinforced Polymers (FRPs)”, Design Manual 3, ISIS Canada Design Manuals, ISIS, Manitoba, Canada, 2001.

[2] Moy, S.S.J., “FRP Composites-Life Extension and Strengthening of Metallic Structures”, The Institute of Civil Engineers Design and Practice Guides, Institution of Civil Engineers (ICE). Thomas Telford Publishing, London, UK, 2001.

[3] ACI Committee 440, “Guide for the Design and Construction of Externally Bonded FRP Systems for Strengthening Concrete Structures”, Technical Committee Documents ACI 440.2R-02, ACI, USA, 2002.

[4] Teng, J.G., Chen, J.F., Smith, S.T. and Lam, L., “FRP Strengthened RC Structures”. John Wiley & Sons Ltd, West Sussex, UK, 2002.

[5] Oehler, D.J. and Seracino, R., “Design of FRP and Steel Plated RC Structures: Retrofitting beams and slabs for strength, stiffness and ductility”, Elsevier, Oxford, UK, 2004.

[6] Fawzia, S., Al-Mahaidi, R., Zhao, X.L. and Rizkalla, S., “Comparative Study of Failure Mechanisms in Steel and Concrete Members Strengthened with CFRP Composites, in Developments in Mechanics of Structures and Materials”, Deeks, A.J. and Hao, H. (eds), Balkema Publishers, London, 2004, pp.71-76.

[7] Hart-Smith, L.J., “Design and Analysis of Adhesive-Bonded Joints”, Air Force Conference on Fibrous Composites in Flight Vehicle Design, September, Douglas Paper 6059, Dayton, Ohio, USA, 1972.

[8] Hart-Smith, L.J., “Adhesive-Bonded Double-Lap Joints”, Technical Report NASA CR-112235, Douglas Aircraft Company, Long Beach, California, USA, 1973.

[9] Fawzia, S., Zhao, X.L., Al-Mahaidi, R. and Rizkalla, S., “Investigation Into the Bond between CFRP and Steel Tubes”, The Second International Conference on FRP Composites in Civil Engineering, December, Adelaide, 2004, pp.733-739.

[10] Jiao, H. and Zhao, X.L., CFRP Strengthened Butt-Welded Very High Strength (VHS) Circular Steel Tubes, Thin-Walled Structures, 2004, 42(7), pp.963-978.

[11] Hart-Smith, L.J., “Bolted and Bonded Joints”, Composites, Vol. 21, ASM Handbook, American Society for Materials (ASM) International, USA, 2001.

[12] Matta, F., “Bond Between Steel and CFRP Laminates for Rehabilitation of Metallic Bridges”, PhD Thesis, Faculty of Engineering, University of Padua, Italy, 2003.

[13] Liu, H.B., Zhao, X.L., Al-Mahaidi, R. and Rizkalla, S., “Analytical Bond Models Between Steel and Normal Modulus CFRP”, 4th International Conference on Advances in Steel Structures, Shanghai, June 2005.

STRUCTURAL BEHAVIOUR OF OVAL HOLLOW SECTIONS

L. Gardner

Department of Civil and Environmental Engineering, Imperial College London

Email: leroy.gardner@imperial.ac.uk

Abstract: Structural oval hollow sections represent a recent and rare addition to the range of cross-sections available to structural engineers and architects. Their emergence is also timely given the increasing application of hollow sections in construction and the current trend towards the use of bare steelwork to express structural form. However, despite widespread interest in their application on the basis of both architectural appeal and structural efficiency, a lack of verified design guidance is inhibiting uptake. This paper summarises previous analytical and experimental studies on oval hollow sections, and describes laboratory testing, numerical modelling and evaluation of preliminary design rules for the recently introduced structural elliptical hollow sections. Laboratory testing has been carried out in two primary structural configurations – compression and in-plane bending. In addition to the basic geometry (including initial geometric imperfections) and material properties, full load-deformation histories were recorded. Numerical models, using the finite element package ABAQUS, were created and validated against the test results, before a series of sensitivity and parametric studies were conducted. The models included features such as curved geometry, non-linear material properties and initial geometric imperfections. For stub column behaviour, ultimate load was generally well predicted by the numerical models, but prediction of deformation at ultimate load was less accurate. For bending behaviour, the full bending moment-deformation history was consistently well predicted. Comparison of the test and finite element results against preliminary design rules has demonstrated broadly acceptable agreement, but additional analysis on the basis of further testing and modelling is required.

Keywords: ABAQUS, elliptical, hollow sections, laboratory testing, numerical modelling, oval, steel structures.

1. INTRODUCTION

As the construction industry continues to evolve, innovative products and design techniques are being developed to respond to the ever increasing demands on both the efficiency and aesthetics of civil engineering structures. A recent advance has been the introduction of high strength, hot-rolled and cold-formed oval hollow sections for structural application. The fundamental test data and verified structural design guidance to enable their safe and efficient use is currently being developed. Previously, in projects where oval sections have been specified, structural engineers have been forced to adopt a pragmatic and conservative approach to the design [1]. A number of examples of applications of oval hollow sections in structural engineering projects have been reported [2].

Whilst maintaining, if not exceeding the aesthetic appeal of circular sections, oval sections also offer the structural advantages of sections with differing major and minor axis properties, i.e. more efficient use of material in a number of primary structural configurations, for example, flexural elements (in major axis bending) and compression elements (braced against minor axis buckling).

An oval has no single mathematical definition, but may be described generally as a curve with a smooth, convex, closed ‘egg-like’ shape; many types of oval, with a range of geometric properties (degree of elongation, asymmetry etc) therefore exist. A number of particular types have been examined in previous studies of elastic critical buckling and post-buckling of shells, the two most significant of which are defined by Eqs. (1) and (2). Other geometries have been described by Marguerre [3].

The curve defined by Eq. (1) is convenient because it can be used to generate a family of ovals of varying aspect ratio, but constant circumferential length, thereby providing a rational basis for comparisons.

$$r = \frac{r_0}{1 + \xi \cos\left(\frac{4\pi s}{L_0}\right)} \quad (1)$$

where r is the local radius of curvature, r_0 is the radius of a circle of circumference equal to that of the oval, ξ is a measure of eccentricity (ovality) ranging between zero and unity (to ensure convexity of the shell), s is the circumferential coordinate (see Figure 1) and L_0 is the circumferential length of the oval measured along the centreline of the wall thickness.

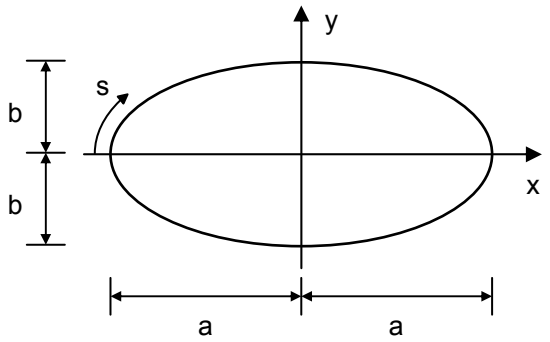

Figure 1. Geometry of oval sections

Eq. (2) defines the geometry of an ellipse. The nature of the expression enables direct and straightforward determination of many of the geometric properties, whilst other properties may be calculated by integration. Standardised section properties may be obtained from prEN 10210-2 (2003) [4]. The oval hollow sections described in the current study are of elliptical geometry.

$$\left(\frac{x}{a}\right)^2 + \left(\frac{y}{b}\right)^2 = 1 \quad (2)$$

where x and y are the Cartesian coordinates and a and b are the major and minor radii, respectively (see Figure 1).

Currently, few test results on oval hollow sections exist and there is a limited understanding of their properties and structural performance at both a cross-sectional and member level. Early test results on oval sections of non-metallic materials and of very slender proportions have been conducted by the aeronautical sector, including those by Hutchinson [5], Feinstein *et al.* [6] and Tennyson *et al.* [7]. Tentative design rules for structural oval hollow sections, based on assumed analogies with circular hollow sections have been proposed by the Steel Construction Institute and Corus Tubes [8,9], which although rationally based, have no theoretical, numerical or experimental verification.

The elastic critical buckling and post-buckling behaviour of oval shells first received attention from the aeronautical industry in the 1950s and 1960s, with the principal investigations conducted in the USA. Following examination of the behaviour of shells of varying curvature [3], analyses to predict the elastic critical buckling and post-buckling response of oval hollow sections under axial loading were conducted [10,11]. It was proposed that the elastic critical buckling stress for an oval cross-section subjected to pure compression could be approximated by Eq. (3), derived simply by substituting the maximum radius of curvature of an oval section r_{max} into the classical buckling expression for a circular cylinder [12]. This assumes that buckling would initiate at the point of maximum radius of curvature and ignores the restraining effect of the surrounding material of lower radius of curvature; Eq. (3) is therefore a lower bound solution.

$$\sigma_{cr} = \frac{E\,t}{r_{max}\sqrt{3(1-\nu^2)}} \quad (3)$$

where E is the material Young's modulus, t is the thickness of the cross-section, ν is Poisson's ratio and r_{max} is the maximum radius of curvature of the oval.

For an elliptical section, the maximum radius of curvature occurs at the ends of the minor axis, and may be shown to be equal to a^2/b, where a and b are the major and minor axis radii (Figure 1). Thus, the elastic critical buckling stress for an elliptical cylinder may be approximated by Eq. (4).

$$\sigma_{cr} = \frac{E\,t}{\left(\frac{a^2}{b}\right)\sqrt{3(1-\nu^2)}} \quad (4)$$

Note that for the case where a = b, Eq. (4) reverts exactly to the elastic critical buckling stress of a circular cylinder, whilst for high a/b ratios the critical buckling stress approaches that predicted by the classical buckling expression for a flat plate.

The post-buckling response of a axially compressed circular cylindrical shell differs markedly from that of a flat plate, as indicated schematically by Figure 2. Whereas a flat plate exhibits a stable post-buckling response, the initial post-buckling response of an axially compressed circular cylindrical shell is highly unstable, resulting in high imperfection sensitivity and observed failure loads significantly below those predicted by linear theory. The behaviour of an oval section may be assumed to be intermediate between these two bounds, but the transition point (a/b ratio) between a stable and an unstable post-buckling response and the associated consequences in terms of ultimate load carrying capacity, has been the subject of some debate [5,11,13]. Discrepancies related to whether consideration was being given to the initial post-buckling region or the far post-buckling region, and it has since been demonstrated by experimentation that ultimate loads well in excess of critical buckling loads can be achieved for oval sections of moderate (ξ = 0.5, a/b = 1.40) to extreme (ξ = 1.0, a/b = 2.07) proportions [6].

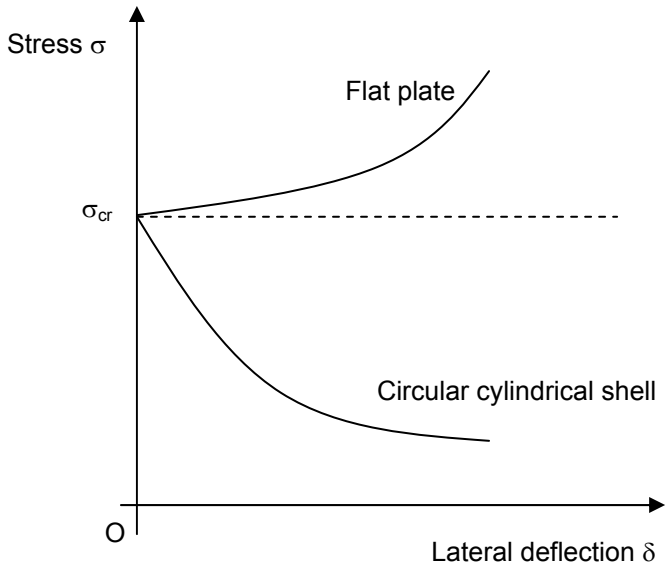

Figure 2. Schematic post-buckling response of an axially compressed circular cylindrical shell and a flat plate

Analysis of the buckling and post-buckling response of oval cylinders in bending and under combined axial compression and bending has also been carried out. For bending about the minor axis, as for pure axial compression, buckling may be assumed to initiate at the point of maximum

radius of curvature, which now also corresponds to the point of maximum compressive stress. For bending about the major axis, buckling, in general, initiates neither at the point of maximum radius of curvature (since this lies on the neutral axis) nor at the point of maximum compressive stress (since the radius of curvature is a minimum at this location). Studies of the point at which buckling initiates in an oval section subjected to combined axial compression and bending (about the major and minor axes) and subsequent examination of the buckling and post-buckling response have been performed and reported [14-16]. The influence of plasticity on the buckling of oval cylinders under axial compression [17] and under bending [18] has also been investigated.

2. LABORATORY TESTING

2.1 Introduction

The investigations described in the previous section have focussed generally on the critical buckling and post-buckling behaviour of slender, elastic oval cylindrical shells of non-structural dimensions. Although fundamental to the understanding of the behaviour of structural oval hollow sections, particularly those with cross-sections of slender proportions where buckling occurs in the elastic material range, this knowledge clearly needs to be supplemented by additional testing and analysis. Two recent experimental programmes to investigate the structural performance of oval hollow sections have been conducted at Imperial College London and at the University of Southampton; the testing details and results of these studies are described herein.

2.2 Imperial College London tests

Since OHS have only recently been introduced, selection of specimens was limited largely by product availability. Three section sizes were obtained: OHS 150x75x6.3, OHS 150x75x8.0 and OHS 300x150x8.0. For each of the two smaller section sizes, two material tensile coupon tests and two stub column tests (in pure compression) were conducted. For the larger section size (OHS 300x150x8.0), three material tensile coupon tests and three stub column tests (in pure compression) were conducted. All material was Grade S355 and supplied by Corus.

2.3 Material tensile coupon tests

Tensile coupon tests were carried out to determine to the basic stress-strain characteristics of the material for each of the tested section sizes. The tensile coupon tests were carried out in accordance with EN 10002-1 (2001) [19].

Parallel coupons were machined longitudinally from the two flattest portions of the cross-sections (i.e. along the centrelines of the ends of the minor axis) using a tipped slot-drill (Figure 3). The nominal dimensions of the tensile coupons were 320×30 mm. Holes were drilled and reamed 20 mm from each end of the coupons for pins to be inserted to prevent slippage of the coupons in the jaws of the testing machine.

Linear electrical strain gauges were affixed at the midpoint of each side of the tensile coupons. A series of overlapping proportional gauge lengths L_0 was marked onto the surface of the coupons; the gauge length of proportional test pieces is related to the original cross-sectional of the test piece S_0 such that $L_0 = 5.65\sqrt{S_0}$. Pressure, strain, displacement and input voltage were all recorded using the data acquisition equipment DATASCAN and logged using the DALITE computer package. All data were recorded at 4 second intervals.

Figure 3. Machining of tensile coupons

The tensile tests were performed using an Amsler 350 kN hydraulic testing machine. Strain rates were within the limits prescribed by EN 10002-1, with fracture occurring, on average, after about 45 minutes.

Mean measured dimensions and key results from the seven coupon tests are reported in Table 1. The stress-strain curves are provided elsewhere [20]. The strain gauges adopted for the OHS 150x75x6.3 and OHS 150x75x8.0 material tests were capable of recording strains up to approximately 1%, whereas for the OHS 300x150x8.0 material tests, high yield strain gauges were utilised enabling strain to be recorded up to approximately 10%. Where material exhibited an upper and lower yield point, it is the lower yield stress that is given in Table 1.

Table 1. Mean measured dimensions and key results from tensile coupon tests

Specimen	Width b_{tc} (mm)	Thickness t (mm)	Young's modulus E (N/mm^2)	Yield stress σ_y (N/mm^2)	Ultimate tensile stress σ_u (N/mm^2)
OHS 150x75x6.3	29.97	6.30	212100	406	517
OHS 150x75x6.3	29.91	6.35	221100	415	541
OHS 150x75x8.0	29.97	8.30	209500	369	502
OHS 150x75x8.0	29.93	8.35	216700	386	518
OHS 300x150x8.0	29.90	7.63	217700	415	536
OHS 300x150x8.0	29.95	7.67	209600	419	537
OHS 300x150x8.0	29.93	7.79	215100	408	524

2.4 Stub column tests

A total of seven Oval Hollow Section (OHS) stub columns were tested in pure axial compression to assess load carrying capacity and deformation capacity. Full load-end shortening curves were recorded, including into the post-ultimate range.

The stub column specimens were cut roughly to length using a rotary hacksaw. Their ends were milled flat and square to a tolerance of ±0.02 mm to achieve accurate seating in the testing machine. Prior to testing, strain visualisation grids were marked onto the surface of the specimens, and measurements of geometry, including initial imperfections were taken.

The nominal lengths of the stub columns were chosen such that they were sufficiently short not to fail by overall buckling, yet still long enough to contain a representative residual stress pattern. A trial stub column test where the length of the specimen was 3 times the larger cross-sectional dimension displayed evidence of overall buckling effects. Subsequent stub column lengths were therefore taken as two times the larger cross-sectional dimension.

Testing of the four OHS 150x75 was carried out in a self-contained 300 T Amsler hydraulic testing machine (Figure 4a), whilst the three larger OHS 300x150 were tested in a purpose-built test rig (Figure 4b). Both set-ups were load-controlled through an Amsler control cabinet. The end platens of both testing arrangements were fixed flat and parallel.

(a) OHS 150x75 (b) OHS 300x150

Figure 4. Testing arrangements for stub columns

Three linear variable displacement transducers (LVDTs) were used to determine the end shortening of the stub columns, between the end platens of the testing machine. Figure 5 shows a schematic view of their layout. Four linear electrical resistance strain gauges were affixed to each specimen at mid-height, and at a distance of four times the material thickness from the major axis. The strain gauges were initially used for alignment purposes. Load, strain, displacement, and input voltage were all recorded using the data acquisition equipment DATASCAN and logged using the DALITE computer package. All data were recorded at 2 second intervals.

Alignment of the specimens was necessary to ensure that the compressive load was introduced concentrically. This was carried out by applying a small alignment load to the specimens, approximately 10% of the predicted failure load $F_{u,pred}$ and observing the variation in strain around the cross-section. In all cases the variation between strains at any point from the average strain was

less than 5%. Linearity of the stress-strain plot was used to confirm that the alignment load was below the proportional limit.

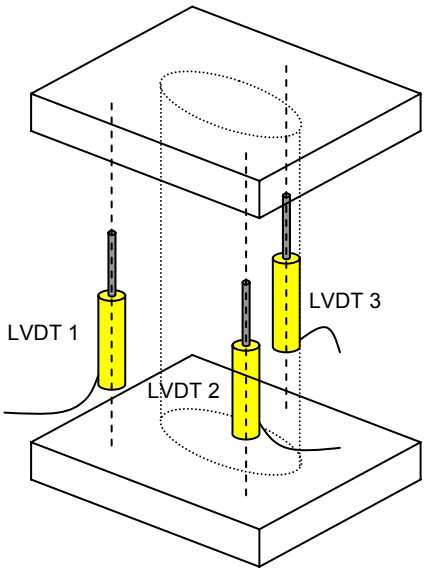

Figure 5. Location of displacement transducers

Loading rates during testing were set such that ultimate load would be reached after 30-45 minutes, and the test would be completed following an appropriate amount of unloading after 60-80 minutes.

Measurements of major and minor axis diameters, material thickness and stub column length were taken at four different points. The mean measured dimensions for the stub column specimens are presented in Table 2. The cross-sectional area A_c of the test specimens was calculated from the measured values of major and minor axis outer diameters and thickness, through Eq. (5).

$$\text{Cross-sectional area } A_c = \pi AB - \pi(A-2t)(B-2t) \quad (5)$$

Table 2. Mean measured dimensions of stub column specimens

Specimen	Major axis outer diameter 2a (mm)	Minor axis outer diameter 2b (mm)	Thickness t (mm)	Area A_c (mm^2)	Length L (mm)
OHS 150x75x6.3 – SC1	149.83	74.87	6.52	2168	451.3
OHS 150x75x6.3 – SC2	150.24	75.16	6.34	2118	298.5
OHS 150x75x8.0 – SC1	150.11	75.10	8.66	2828	302.6
OHS 150x75x8.0 – SC2	149.17	75.07	8.51	2770	297.2
OHS 300x150x8.0 – SC1	299.67	149.99	7.95	5417	598.7
OHS 300x150x8.0 – SC2	300.04	149.79	7.97	5432	599.4
OHS 300x150x8.0 – SC3	301.64	148.90	7.80	5329	600.1

Measurements of local initial geometric imperfections are important in aiding the explanation of structural response and in the development of numerical models. Schafer and Peköz [21] conducted a detailed assessment of initial geometric imperfections on cold-formed channel sections. In their experimental set-up, the specimens were mounted on the table of a milling machine, and a displacement transducer, fitted in the head of the milling machine, was employed to trace the local geometric imperfections. A similar arrangement was adopted by Gardner and Nethercot [22] and in

the present study (Figure 6), whereby, a mechanical dial gauge indicator was fitted into the head of the milling machine, and the specimens were clamped to the bed. An automatic feed was used to pass the specimen under the dial gauge indicator, along its length. Readings were taken at regular intervals along the centreline of the minor axes of the specimens (Figure 7).

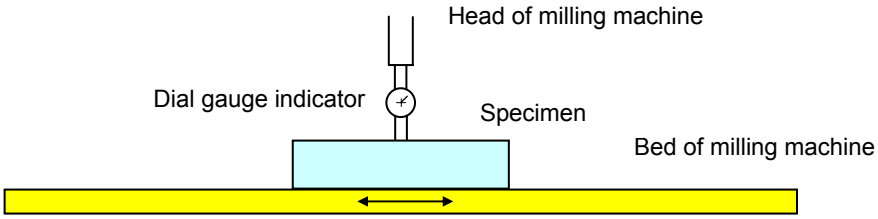

Figure 6. Initial imperfection measurement set-up

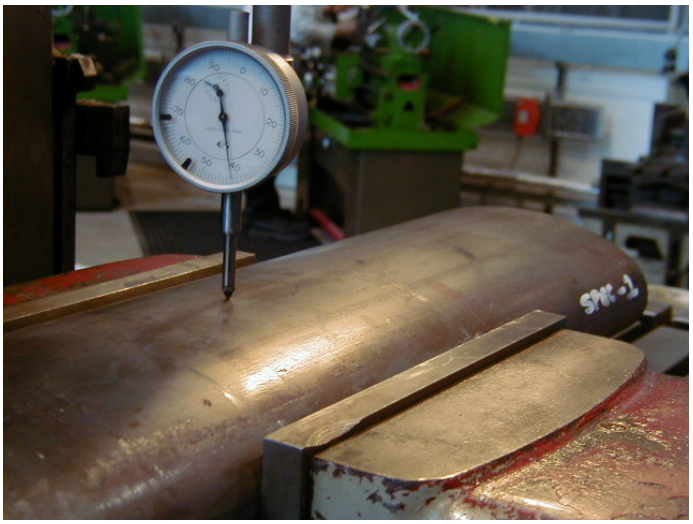

Figure 7. Measurement of initial geometric imperfections

Table 3 presents the maximum initial geometric imperfection magnitudes that were measured along the centrelines of the minor axes of each of the section sizes. The datum for the imperfection measurements is a straight line connecting the ends of each stub column face.

Table 3. Maximum magnitudes of initial geometric imperfections for tested section sizes

Specimen	Mean measured maximum imperfection (mm)
OHS 150x75x6.3	0.061
OHS 150x75x8.0	0.562
OHS 300x150x8.0	0.633

Compression tests on stub columns reveal the average compressive response of the cross-sections. Ultimate failure is due to local buckling of the cross-section. For cross-sections comprising slender elements local buckling may occur in the elastic material range. For more stocky cross-sections, local buckling will occur following significant inelastic deformation.

Measured end shortening readings from the LVDTs were modified on the basis of the strain gauge readings to account for the elastic deformation of the end platens (that are present in the LVDT

measurements). Thus true end shortening values were derived, and are utilised in the remainder of this study.

Load-end shortening curves from the stub column tests are shown in Figures 8 to 10. Note that the two OHS 150x75x6.3 stub columns are of differing length (resulting in differing load-end-shortening behaviour, as shown in Figure 8). The full load-end shortening curve was not recorded for OHS 300x150x8.0 – SC3.

All stub columns exhibited a similar failure mode whereby the two wider faces of the cross-sections buckled locally. All sections displayed a single half wave across the width of the section, indicating characteristics more closely associated with plate behaviour than shell behaviour. Photographs of deformed test specimens (OHS 150x75x8.0 – SC1 and OHS 300x150x8.0 – SC1) are shown in Figure 11.

A summary of the results from the stub column tests is presented in Table 4. For each test, the ultimate load and the end shortening at ultimate load have been tabulated.

Table 4. Summary of results from stub column tests

Specimen identification	Ultimate load F_u (kN)	End shortening at F_u (mm)
OHS 150x75x6.3 – SC1	931	13.7
OHS 150x75x6.3 – SC2	952	10.5
OHS 150x75x8.0 – SC1	1367	18.1
OHS 150x75x8.0 – SC2	1435	18.8
OHS 300x150x8.0 – SC1	2777	1.6
OHS 300x150x8.0 – SC2	2792	1.7
OHS 300x150x8.0 – SC3	2574	-

2.5 University of Southampton tests

An experimental study into the minor axis bending behaviour of structural OHS was conducted at the University of Southampton [23]. A four-point bending arrangement was employed for all tests. Three different section sizes were considered, OHS 150x75x5.0, OHS 150x75x6.3 and OHS 150x75x8.0; each test was repeated three times, resulting in the total of nine tests. A tensile coupon test was conducted on material from each of the nine test specimens. All material was Grade S355 and supplied by Corus.

2.6 Material tensile coupon tests

Tensile coupon tests were conducted on material cut from each of the nine bending test specimens. The nominal dimensions of the coupons were 200 mm x 20 mm. The tests were displacement controlled and utilised Instron testing machinery. A summary of the results is provided in Table 5, though other than geometric measurements, only yield stress was reported.

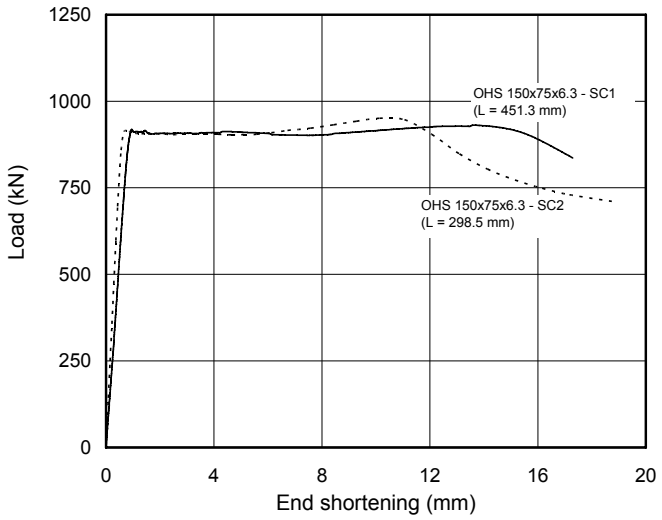

Figure 8. Load-end shortening curves for OHS 150x75x6.3 stub columns

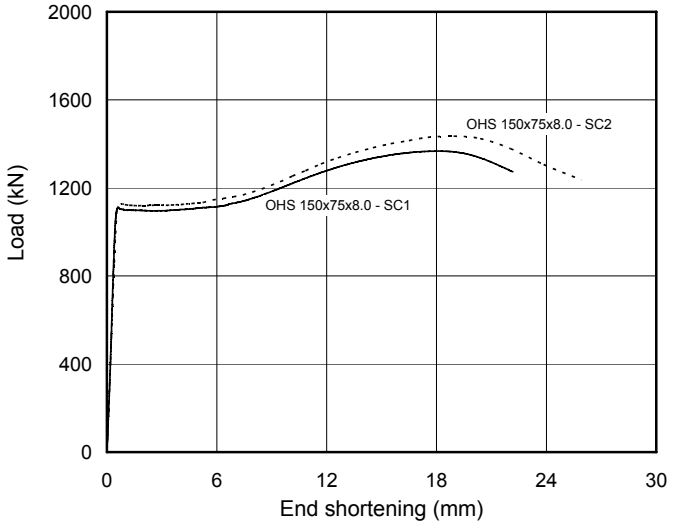

Figure 9. Load-end shortening curves for OHS 150x75x8.0 stub columns

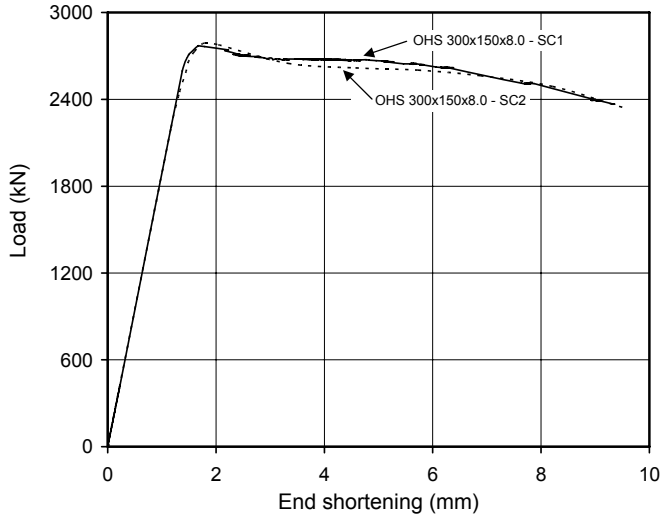

Figure 10. Load-end shortening curves for OHS 300x150x8.0 stub columns

(a) OHS 150x75x8.0 – (b) OHS 300x150x8.0 –

Figure 11. Deformed stub column test specimens

Table 5. Minimum measured dimensions and yield stress from tensile coupon tests

Specimen	Width b (mm)	Thickness t (mm)	Yield stress σ_y (N/mm^2)
OHS 150x75x5.0 – C1	19.93	5.21	367
OHS 150x75x5.0 – C2	20.00	5.11	363
OHS 150x75x5.0 – C3	20.09	5.11	360
OHS 150x75x6.3 – C1	19.97	6.40	380
OHS 150x75x6.3 – C2	19.96	6.44	387
OHS 150x75x6.3 – C3	19.96	6.38	386
OHS 150x75x8.0 – C1	19.92	8.29	366
OHS 150x75x8.0 – C2	19.91	8.32	362
OHS 150x75x8.0 – C3	19.96	8.60	372

Note that the number of the coupon tests (C1, C2 and C3) relates directly to material cut from the bending test specimens (B1, B2 and B3, respectively).

2.7 In-plane bending tests

The in-plane minor axis bending tests were conducted in a symmetrical four-point bending arrangement as illustrated in Figure 12. The nominal dimensions for L_1, L_2 and L_3 were 1100 mm, 800 mm and 1100 mm respectively, with the measured dimensions given in Table 6. Mean measured cross-sectional dimensions of the test specimens are provided in Table 7.

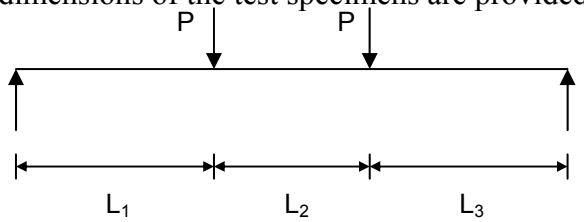

Figure 12. Four-point bending loading arrangement

Table 6. Measured dimensions for four-point bending arrangements

Specimen	L_1 (mm)	L_2 (mm)	L_3 (mm)
OHS 150x75x5.0 – B1	1089	799	1088
OHS 150x75x5.0 – B2	1089	800	1091
OHS 150x75x5.0 – B3	1090	799	1089
OHS 150x75x6.3 – B1	1088	798	1090
OHS 150x75x6.3 – B2	1091	800	1090
OHS 150x75x6.3 – B3	1090	800	1089
OHS 150x75x8.0 – B1	1089	799	1093
OHS 150x75x8.0 – B2	1088	799	1089
OHS 150x75x8.0 – B3	1090	800	1091

Table 7. Mean measured cross-sectional dimensions for bending specimens

Specimen	Major axis outer diameter 2a (mm)	Minor axis outer diameter 2b (mm)	Thickness t (mm)[1]	Area A_c (mm^2)[1]
OHS 150x75x5.0 – B1	150.5	73.9	5.2	1763
OHS 150x75x5.0 – B2	150.6	74.2	5.2	1758
OHS 150x75x5.0 – B3	150.4	74.6	5.2	1766
OHS 150x75x6.3 – B1	150.2	72.6	6.7	2195
OHS 150x75x6.3 – B2	150.2	73.5	6.7	2217
OHS 150x75x6.3 – B3	150.4	73.6	6.7	2224
OHS 150x75x8.0 – B1	148.8	73.8	8.8	2823
OHS 150x75x8.0 – B2	148.9	72.8	8.8	2828
OHS 150x75x8.0 – B3	148.8	73.0	9.0	2879

Note 1: Area A_c and thickness t were calculated from measured mass and density

The results of the bending tests are summarised in Table 8. For each specimen, the maximum test bending moment M_u attained and the average vertical deflection at the loading points at maximum load δ_u are given. Full bending moment-deflection graphs for the nine test specimens are shown in Figures 13 to 15.

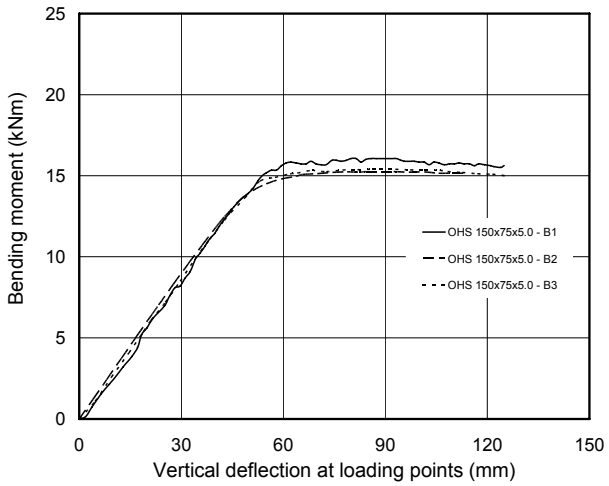

Figure 13. Bending moment–deflection curves for OHS 150x75x5.0 beams

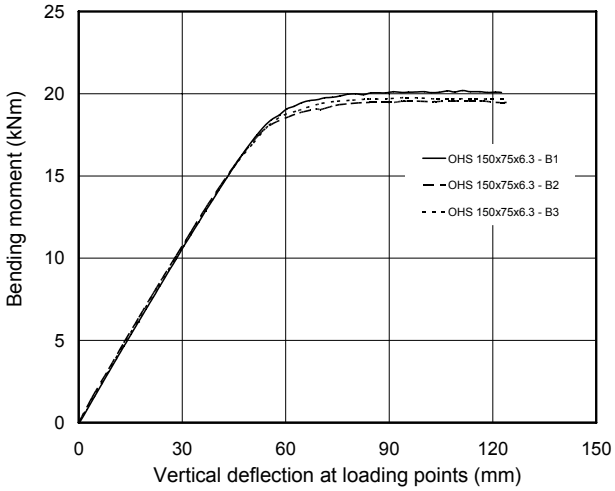

Figure 14. Bending moment–deflection curves for OHS 150x75x6.3 beams

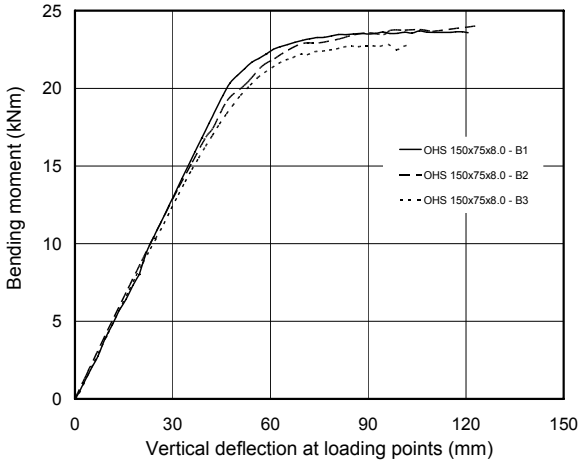

Figure 15. Bending moment–deflection curves for OHS 150x75x8.0 beams

Table 8. Summary of results from bending tests

Specimen	Ultimate moment M_u (kNm)	Deflection at ultimate moment δ_u (mm)
OHS 150x75x5.0 – B1	16.1	87
OHS 150x75x5.0 – B2	15.3	87
OHS 150x75x5.0 – B3	15.4	87
OHS 150x75x6.3 – B1	20.2	111
OHS 150x75x6.3 – B2	19.6	116
OHS 150x75x6.3 – B3	19.8	97
OHS 150x75x8.0 – B1	23.7	106
OHS 150x75x8.0 – B2	24.0	124
OHS 150x75x8.0 – B3	22.9	103

3. NUMERICAL MODELLING

3.1 Introduction

A numerical modelling programme was carried out in parallel with the experimental programme at Imperial College London. The initial aim of the numerical work was to replicate the experimental compression and bending behaviour numerically. Subsequent studies were performed to investigate the sensitivity of the models to variation in the key input parameters. All numerical modelling was performed using the non-linear finite element (FE) analysis package, ABAQUS version 6.4 [24].

3.2 Development of FE models

3.2.1 General

The elements chosen for the FE models were 4-noded, reduced integration shell elements, designated as S4R in the ABAQUS element library, and are suitable for thin or thick shell applications [24]. Convergence studies were conducted to decide upon an appropriate mesh density, with the aim of achieving suitably accurate results whilst minimising computational time. Linear elastic eigenmode simulations were conducted to provide buckling modes to be used as initial imperfections in subsequent non-linear analyses. The modified Riks method [24] was employed to solve the geometrically and materially non-linear stub column and beam models. The modified Riks method is an algorithm that enables effective solutions to be found to unstable problems (e.g. post-ultimate response of compression or flexural members), and adequately traces non-linear unloading paths.

3.2.2 Material modelling

ABAQUS requires that material behaviour be specified by means of a multi-linear stress-strain curve, defined in terms of true stress and log plastic strain. The relationships between true stress and engineering stress, σ_{true} and σ_{nom}, respectively, and log plastic strain and engineering strain, ε_{ln}^{pl} and ε_{nom}, respectively, are given in Eqs. (6) and (7) respectively. Engineering stress and strain are of course the nominal values that are recorded from an uniaxial stress-strain coupon test.

$$\sigma_{true} = \sigma_{nom} (1 + \varepsilon_{nom}) \quad (6)$$

$$\varepsilon_{ln}^{pl} = \ln (1 + \varepsilon_{nom}) - \frac{\sigma_{true}}{E} \quad (7)$$

The measured material properties taken from the tensile coupon tests were adopted in all cases. Where incomplete stress-strain data were available average properties (such as Young's modulus) from the remaining coupon tests were used; this was deemed acceptable since there was little variation in material properties between specimens.

3.2.3 Residual stresses and initial geometric imperfections

Residual stresses were not incorporated in the FE models in this study. The reason for this was two-fold. Firstly, no residual stress measurements have been conducted on structural steel oval hollow sections, and secondly, there was no evidence of residual stresses during the preparation of the tensile coupons (that were machined from within the completed oval hollow sections); i.e. the deformation of the coupons as they were released from the surrounding material was very small. However, residual stresses may have been induced as a result of thermal action in the University of Southampton bending tests, where plates were welded to the specimens at the loading and support points. Residual stress measurements would be useful in future studies.

For the stub column models local geometric imperfections of the form of the lowest eigenmode were included in the non-linear analysis. The shape of the three lowest eigenmodes for OHS 150x75.6.3 – SC2 are shown in Figure 16. For the bending models, both local and global geometric imperfections were included in the models. To generate the imperfection modes for the beam models, the bending arrangement was initially replaced by an axial compression arrangement with pin-ends; subsequently, for the non-linear bending analysis, the local imperfection took the form of the lowest local buckling mode and the global imperfection took the form of the lowest global buckling mode.

Due to the limited detail of imperfection measurements, the local imperfection amplitude for the stub columns was considered as a series of fixed fractions of the material thickness (t/10, t/100 and t/500), whilst the global imperfection amplitude for the beam models was taken as a fixed fraction of the beam length (L/2000).

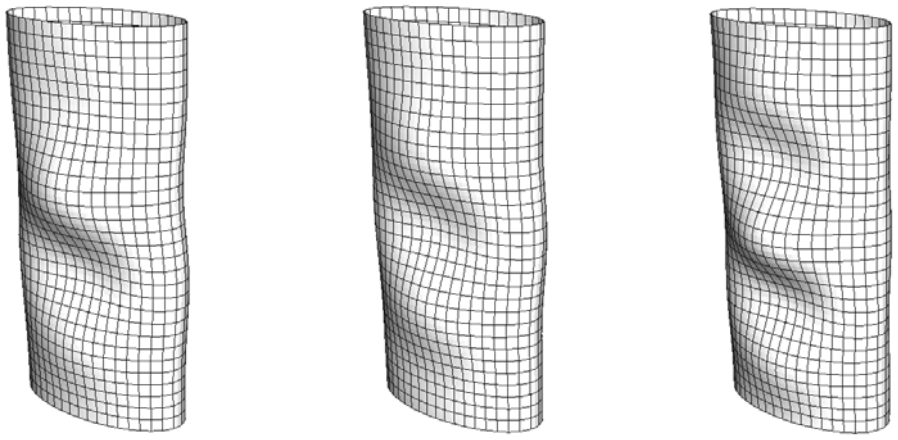

Figure 16. Three lowest eigenmodes for OHS 150x75x6.3 – SC2

3.3 Simulation of tests

3.3.1 Stub column tests

The stub column tests were modelled using the measured dimensions of the test specimens, material stress-strain data from the corresponding tensile tests and geometric imperfections of the form of the lowest elastic eigenmode. To assess the sensitivity of the models to variation in imperfections, three different amplitudes were considered – t/10, t/100 and t/500, where t is the material thickness. Boundary conditions were applied to model fixed ends. This was achieved by restraining all displacements and rotations at the base of the columns, and all bar vertical displacement at the loaded end of the stub column. Constraint equations were used to ensure that the loaded end of the stub column remained in a horizontal plane.

A comparison of the FE results with the test results for the stub columns is given in Table 9; values of ultimate load F_u and deformation at ultimate load δ_u are compared. Table 9 demonstrates that test ultimate load can generally be closely predicted numerically, and is relatively insensitive to imperfection amplitude. In all cases the ultimate load in under-predicted; this is assumed to be largely due to inaccurate material modelling (including use of tensile coupon tests to represent compressive stress-strain properties). However, the deformation at ultimate load is very sensitive to the exact level of imperfection, and this is not reliably predicted using the described models. This is a commonly observed problem and due principally to the sensitivity of numerical models at points of very low stiffness (i.e. near ultimate load, a small increment of load corresponds to a very large increment of deformation). This matter will receive further attention in future studies.

Table 9. Comparison of FE and test results for OHS stub columns

Imperfection amplitude	t / 500		t / 100		t / 10	
Specimen identification	FE F_u / Test F_u	FE σ_u / Test σ_u	FE F_u / Test F_u	FE σ_u / Test σ_u	FE F_u / Test F_u	FE σ_u / Test σ_u
OHS 150x75x6.3 – SC1	0.99	0.39	0.99	0.38	0.97	0.07
OHS 150x75x6.3 – SC2	0.96	0.23	0.96	0.18	0.92	0.06
OHS 150x75x8.0 – SC1	0.83	0.83	0.83	0.82	0.79	0.04
OHS 150x75x8.0 – SC2	0.80	0.81	0.79	0.81	0.75	0.04
OHS 300x150x8.0 – SC1	0.95	0.93	0.95	0.99	0.93	0.91
OHS 300x150x8.0 – SC2	0.95	0.97	0.95	0.97	0.92	0.91

Figure 17 compares the load-end shortening response of the OHS 300x150x8.0 – SC1 test with the FE models containing the three different imperfection amplitudes. Note that the results of the FE models with imperfection amplitudes of t/100 and t/500 are almost coincident.

The failure modes of the FE models were similar to those observed in the tests. An example of a deformed FE stub column model (OHS 150x75x6.3 – SC1) is shown in Figure 18.

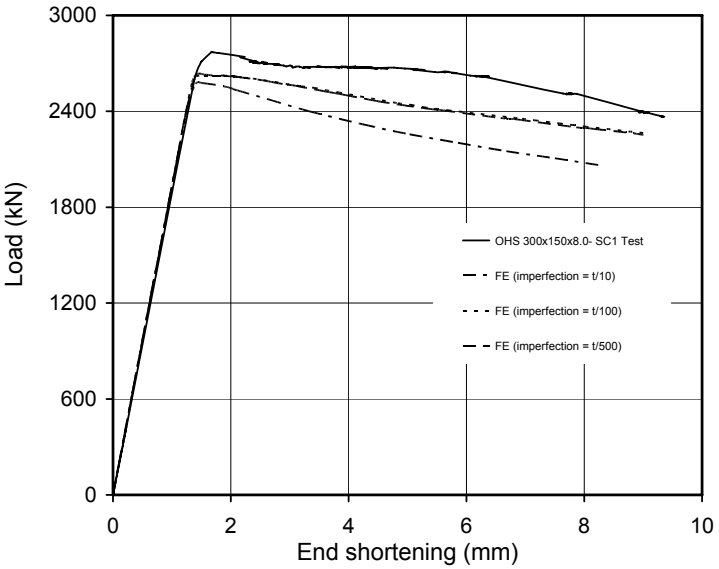

Figure 17. Comparison between test and FE model of OHS 300x150x8.0 – SC1 stub column

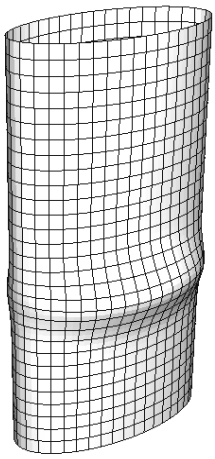

Figure 18. Deformed FE model of OHS 150x75x6.3 stub column

3.3.2 Bending tests

The bending tests conducted at the University of Southampton were modelled using the measured dimensions of the test specimens, material stress-strain data from the corresponding tensile tests and local and global geometric imperfections of the form of the lowest elastic eigenmodes. Since only values of yield strength were reported from the University of Southampton tests, mean values of other material properties such as Young's modulus and ultimate strength were assumed as the mean values from the Imperial College London tests. Initial studies demonstrated that the models were not sensitive to variation in imperfection amplitude; therefore a local imperfection amplitude of t/100 and a global imperfection amplitude of L/2000 were employed throughout the study. A general view of the FE model of the bending set-up is shown in Figure 19.

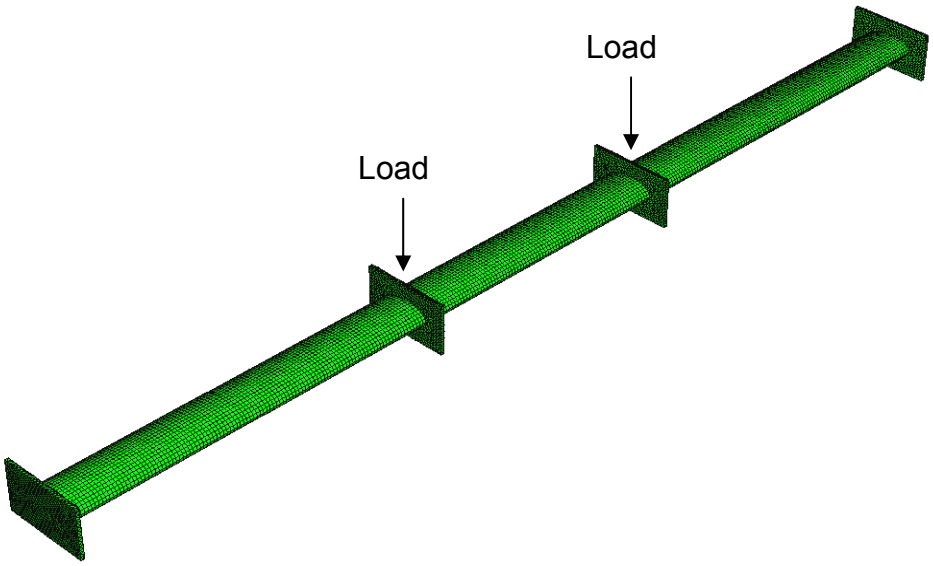

Figure 19. General view of FE model of bending set-up

A comparison of the FE results with the test results for the beams is given in Table 10; values of ultimate moment M_u and average vertical deflection at the loading points at ultimate moment δ_u are compared. Graphical comparisons between test and FE results for bending moment versus vertical displacement at the loading points are shown in Figures 20 to 22.

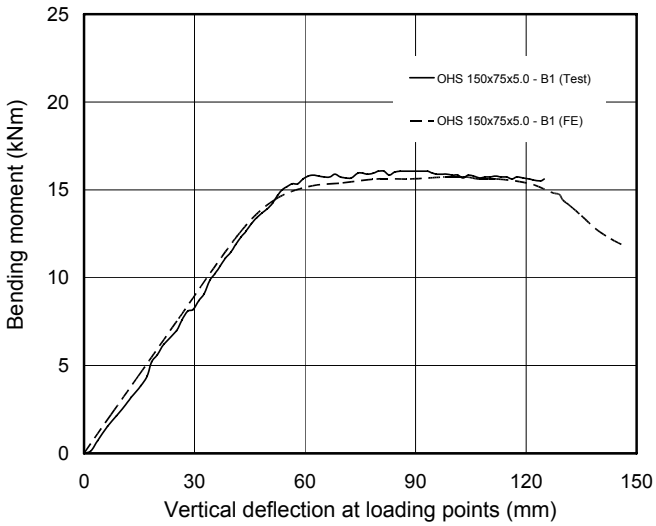

Figure 20. Comparison of bending moment versus deformation for OHS 150x75x5.0 – B1

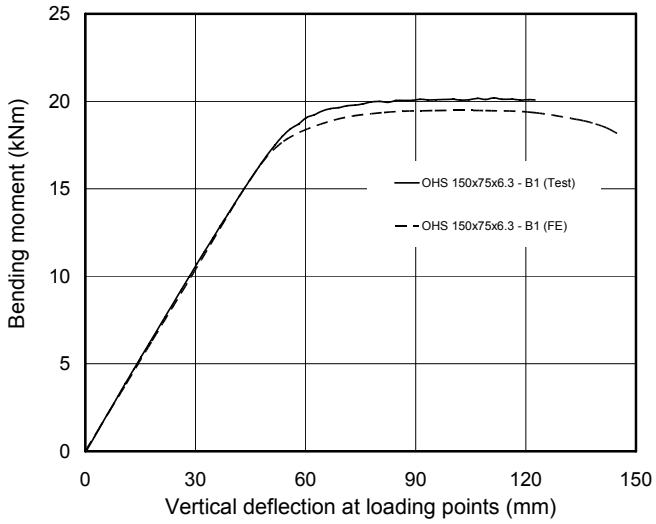

Figure 21. Comparison of bending moment versus deformation for OHS 150x75x6.3 – B1

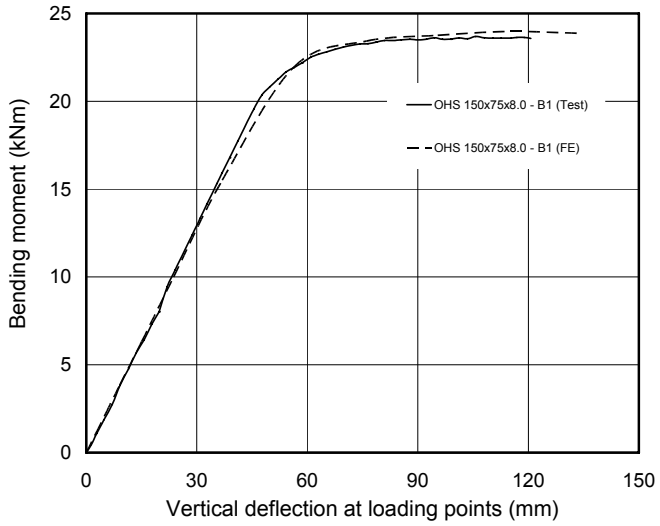

Figure 22. Comparison of bending moment versus deformation for OHS 150x75x8.0 – B1

Table 10. Comparison of FE and test results for OHS beams

Specimen	FE ultimate moment M_u (kNm)	FE deflection at ultimate moment δ_u (mm)	FE M_u / Test M_u	FE σ_u / Test σ_u
OHS 150x75x5.0 – B1	15.7	101	0.98	1.16
OHS 150x75x5.0 – B2	15.7	99	1.03	1.14
OHS 150x75x5.0 – B3	15.7	99	1.02	1.14
OHS 150x75x6.3 – B1	19.5	102	0.97	0.92
OHS 150x75x6.3 – B2	19.5	104	0.99	0.90
OHS 150x75x6.3 – B3	19.6	104	0.99	1.07
OHS 150x75x8.0 – B1	24.0	115	1.01	0.98
OHS 150x75x8.0 – B2	23.9	116	1.00	0.94
OHS 150x75x8.0 – B3	24.1	115	1.05	1.12

The FE failure modes mirrored the test failure modes, with in-plane bending only. The bending was generally symmetrical, though in some cases non-symmetrical deformations were observed beyond the ultimate bending moment (due to slight non-symmetry in the test geometry). A typical FE failure mode is shown in Figure 23.

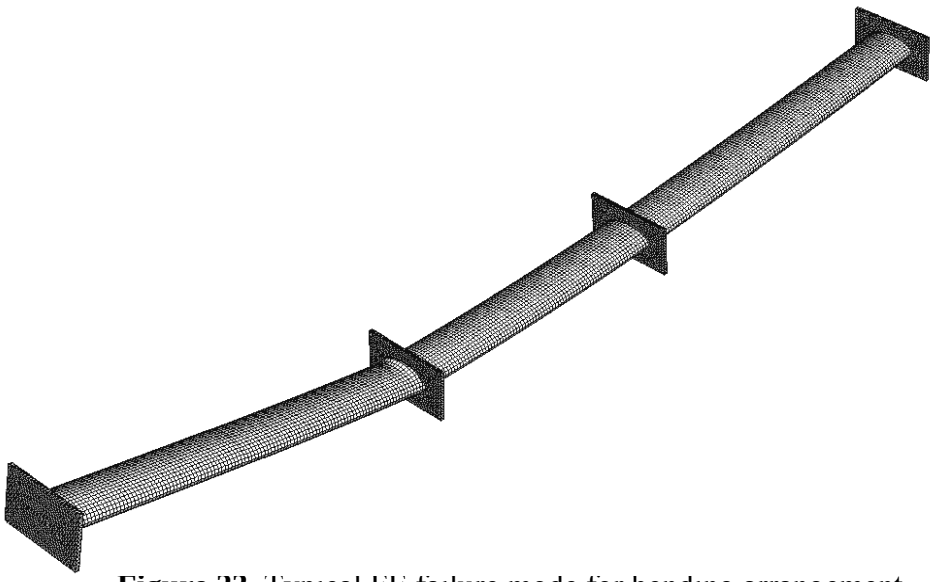

Figure 23. Typical FE failure mode for bending arrangement

3.4 Parametric studies

Following the satisfactory agreement between test and FE model behaviour, this section presents parametric studies, intended to analyse trends and generate a greater pool of results.

3.4.1 Stub columns

From the comparison between test and FE stub column behaviour, it was shown that ultimate load was adequately predicted, but deformation at ultimate load was not well predicted. A parametric study has been conducted to determine ultimate loads for stub columns of varying slenderness, with

the results compared against the yield load for each cross-section, to investigate the effects of strain hardening for the stocky sections and elastic local buckling in the slender sections. Variation in slenderness was achieved by altering the thickness of the OHS 150x75. Mean values for material properties were taken from the tensile tests performed at Imperial College London, whilst initial geometric imperfections were taken as the lowest eigenmode with an amplitude of t/500. The results are presented in Table 11.

Table 11. Results of parametric study to investigate stub column behaviour

Section	FE ultimate load F_u (kN)	Calculated yield load F_y (kN)	F_u / F_y
OHS 150x75x3.0	379	424	0.89
OHS 150x75x4.0	506	560	0.90
OHS 150x75x5.0	636	694	0.92
OHS 150x75x6.3[1]	919	875	1.05
OHS 150x75x8.0[1]	1130	1058	1.07

Note: [1] Replication of test

The results demonstrate that the two stockier sections (OHS 150x75x6.3 and OHS 150x75x8.0) are capable of achieving and exceeding their respective yield loads. The more slender OHS 150x75x5.0, OHS 150x75x4.0 and OHS 150x75x3.0 do not reach their yield load due to the effects of local buckling in the elastic material range, which, as expected, can be seen to be more detrimental with increasing slenderness.

3.4.2 Beams

From the comparison between tests and FE bending behaviour, it was shown that the ultimate moment, deformation at ultimate moment, and indeed the full bending moment-deformation history was well predicted. Thus a parametric study has been conducted to generate bending moment-deformation histories for a range of cross-section slenderness. As with the stub column models, this was achieved through variation in section thickness. Material properties were taken as the mean values from the tensile tests conducted at the University of Southampton on material cut from the bending specimens. Local and global imperfections were introduced as described previously in this paper.

The results of the parametric study are shown in Figure 24, with the bending moments normalised by the plastic bending resistance of each of the cross-sections.

Figure 24 demonstrates, as expected, that the stockier the cross-section the higher the deformation capacity. The 5.0 mm, 6.3 mm, 8.0 mm and 10.0 mm models all reach the calculated cross-sectional plastic bending resistance. The 3.0 mm and 4.0 mm models display a lower deformation capacity and do not reach the full plastic bending resistance. The 3.0 mm model reached 92% of the plastic bending resistance, whilst the 4.0 mm model reached 97%. Both of these sections exceeded their elastic bending resistances.

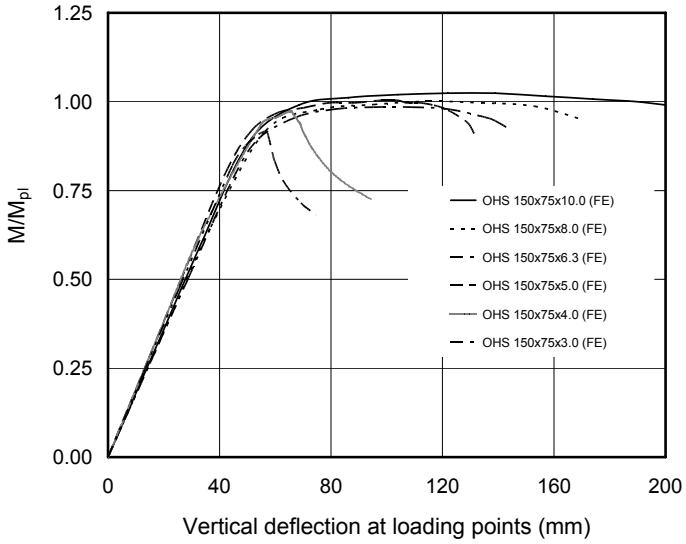

Figure 24. Effect of cross-section slenderness on bending behaviour

4. COMPARISON WITH PRELIMINARY DESIGN GUIDANCE

A preliminary method for the section classification of oval hollow sections under the individual loading conditions of axial compression, minor axis bending and major axis bending has been drafted [9]; combined loading was not considered. The classification limits are those contained in prEN 1993-1-1 (2003) [25] for circular hollow sections, but the section slenderness is defined based on an equivalent diameter D_e, to account for the continuously varying curvature. The classification limits for axial compression and for minor axis bending, with which to compare the diameter-to-thickness ratio (D/t) of a circular section (or D_e/t for an oval section) are 50 ε^2 for Class 1, 70 ε^2 for Class 2 and 90 ε^2 for Class 3, where $\varepsilon = (235/\sigma_y)^{0.5}$ and σ_y is the material yield strength. General guidance on the use of EN 1993-1-1 is available [26].

For the configurations considered in the current study (i.e. axial compression and minor axis bending), the equivalent diameter D_e used to determine the section slenderness is taken as that of an equivalent circle, as given by Eq. (8), where the symbols have been harmonised with those adopted in the remainder of the paper.

$$D_e = 2a\sqrt{\frac{a}{b}} \tag{8}$$

As shown in Figure 25, the equivalent circle approximately follows the continuously varying curvature of the oval.

The calculated D_e/t ratios of the tested specimens and three additional finite element models are given in Table 12, along with their corresponding section classification. EN 1993-1-1 defines four classes of cross-section. Under pure compression, Class 1-3 specimens are capable of reaching their squash (or yield) load F_y, defined as the gross area multiplied by the material yield strength, whilst Class 4 sections fail at a lower load due to local buckling in the elastic material range. In Table 12, the ultimate test (or FE) load F_u is normalised by the squash load F_y, and the relationship between F_u/F_y and cross-section slenderness $D_e/t\varepsilon^2$ is plotted in Figure 26. A value of F_u/F_y greater than unity represents meeting of the Class 1-3 requirements, whilst a value less than unity indicates a Class 4 section where local buckling prevents the yield load being reached. Figure 26 exhibits the

anticipated trend of reducing values of F_u/F_y with increasing slenderness, and indicates that a Class 3 slenderness limit of $90\varepsilon^2$ is reasonable, but requires further investigation.

Table 12. Section classification in compression

Specimen	Equivalent diameter D_e (mm)	Thickness t (mm)	D_e/t	F_u/F_y	Classification
OHS 150x75x6.3 – SC1	211.96	6.52	32.5	1.06	Class 2
OHS 150x75x6.3 – SC2	212.41	6.34	33.5	1.08	Class 2
OHS 150x75x8.0 – SC1	212.22	8.66	24.5	1.31	Class 1
OHS 150x75x8.0 – SC2	210.28	8.51	24.7	1.34	Class 1
OHS 300x150x8.0 – SC1	423.58	7.95	53.3	1.24	Class 4
OHS 300x150x8.0 – SC2	424.65	7.97	53.3	1.24	Class 4
OHS 300x150x8.0 – SC3	429.32	7.80	55.0	1.18	Class 4
FE OHS 150x75x5.0	212.13	5.00	42.4	0.92	Class 3
FE OHS 150x75x4.0	212.13	4.00	53.0	0.90	Class 4
FE OHS 150x75x3.0	212.13	3.00	70.7	0.89	Class 4

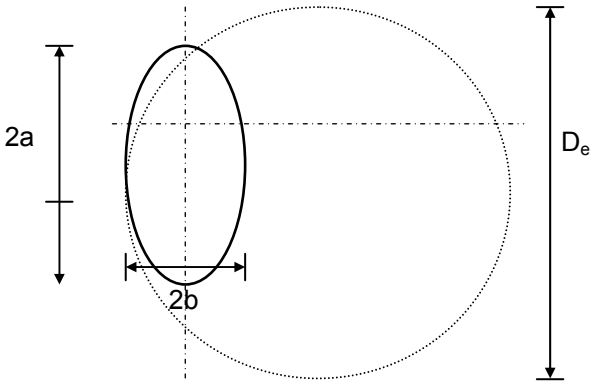

Figure 25. Illustration of equivalent diameter

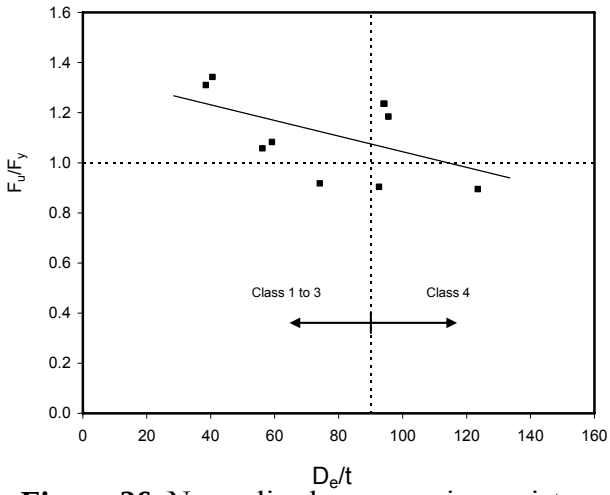

Figure 26. Normalised compressive resistance versus cross-section slenderness

It may be observed from Table 12 and Figure 26 that the three OHS 300x150x8.0 stub columns have performed better than expected, with the F_u/F_y values (of around 1.2) indicating a high degree of strain hardening. However, inspection of the load-end shortening curves of Figure 10 does not support this result and the high values of F_u/F_y are believed to be due to normalisation of the ultimate stub column load in compression by the yield load in tension, and assuming symmetrical stress-strain behaviour in tension and compression. Normalisation could alternatively be made against the stub column stress-strain curve itself or against compressive coupon data. Normalisation against the stub column curve itself is generally inappropriate since the material behaviour is influenced by the effects of local buckling (which may preclude reaching yield), initial imperfections and residual stresses. Normalisation against the compressive stress-strain curve is preferable and this will be generated as part of future studies. The finite element models of the stub columns are based on tensile properties and this issue therefore does not arise.

Results of the nine tested beams and six modelled beams (generated as part of the parametric finite element study and shown in Figure 24) are presented in Figure 27. The ultimate moments attained in the tests (or FE models) M_u have been normalised against the plastic moment resistances M_{pl} (calculated as the plastic modulus multiplied by the material yield strength) and plotted against cross-section slenderness $D_e/t\varepsilon^2$ in Figure 27, where the section classification limits are also included. In bending, Class 1 cross-sections are capable of reaching and maintaining their full plastic moment (and may therefore be used in plastic design). Class 2 cross-sections are also capable of reaching their full plastic moment in bending but have a somewhat lower deformation capacity. In Class 3 cross-sections local buckling prevents attainment of the full plastic moment and the bending moment resistance is therefore limited to the (elastic) yield moment. For Class 4 cross-sections, local buckling occurs in the elastic range for which an effective cross-section is defined based on the width-to-thickness (or diameter-to-thickness) ratios of constituent elements, and this is used to determine the cross-sectional bending resistance.

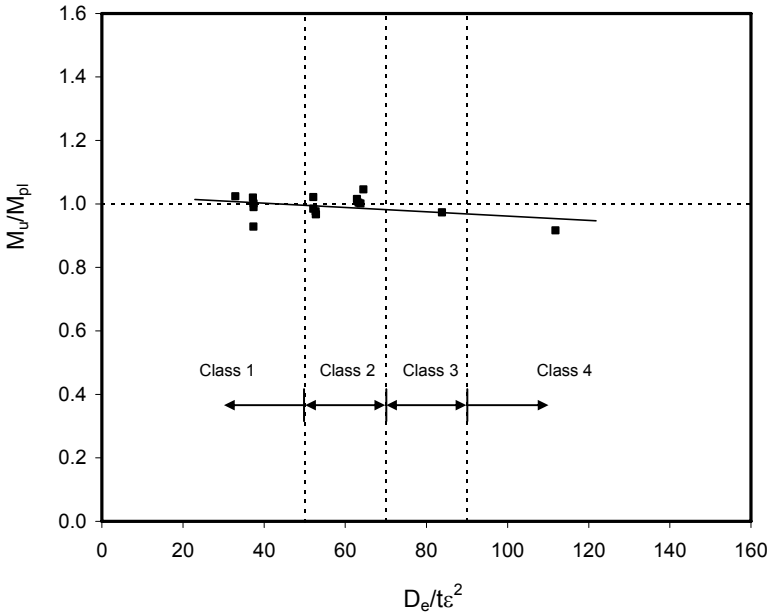

Figure 27. Normalised bending resistance versus cross-section slenderness

From Figure 27, the anticipated trend of decreasing moment resistance with increasing cross-section slenderness may be observed. The proposed classification limits are broadly acceptable, though some of the Class 1 and 2 cross-sections have not performed as would be expected – this apparent under-performance may be associated with the normalisation method (as discussed above) or variation in geometric properties. The classification limits will be reviewed on the basis of the results of further testing and finite element modelling which is currently underway.

5. CONCLUSIONS

This paper has provided an introduction to the behaviour of structural oval hollow sections and described a series of material and cross-section tests conducted at Imperial College London. In total 7 stub column tests and 7 tensile coupon tests were conducted. Further tests carried out in minor axis bending at the University of Southampton have also been summarised and reviewed. For all tests, measured geometry and material properties have been tabulated and the key results summarised. Full load-deformation curves for each test have been provided.

In parallel to the testing, a numerical modelling programme using the finite element package ABAQUS has been carried out. For stub column behaviour, ultimate load was generally well

predicted, but deformation at ultimate load was not well predicted. For bending behaviour, the full bending moment-deformation history was consistently well predicted. Parametric studies were performed to investigate the influence of cross-section slenderness on structural response, where both strain hardening and local buckling effects were observed.

The test and finite element results have been compared with preliminary rules for section classification of oval hollow sections. The classification limits have been shown to be broadly acceptable, but require further test and finite element results for a thorough validation. Such data are currently being generated.

ACKNOWLEDGEMENTS

The author would like to thank Corus for the supply of test specimens and for funding contributions, and Eddie Hole (Corus Tubes) and Ken Chan (Imperial College London) for their technical input.

REFERENCES

[1] Gardner, L., "Structural behaviour of oval hollow sections", Proceedings of the Fourth International Conference on Advances in Steel Structures. 13th-15th June, 2005, Shanghai, China, 2005, pp.517-522.

[2] Gardner, L. and Ministro, A., "Structural steel oval hollow sections", The Structural Engineer, 2005, 83(21), pp.32-36.

[3] Marguerre, K., "Stability of cylindrical shells of variable curvature", NACA TM 1302, 1951.

[4] prEN 10210-2, "Hot finished structural hollow sections of non-alloy and fine grain steels - Part 2: Tolerances, dimensions and sectional properties", CEN, 2003.

[5] Hutchinson, J.W., "Buckling and initial post-buckling behaviour of oval cylindrical shells under axial compression", Transactions of the American Society of Mechanical Engineers, Journal of Applied Mechanics, March 1968, pp.66-72.

[6] Feinstein, G., Erickson, B. and Kempner, J., "Stability of oval cylindrical shells: Experimental investigation of initial and ultimate buckling loads of fixed-end, oval cylindrical shells under axial compression", Experimental Mechanics, November 1971, pp.514-520.

[7] Tennyson, R.C., Booton, M. and Caswell, R.D., "Buckling of imperfect elliptical cylindrical shells under axial compression", American Institute of Aeronautics and Astronautics Journal, 1971, 9(2), pp.250-255.

[8] The Steel Construction Institute, "Gross section properties of elliptical hollow sections", The Steel Construction Institute, UK, 2003.

[9] Corus Tubes, "Celsius 355® Ovals – Sizes and Resistances, Eurocode Version", Structural and Conveyance Publication, Corus, 2003.

[10] Kempner, J., "Some results on buckling and post-buckling of cylindrical shells", Collected papers on Instability of Shell Structures, NASA TN D-1510, 1962, pp.173-186.

[11] Kempner, J. and Chen, Y.N., "Large deflections of an axially compressed oval cylindrical shell", Proceedings of the Eleventh International Congress of Applied Mechanics, Munich, Springer-Verlag, Berlin, 1964, pp.299-305.

[12] Donnell, L.H., "A new theory for the buckling of thin cylinders under axial compression and bending", Transactions of the American Society of Mechanical Engineers, 1934, 56, pp.795-806.
[13] Kempner, J. and Chen, Y.N., "Postbuckling of an axially compressed oval cylindrical shell", Proceedings of the Twelth International Congress of Applied Mechanics, Stanford University, 1968, pp.246-256.
[14] Koroleva, E., "Stability of cylindrical shells of oval cross-section in the bending stress-state", Prikladnaya Matematika i Mekhanika, 1974, 37(5), pp.901-904.
[15] Kempner, J. and Chen, Y.N., "Buckling and initial postbuckling of oval cylindrical shells under combined axial compression and bending", Transactions of the New York Academy of Sciences, 1974, 36(2), pp.171-191.
[16] Chen, Y.N. and Kempner, J., "Buckling of oval cylindrical shells under compression and asymmetric bending", AIAA Journal, 1976, 14(9), pp.1235-1240.
[17] Tvergaard, V., "Buckling of elastic-plastic oval cylindrical shells under axial compression" International Journal of Solids and Structures, 1976, 12(9-10), pp.683-691.
[18] Tang, S.C., Chu, C.C. and Yeung, K.S., "Collapse of long, noncircular, cylindrical shells under pure bending", Computers and Structures, 1985, 21(6), pp.1345-1353.
[19] EN 10002-1, "Metallic materials – Tensile testing – Part 1: Method of test at ambient temperature", CEN, 2001.
[20] Gardner, L. and Ministro, A., "Testing and numerical modelling of structural steel oval hollow sections", Research Report No. 04-002-ST, Department of Civil and Environmental Engineering, Imperial College London, 2004.
[21] Schafer, B. and Peköz, T., "Computational modelling of cold-formed steel: characterizing geometric imperfections and residual imperfections", Journal of Constructional Steel Research, 1998, 47(3), pp.193-210.
[22] Gardner, L. and Nethercot, D.A., "Experiments on stainless steel hollow sections - Part 1: Material and cross-sectional behaviour", Journal of Constructional Steel Research, 2004, 60(9), pp.1291-1318.
[23] Eckhardt, C., "Classification of oval hollow sections", School of Civil Engineering Report, University of Southampton, 2004.
[24] ABAQUS, "ABAQUS/ Standard User's Manual Volumes I-III and ABAQUS CAE Manual", Version 6.4, Hibbitt, Karlsson & Sorensen, Inc. Pawtucket, USA, 2003.
[25] prEN 1993-1-1, "Eurocode 3: Design of steel structures – Part 1.1: General rules and rules for buildings", CEN, 2003.
[26] Gardner, L. and Nethercot, D.A., "Designers' Guide to EN 1993-1-1: Eurocode 3: Design of Steel Structures", Thomas Telford Publishing, London, 2005.

THE EFFECTS OF ELASTO-PLASTIC BEHAVIOR AT THE CRACK TIP ON FATIGUE CRACK PROPAGATION

Y. Xiong[1] J. Katsuta[2,*] K. Kawano[2] T. Sakiyama[2]

[1]*Graduate School of Science and Technology, Nagasaki University,*
1-14 Bunkyo-machi, Nagasaki, 852-8521, Japan

[2]*Department of Structural Engineering, Faculty of Engineering, Nagasaki University,*
1-14 Bunkyo-machi, Nagasaki, 852-8521, Japan

*(*Corresponding author: katsuta@st.nagasaki-u.ac.jp)*

Abstract: Emphasis on physical meanings of the hysteresis loop denoting the relationship between loads and strains near the crack tip, variations of the loading tensile plastic load zone and the unloading compressive plastic load zone are studied respectively under various fatigue test conditions, and the effects on acceleration, deceleration and non-propagation during fatigue crack propagation are also studied. Two types of crack closure are obtained from tests, and the influence of each load zone of the hysteresis loop on fatigue crack propagation is evaluated. Result shows that load zones P_{RPG}~P_{max} and P_{RCPG}~P_{CF} play an important role in the crack opening/closure behavior, and the fatigue crack propagates difficultly if the compressive plastic zone at the crack tip is not enough.

Keywords: Fatigue crack propagation, Crack tip, Opening/closure, Hysteresis loop, compressive plastic zone, Variable amplitude loading.

1. INTRODUCTION

The effect of elasto-plastic behavior at the crack tip on fatigue crack propagation has been known since Elber [1] affirmed crack closure phenomenon during fatigue crack propagation by experiment. An effective stress intensity factor range ΔK_{eff} ($=K_{\max}-K_{\mathrm{op}}$) was defined by an opening stress intensity factor K_{op}, and the opening load P_{op} was often measured by ASTM 2% offset method or curve fitting method [2], as well as an unloading elastic compliance method brought by Kikukawa *et al*. [3]. Otherwise, Nisitani and Chen [4] defined an effective stress intensity factor range ΔK_{eff} ($=K_{\max}-K_{\mathrm{cl}}$) by means of a closure stress intensity factor K_{cl}, and the closure load P_{cl} was determined based on the inflexion point on the unloading compliance. But, loads P_{op} and P_{cl} were dependent on geometric criterion of the compliance curve obtained by global measurement techniques, and the method neglects the physical meaning of compliance change caused by plastic deformation at the crack tip. Recently, Toyosada and Niwa [5] investigated the physical change of the compliance during a load cycle by local measurement techniques, presented a concept of Re-tensile plastic zone's generated load P_{RPG} and established ΔK_{RPG} ($=K_{\max}-K_{\mathrm{RPG}}$). He also presented a method for determining the special loads such as opening/closure loads through overlapping the original hysteresis loop near the crack tip on the loop which rotates at the coordinate origin by 180°. However, the above parameters cannot evaluate the effect of the compressive plastic zone at the crack tip on fatigue crack propagation, and there was an inaccuracy caused by the manual operation after experiment.

In this paper, by using global measurement techniques, the hysteresis loop of strains via loads denoting elasto-plastic behavior near the crack tip is obtained. Loads at inflexions on the hysteresis loop are calculated by differential and the hysteresis loop is divided into several physical load zones. Fatigue tests of CT specimen are carried out under variable amplitude loading. Emphasis on variations of the loading tensile and the unloading compressive plastic load zones during fatigue crack propagation, how the variations affect acceleration, deceleration and non-propagation

phenomena are investigated in detail. By using of parameter P_{CF} that is presented in paper, the effect of the compressive plastic zone at the crack tip on fatigue crack propagation is ascertained.

2. EXPERIMENTAL DETAILS

2.1. Material and conditions in fatigue test

The fatigue test machine is a digital, hydraulic servo control machine with 200kN load capacity. Using a high-precision load cell and a digital dynamic strain meter as well as self-made measurement program, and strains both near the crack tip and on the back face and loads can be measured simultaneously with a sampling time 1msec. The test process is monitored by a computer.

A CT specimen made of mild steel (JI-SM400B) is shown in Figure 1. The chemical composition and mechanical properties of the material are given in Table 1. Several groups of 5-piece (GL2mm) strain gages are glued on surfaces of specimen just along the direction of crack propagation, a cut-free strain gage nearest to the crack tip is always chosen automatically by the program, and the strain near the crack tip is measured. Under a sine tensile load with a frequency 10Hz, constant amplitude loading, block amplitude loading and K_{th} tests are carried out. In constant amplitude loading tests, the maximum load is 20kN and the minimum load is 2kN. In block amplitude loading tests, the minimum load is always 2kN and the maximum load changes at intervals of 50000 cycles. The load amplitudes from stage A to stage F are 2-20kN, 2-30kN, 2-20kN, 2-10kN, 2-20kN, 2-30kN, respectively. In K_{th} tests, the maximum load is always 20kN and the minimum load rises at intervals of 2.5mm crack propagation length. The load amplitude at stage A is 2-20kN. The increment is 2kN from B to E, 1kN from F to K, 0.5kN from L to O, respectively. Finally, the load amplitude is about 18-20kN at O.

Table 1. Chemical composition and mechanical properties of SM400B

Chemical compositions (wt. %)					Mechanical properties (MPa , %)		
C	Si	Mn	P	S	Yield stress	Tensile strength	Elongation
0.15	0.21	0.61	0.02	0.012	314	440	26

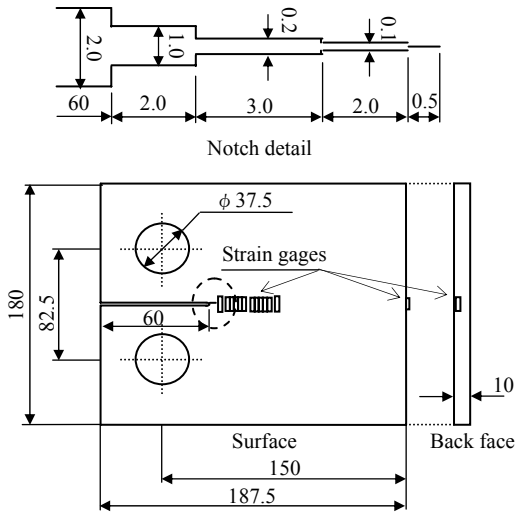

Figure 1. CT type specimen used in fatigue test

2.2. Measurement of fatigue crack length

The relationship between the compliance and the fatigue crack length is determined by other experiments. The compliance is obtained from the relationship between loads and strains on the back surface of CT specimen (Figure 2). The fatigue crack length is measured by beach mark method. Their relation is given by a curve in Figure 3. The crack propagation length in fatigue test is calculated from equation (1) based on Figure 3 [6].

$$C_p = \frac{1}{Et}\times\left\{1+\frac{0.25}{a_i/W}\right\}\times\left\{\frac{1+a_i/W}{(1-a_i/W)^2}\right\}\times\left\{0.0901+1.2787\frac{a_i}{W}+0.1854\left(\frac{a_i}{W}\right)^2-1.6939\left(\frac{a_i}{W}\right)^3+0.8617\left(\frac{a_i}{W}\right)^4+0.983\left(\frac{a_i}{W}\right)^5\right\} \quad (1)$$

where C_p is the compliance, E Young's Modulus, t and W the thickness and the width of CT specimen (mm), a_i the crack length (mm).

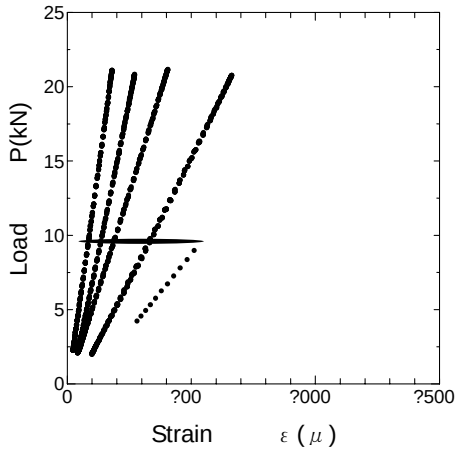

Figure 2. The example of relation between loads and strains on the back-face

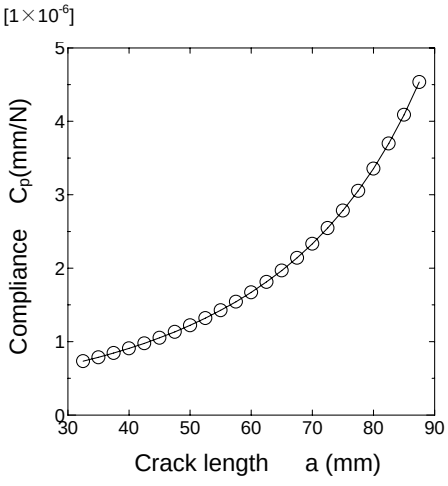

Figure 3. Relationship between compliance and fatigue crack length

2.3. Measurement of physical load zones on hysteresis loop

The relationship between loads and strains near the crack tip under given cycles is monitored by program. Figure 4 provides a series of results measured step by step during fatigue crack propagation. For each result, subtracting the unloading elastic strains from strains near the crack tip and magnifying them, a hysteresis loop is obtained as shown in Figure 5 (middle). But it is difficult to determine loads at physical inflexions from the original hysteresis loop. In order to evaluate the elasto-plastic behavior at the crack tip quantitatively, the hysteresis loop is divided into loading and unloading parts and the least square method is applied for expression by functions as shown in Figure 5(left and right). Figure 6 gives the relationships between P and $d\varepsilon'/dp$, and between P and $d^2\varepsilon'/dp^2$.

Based on physical study in the Ref. [7], the maximum in the first differential of unloading part is defined as the closure load P_{cl}, and the minimum in the second differential of loading part is defined as Re-tensile plastic zone's generated load P_{RPG}. The reason for the former is that regeneration of Re-compressive plastic zone at the crack tip leads $d\varepsilon'/dp$ raise and the increase in ligament after crack closure makes $d^2\varepsilon'/dp^2$ decrease during unloading process. The reason for the latter is that $d\varepsilon'/dp$ increases and $d^2\varepsilon'/dp^2$ decreases before crack open, but $d\varepsilon'/dp$ and $d^2\varepsilon'/dp^2$ increase simultaneously with Re-tensile plastic zone generates during loading process.

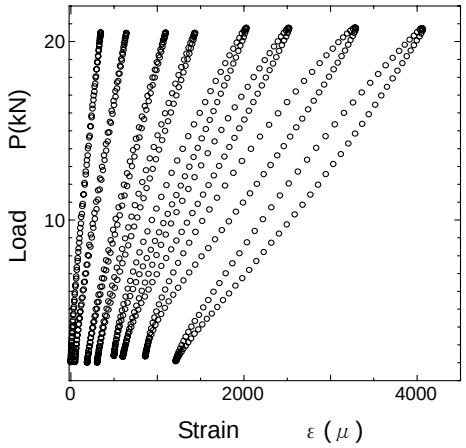

Figure 4. The examples of relation between loads and strains near the fatigue crack tip

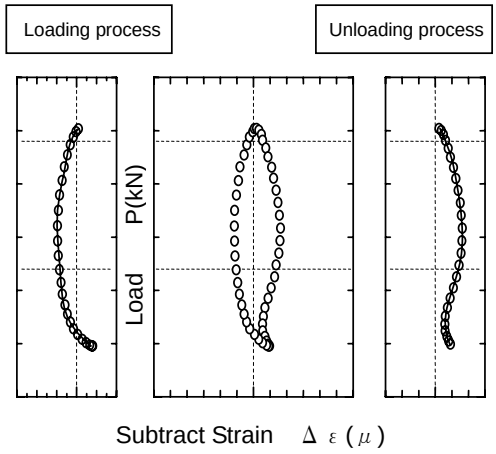

Figure 5. An example of separated hysteresis loop to make functions

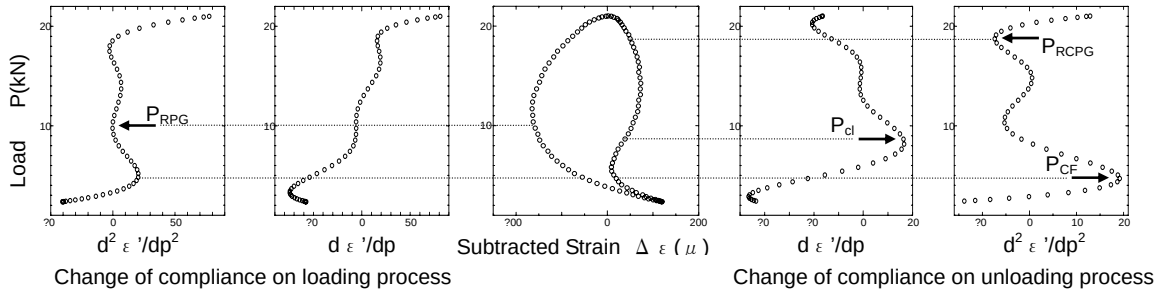

Figure 6. Quantitative calculation of P_{RCPG} P_{RPG} P_{cl} and P_{CF}

In addition, the minimum in the second differential of unloading part is defined as Re-compressive plastic zone's generated load P_{RCPG}. But there is extreme point within zone P_{cl}~P_{min} if the differential of compliance is carried out. The growth rate of the Re-compressive plastic zone from P_{cl} to the extreme point is slower than that in zone P_{RCPG}~P_{cl}, and the growth of crack closure is dominant, so $d\varepsilon'/dp$ decreases and $d^2\varepsilon'/dp^2$ increases. As unloading to the extreme point, that crack close will not progress due to the crack surfaces contact, therefore, $d\varepsilon'/dp$ and $d^2\varepsilon'/dp^2$ decrease simultaneously. Hereby, the extreme point is defined as a crack closure finish load P_{CF} in this paper. Consequently, the zone from P_{RPG} to P_{max} (ΔP_{PRG}) indicates the loading tensile plastic load zone, the zone from P_{max} to P_{RCPG} the unloading elastic load zone, the zone from P_{RCPG} to P_{CF} (ΔP_{RCF}) the unloading compressive plastic zone, and the zone from P_{CF} to P_{min} the hysteresis loop tail.

3. TEST RESULTS AND ANALYSIS

3.1. In the case of constant amplitude loading

Figure 7 shows a part of test results under constant amplitude loading. Because of 0.1mm width pre-crack on the bottom of saw notch, a small load causes yielding at the crack tip in the initial stage of fatigue crack propagation. At this time, the value P_{RCPG} is in the high load region, but the values P_{RPG}, P_{cl} and P_{CF} are in the low load region as shown in Figure 7(b), and the hysteresis loop tail is not formed as shown in Figure 7(a)(1). When the value P_{RPG}, P_{cl} and P_{CF} rise gradually, the hysteresis loop tail enlarges gradually as shown in Figure 7(a)(2) and (3), and the fatigue crack begins to propagate. When each of the value P_{RCPG}, P_{RPG}, P_{cl}, and P_{CF} tends to constants, the

hysteresis loop tail are obvious as shown in Figure 7(a)(4),(5) and (6), and the fatigue crack propagates stably. Thereafter, the value P_{RPG}, P_{cl}, and P_{CF} decrease, the crack difficult to close as shown in Figure 7(a)(7) and (8), and the fatigue crack propagates fast. Therefore, it is considered that the change in size of the hysteresis loop tail is due to the influence of tensile deformed layer that remains on the crack surface as the fatigue crack propagates, which was described by Elber [1].

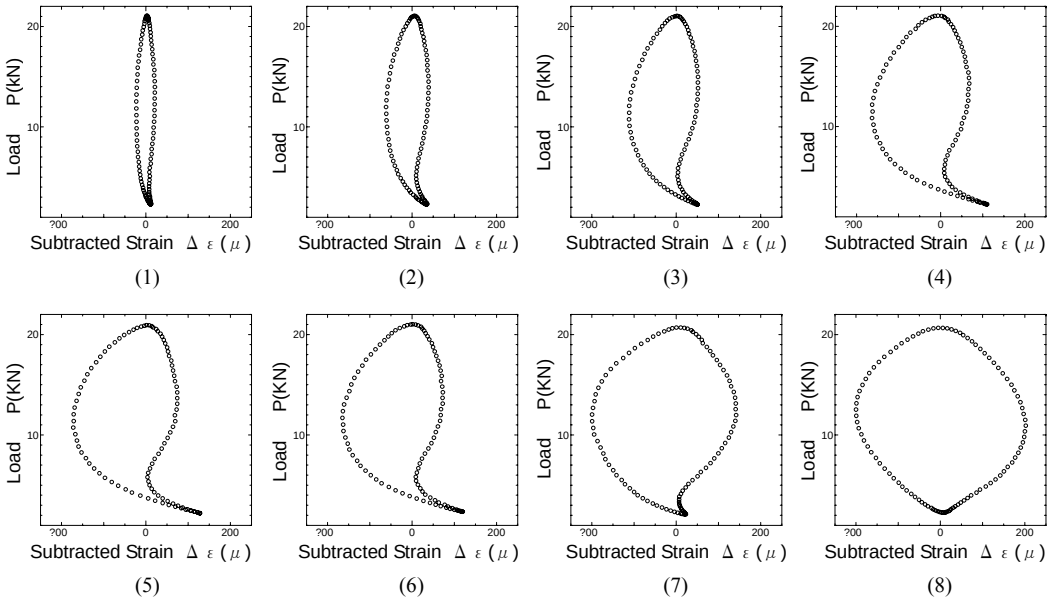

(a) Change of hystersis loops during fatigue crack propagation

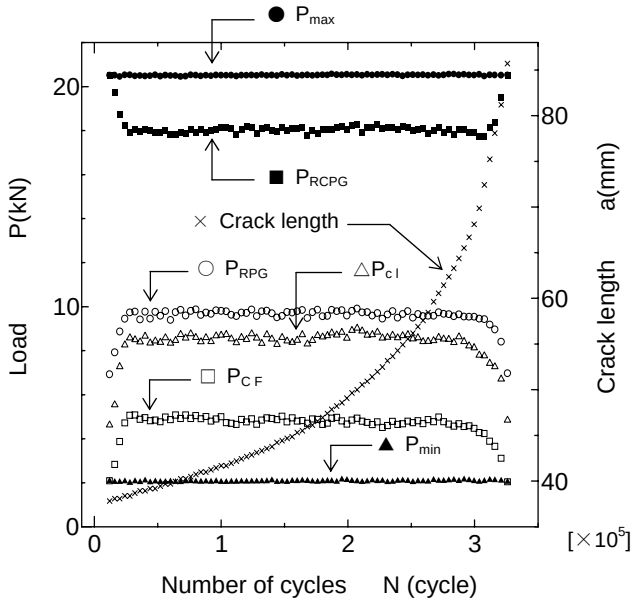

(b) The relationship between loads and fatigue crack length

Figure 7. Results of constant amplitude loading test

3.2. In the case of block amplitude loading

Figure 8 is a part of test results under block amplitude loading. Figure 8(a)(1)(3)(4)(5)(6)(7) indicate the characteristics of the hysteresis loops in each stage when the crack grows stably. Because the test condition in the stage A is the same as that under constant amplitude loading, the test results are the same. Entering stage B, in the early stage of the maximum load P_{max} rising to 30kN, P_{RPG}, P_{cl} and P_{CF} decrease temporarily, the hysteresis loop tail becomes small as shown in

Figure 8(a)(2), and the crack propagation shows acceleration. Because of a large tensile deformed zone forms at the crack tip when the overload is applied, the crack tip opens fully. After that, the tensile deformed layer on the crack surface becomes thick gradually with the crack propagation under high amplitude loads, thus make the crack close easy. Therefore, the value P_{RPG}, P_{cl} and P_{CF} rise to constants in this stage. But in the stages C and E, the zone from P_{RCPG} to P_{cl} reduces, the hysteresis loop tail lengthens as shown in Figure 8(a)(4) and (6). It is considered due to the effect of the thick residual tensile deformed layer that remains on the crack surface in the stage B make the crack close easy, thus the crack propagation shows deceleration. Entering the stage D, the value P_{max} is close to the value P_{RPG} in the stage C, and the value for the zone from P_{RCPG} to P_{cl} is almost zero, which means there is only elastic deformation at the crack tip under low amplitude loads as shown in Figure 8(a)(5), thus the crack propagation shows non-propagation. In the stage F, the zones ΔP_{RPG} and ΔP_{RCF} increase with the maximum load P_{max} increasing again and the hysteresis loop tail becomes small as shown in Figure 8(a)(8), thus the fatigue crack propagates speedily again.

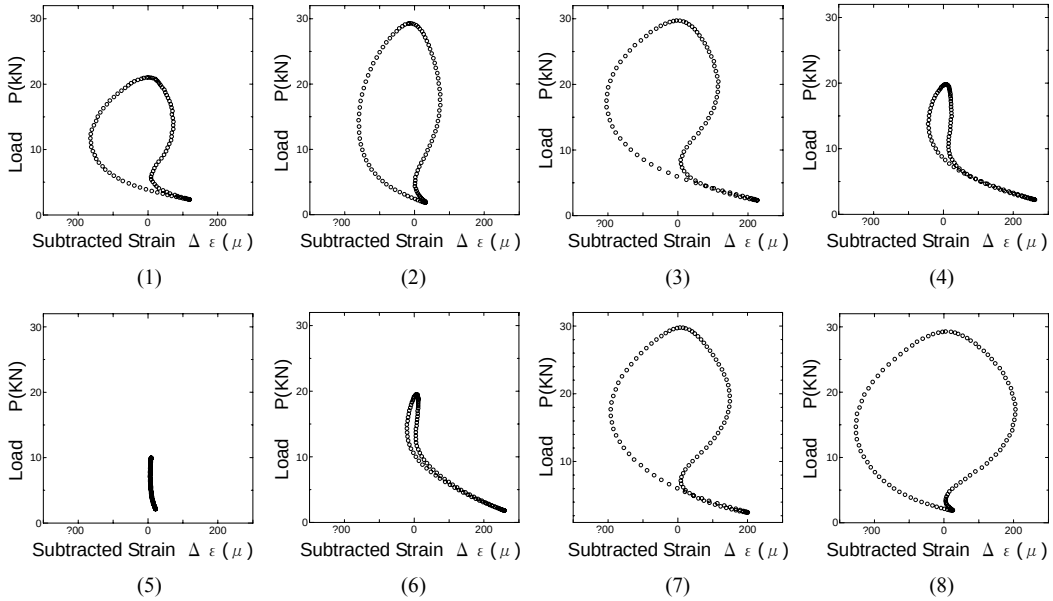

(a) Change of hystersis loops during fatigue crack propagation

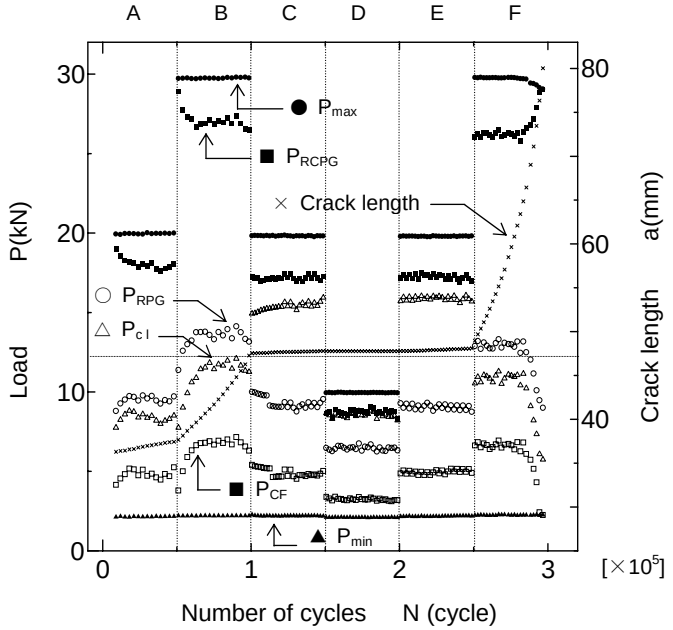

(b) The relationship between loads and fatigue crack length

Figure 8. Results of block amplitude loading test

In addition, there is a formula for CT specimen according to fracture mechanics,

$$K = \frac{P}{t\sqrt{W}} f\left(\frac{a}{W}\right) \tag{2}$$

calculating the stress intensity factors by the loads in Figure 8b a linear relationship is obtained,

$$\left(K_{\max} - K_{RPG}\right)/\left(K_{RCPG} - K_{CF}\right) = \alpha \tag{3a}$$

and then the following equation is achieved,

$$\Delta K_{RPG} = \alpha \Delta K_{RCF} \tag{3b}$$

It indicates that ΔK_{RPG} decreases with ΔK_{RCF} decreasing, or the crack propagates difficultly.

It is observed from the experiments, due to the increase of load amplitude, the residual tensile plastic deformed layer on the crack surface becomes thick, the crack surfaces contact completely when the load is unloaded to P_{CF}. Consequently, P_{CF} plays an action of shielding the crack tip. It have been clarified that the shielding action increases with the crack closure increasing.

3.3. In the case of K_{th} test

Figure 9(a) shows hysteresis loops of some stage in the K_{th} test. From the figure it is observed once the hysteresis loop becomes small, the hysteresis loop tail disappears gradually. It is known from Figure 9(b) they are different from those under block amplitude loading (decreasing maximum load), the value P_{RPG} rises gradually and approaches $P_{\max}$, but the value P_{cl} approaches $P_{\min}$, and the fatigue crack propagation rate reduces from deceleration to non-propagation. This is because the thickness of the residual tensile deformed layer is almost the same at each stage of fatigue crack propagation in the case of the constant $P_{\max}$. Therefore, the crack propagation decelerates when the hysteresis loop tail disappearing, with the minimum load $P_{\min}$ increasing gradually. It means the shielding action of P_{CF} decrease to the minimum, or the value P_{CF} coincides with $P_{\min}$. But, when the minimum load rises to the preceding unloading elastic load zone, the crack opening is small in the subsequent loading process. Therefore the hysteresis loop shows no evident of opening at the crack non-propagation stage. The above characteristic is the same as that under block amplitude loading. It is known the fatigue crack propagates difficultly if there is not sufficiently compressive plastic zone at the crack tip.

4. DISCUSSION

Based on the test results, there are two types of crack closure that are closure-free and closure-affected respectively, and the open/closure patterns of the crack tip in different load zones of the hysteresis loop given in Figure10. Figure 10(a) and (b) denote an example of fatigue crack deceleration stage under K_{th} tests and block amplitude loading, respectively.

After loading from $P_{\min}$, to the former, the crack tip opens gradually and it opens completely when the load reaches P_{op}. To the latter, closed crack surface opens gradually as the load reaches P_{CF}, and the crack tip opens completely when the load reaches P_{op}. Once the load exceeds the load point P_{RPG}, the residual compressive stress acted at the crack tip releases completely and the Re-tensile plastic zone begins to form (If unloading begins before P_{RPG}, the crack tip is in elastic status which is the same as the stage D under block amplitude loading). As the load continues to increase and reaches $P_{\max}$, the tensile plastic deformation at the crack tip reaches the maximum, and the crack propagates during this process. In the following unloading process, through the unloading elastic

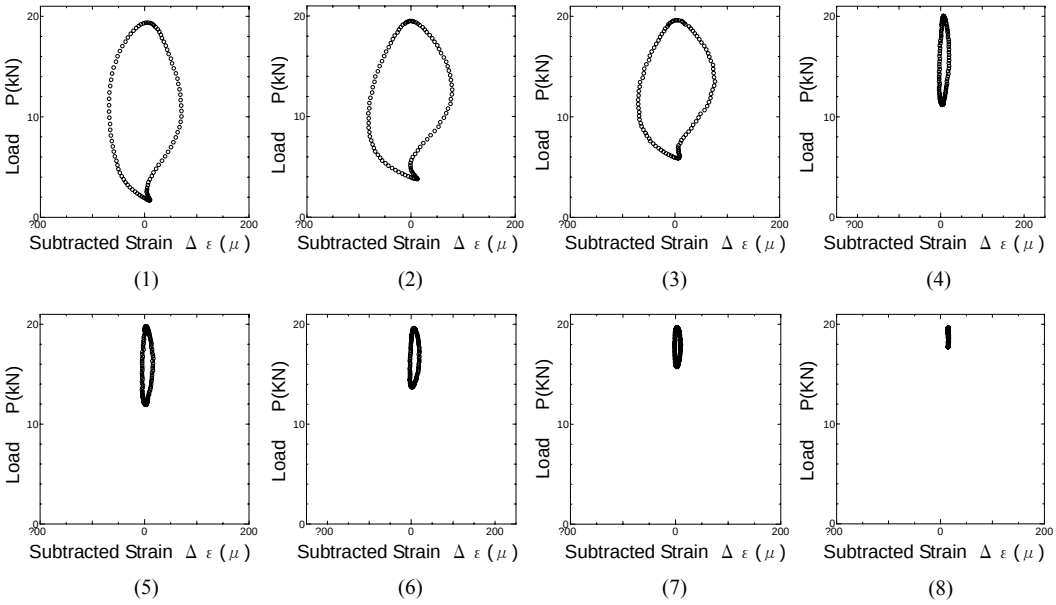

(a) Change of hystersis loops during fatigue crack propagation

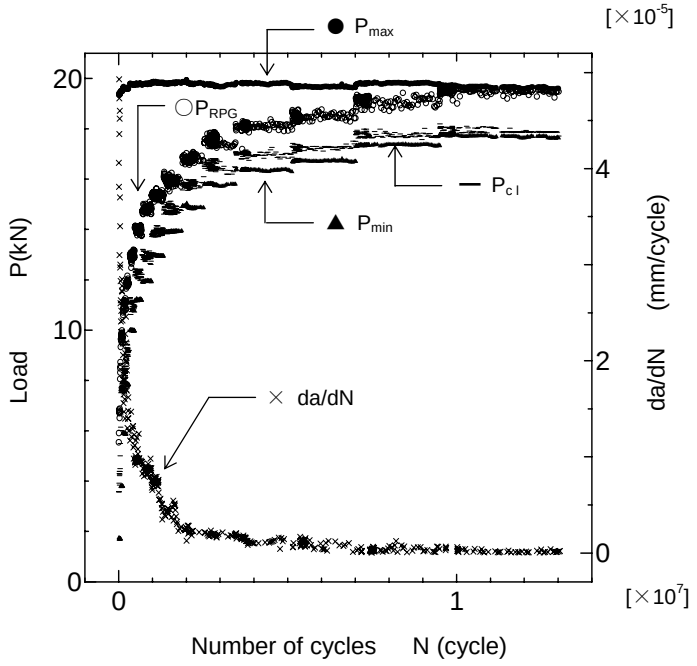

(b) The relationship between loads and fatigue crack propagation data

Figure 9. Results of K_{th} test

zone P_{max}~P_{RCPG} (If loading before P_{RCPG}, the crack tip is in elastic status which is the same as the final stage in K_{th} test), the Re-compressive plastic zone at the crack tip begins to form and the crack tip begins to close as the unloading reaches P_{cl}. After that, to the former, the crack tip close completely when the load is unloaded to P_{min}, and the actual amplitude at the crack tip is equivalent to applied amplitude $\Delta K(=K_{max}-K_{min})$. To the latter, the crack surfaces contact when the load is unloaded to P_{CF}, which likes the crack mouth being fully wedged-frozen, and the actual stress intensity factor at the crack tip is still K_{CF} even though the load is unloaded to P_{min}. So the actual amplitude at the crack tip decreases from $\Delta K(=K_{max}-K_{min})$ to $\Delta K_{CF}(=K_{max}-K_{CF})$, it likes the change in load condition.

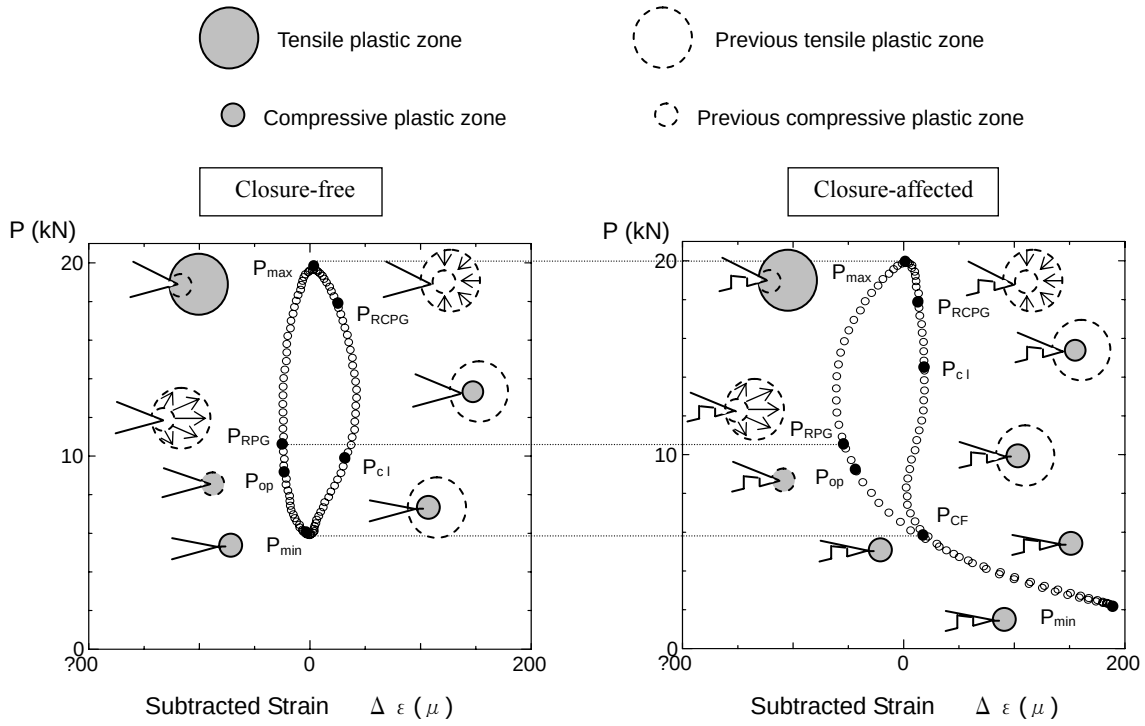

(a) An example of deceleration in the case of K_{th} test (b) An example of deceleration in the case of block amplitude loading

Figure 10. Schematic diagram the influence of crack closure on fatigue crack propagation

According to the relationship between the size of the plastic zone at the crack tip and the square of K in the Ref. [8], if K_{max} denotes the size of the tensile plastic zone and ΔK_{RCF} ($=K_{RCPG}-K_{CF}$) denotes the size of the compressive plastic zone indirectly, then ΔK_{RPG} ($=K_{max}-K_{RPG}$) represents the overlapped zone of tensile and compressive zones. The plastic deformation energy in this overlapped zone drives a fatigue crack to propagate only [9]. The above tests shows the fatigue crack grows difficultly if there is no completely compressive plastic zone ΔK_{RCF}, and ΔK_{RPG} is not enough yet. Therefore, the reason of fatigue crack deceleration is that the reduction in the actual amplitude causes a decrease in the compressive plastic zone at the crack tip.

5. CONCLUSION

Emphasis on the hystersis loop denoting the relationship between loads and strains near the fatigue crack tip, the elasto-plastic behavior at the crack tip is studied under various fatigue test conditions, and the results are as follows.

(1) An alternating change in the tensile and the compressive plastic zones is a requirement for fatigue crack propagation. The crack propagation decelerates in the absence of a sufficient compressive plastic zone at the crack tip.

(2) The route of fatigue crack propagation P_{RPG}~P_{max} and P_{RCPG}~P_{CF} plays an important effect in the crack opening/closure behavior, and is also a fundamental reason for causing the acceleration, deceleration and non-propagation phenomena under variable amplitude loading.

(3) The crack closure types and the size of the plastic zone at the crack tip can be speculated according to the loads such as open/closure load on the hysteresis loop obtained by differential, and the fatigue crack propagation behavior can also be estimated quantitatively.

NOTATION

K_{max}, P_{max} = maximum stress intensity factor, maximum load
K_{min}, P_{min} = minimum stress intensity factor, minimum load
K_{cl}, P_{cl} = closure stress intensity factor, closure load
K_{op}, P_{op} = opening stress intensity factor, opening load
K_{RPG}, P_{RPG} = stress intensity factor at RPG load, Re-tensile plastic zone's generated load
K_{RCPG}, P_{RCPG} = stress intensity factor at RCPG load, Re-compressive plastic zone's generated load
K_{CF}, P_{CF} = stress intensity factor corresponding to P_{CF}, crack closure finish load
K_{th} = threshold stress intensity factor
ΔK_{RPG}, ΔP_{RPG} = stress intensity factor range at ΔP_{RPG} ($=P_{max}-P_{RPG}$), tensile plastic loading zone
ΔK_{RCF}, ΔP_{RCF} = stress intensity factor range corresponding to ΔP_{RCF} ($=P_{RCPG}-P_{CF}$), compressive plastic loading zone
ΔK_{CF} = stress intensity factor range corresponding to ΔP_{CF} ($=P_{max}-P_{CF}$)

REFFERENCES

[1] Elber, W., "The significance of fatigue crack closure", In: Damage tolerance in aircraft structures, ASTM STP 486, 1971, pp.230-242.
[2] Stoychev, S. and Kujawki, D., "Methods for crack opening load and crack tip shielding determination: a review", Fatigue Fract. Engng Maert. Struct., 2003, 26, pp.1053-1067.
[3] Kikukawa, M., Jono, M., Tanaka, K. and Takatani, M., "Measurement of fatigue crack propagation and crack closure at low stress intensity level by unloading elastic compliance method", J. Soc. Mater. Sci. Jpn., 1976, 25, pp.899-903.
[4] Nisitani, H. and Chen, D.H.A., "Consideration on the Unloading Elastic Compliance Method", Trans. Jpn. Soc. Mech. Eng,. 1985, 51, pp.1436-1441.
[5] Toyosada, M. and Niwa, T., "The significance of RPG load for fatigue crack propagation and the development of a compliance measuring system", Int J. Fracture., 1994, 67, pp.217-230.
[6] Machida, S., Yoshinari, H. and Makino, H., "Detailed observation of change in strain near fatigue crack tip", J. Soc. Mater. Sci. Jpn., 1997, 46, pp.138-142.
[7] Katsuta, J., Tetsukawa, S., Kawano, K. and Hidaka, T., "On the Measurement for propagation behavior of fatigue crack using piezoelectric ceramics", The West-Japan Society of Naval Architect, 2000, 100, pp.313-325.
[8] Toyosada, M., "A study of threshold phenomena by residual tensile layer close to the surface of a fatigue crack", The West-Japan Society of Naval Architect, 2002, 105, pp.223-235.
[9] Dugdale, D.S., "Yielding of steel sheets containing slits", J. Mech. Phys. Solids., 1960, 8, pp.100-108.

PRACTICAL ADVANCED ANALYSIS FOR STEEL FRAMES

A. Agüero and F. Pallares

Universidad Politecnica de Valencia, Campus Vera s/n, 46020 Valencia, España

Email: anagra@mes.upv.es

Abstract: The aim of this paper is to present a practical advanced analysis method for steel frame design, based on a simplified second-order elastic analysis of the structure with an equivalent geometric imperfection. The second order effects are calculated using the orthogonality properties of the buckling modes. The geometric imperfection is obtained from the buckling mode by a suitable scaling procedure using a generalization of Dutheil´s method.

Keywords: Advanced analysis, Geometric nonlinearity, Steel design, Steel frames, Geometric imperfection.

1. INTRODUCTION

The buckling analysis and design of steel frames requires to take into account: geometric and material nonlinearities. The geometric nonlinearity includes second-order effects associated with P-δ and P-Δ effects and geometric imperfections. The material nonlinearity includes gradual yielding associated with the influence of residual stresses and flexure (Figure 1).

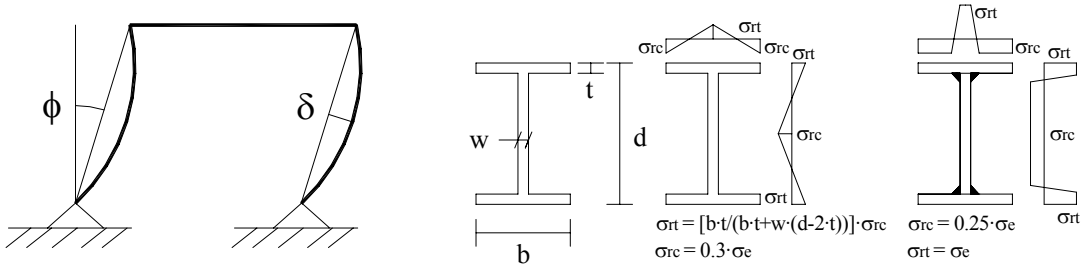

Figure 1. member imperfection (δ), frame imperfection (Φ) and residual stress diagrams

To obtain the collapse load of the structure some of these factors can be taken into account in a simplified way, for example by means of equivalent imperfections. In the present proposal a geometric equivalent imperfection is used to consider the residual stress, the geometric imperfection and the nonlinear constitutive behavior.

As shown in Figure 2, the Eurocode-3 [1] proposes a second order analysis of imperfect structures with two type of imperfections, member {δ} and frame {Φ}, the local imperfection can sometimes be neglected in the global analysis and considered by means of the proper design formula with an auxiliary coefficient "χ".

The method presented in this paper is based on:

1. A linear analysis of the structure used to obtain the primary internal forces and moments.
2. An initial stability analysis used to obtain the secondary internal forces and moments.
3. The analysis is limited to the elastic range and the computed collapse load is equal to the one causing the formation of the first plastic hinge or yield, depending on the use of the plastic (Class 2) or elastic (Class 3) section modulus.
   The formation of the first plastic hinge can be expressed as Chen [2]:

$$\left(\frac{M_Z^{KB}}{M_{zpl}^{KB}}\right)^{\alpha} + \left(\frac{M_Y^{KB}}{M_{ypl}^{KB}}\right)^{\beta} \leq 1$$

Or in a conservative way as:

$$\frac{N_{KB}}{N_{pl}^{KB}} + \frac{M_Z^{KB}}{M_{zpl}^{KB}} + \frac{M_Y^{KB}}{M_{ypl}^{KB}} + \frac{Bi^{KB}}{Bi_{pl}^{KB}} = 1$$

4. The orthogonality properties of the buckling modes are used to simplify the analysis.
5. A generalization of Dutheil's method is used to obtain the geometric equivalent imperfection.

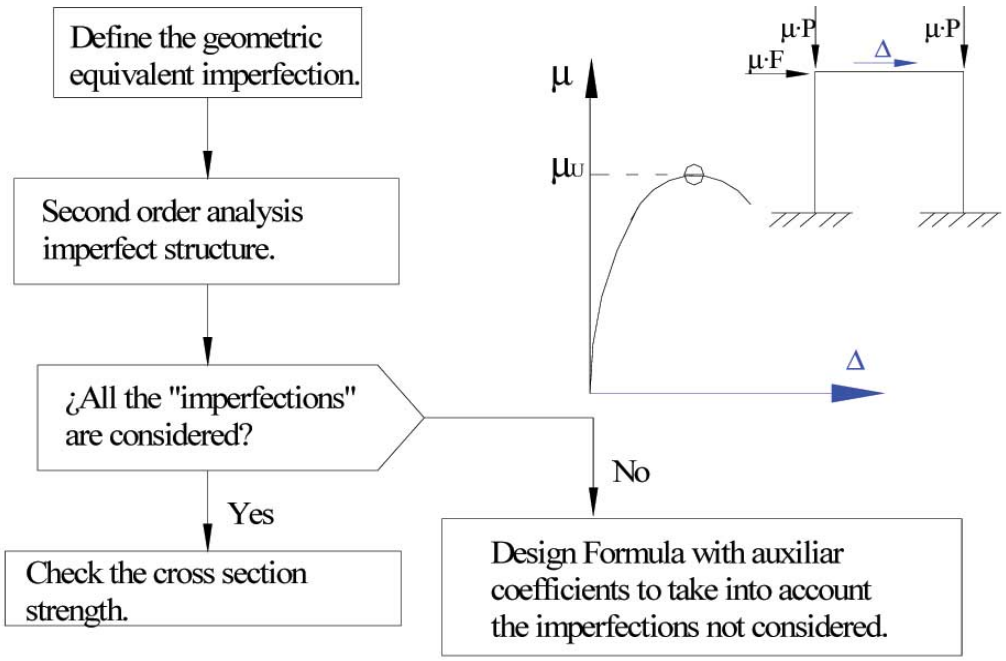

Figure 2. Frame analysis according to Eurocode

The proposed method can be applied easily to the design of practical structures due to its compatibility with the design code requirements and its simplicity, and like the practical advanced analysis methods proposed by Chan [3] and Kim [4] it does not require tedious separate member capacity checks so it can find its way into practice.

2. DESCRIPTION OF THE PROPOSED METHOD

In first place the nonlinear geometric analysis of imperfect structures is described, giving a simplified way of analysis, using the orthogonality properties of the bucking modes. In second place a methodology is proposed to obtain the geometric equivalent imperfection.

Nonlinear analysis of the structure with geometric imperfections

The governing equilibrium equations of the imperfect prismatic beam column with primary constant axial {P} and constant strong bending moment {My}, and small distributed loads {p_x, p_y, p_z, m_x} are:

$$EA\frac{d^2u}{dx^2} = -p_x$$

$$EIy\frac{d^4w}{dx^4} + P\frac{d^2w}{dx^2} = -P\frac{d^2w_i}{dx^2} + p_z$$

$$EIz\frac{d^4v}{dx^4}+My\frac{d^2\theta_x}{dx^2}+P\frac{d^2v}{dx^2}=-My\frac{d^2\theta_{xi}}{dx^2}-P\frac{d^2v_i}{dx^2}+p_y$$

$$\left(-GIt+\mathrm{Pr}_o^{\,2}\right)\frac{d^2\theta_x}{dx^2}+My\frac{d^2v}{dx^2}+EIa\frac{d^4\theta_x}{dx^4}=-\mathrm{Pr}_o^{\,2}\frac{d^2\theta_{xi}}{dx^2}-My\frac{d^2v_i}{dx^2}+m_x$$

The displacements are given by:

$$u(x)=a_1+a_2x-\frac{p_x}{2EA}x^2$$

$$v(x)=a_3senh(\mu x)+a_4\cosh(\mu x)+a_5\cdot senh(\beta x)+a_6\cdot\cosh(\beta x)+a_7+a_8x$$
$$+\frac{Mym_x+p_y\left(GIt-Pr_o^{\,2}\right)}{2\left(P\left(GIt-Pr_o^{\,2}\right)+My^2\right)}x^2+v_{ia}(x)$$

$$w(x)=a_9+a_{10}x+a_{11}\cos(kx)+a_{12}sen(kx)+\frac{p_z}{2P}x^2+w_{ia}(x);\ k=\sqrt{\frac{P}{EIy}}$$

$$\theta_x(x)=\eta(a_3senh(\mu x)+a_4\cosh(\mu x))+\psi(a_5senh(\beta x)+a_6\cosh(\beta x))+a_{13}+a_{14}x$$
$$+\frac{Myp_y-m_xP}{2\left(P\left(GIt-Pr_o^{\,2}\right)+My^2\right)}x^2+\theta_{xia}(x)$$

$$\mu=\frac{\sqrt{\rho-P\left(Izr_o^{\,2}+Ia\right)+\sqrt{4IzIaMy^2+\rho^2+2P\rho\left(Ia-Izro^2\right)+P^2\left(Izro^2\left(Izro^2-2Ia\right)+Ia^2\right)}}}{\sqrt{2EIzIa}}$$

$$\beta=\frac{\sqrt{\rho-P\left(Izr_o^{\,2}+Ia\right)-\sqrt{4IzIaMy^2+\rho^2+2P\rho\left(Ia-Izro^2\right)+P^2\left(Izro^2\left(Izro^2-2Ia\right)+Ia^2\right)}}}{\sqrt{2EIzIa}}$$

$$\eta=-\frac{EIz\mu^2+P}{My};\ \psi=-\frac{EIz\beta^2+P}{My}\ ;\ \rho=GIzIt$$

If the imperfection $\{v_i, w_i, \theta_{xi}\}$ is given by the first bucking mode the solution associated with the imperfection $\{v_{ia}, w_{ia}, \theta_{xia}\}$ is:

$$v_{ia}=\frac{v_i}{\mu_{1MN}-1};\ w_{ia}=\frac{w_i}{\mu_{1MN}-1};\ \theta_{xia}=\frac{\theta_{xi}}{\mu_{1MN}-1}$$

Several authors have studied the effect of imperfections on the behaviour of steel frames, Clarke *et al.* [5] showed that the worst shape was the one given by the first buckling mode. In case of Figure 3 this imperfection is for the frame D and for the cantilever E.

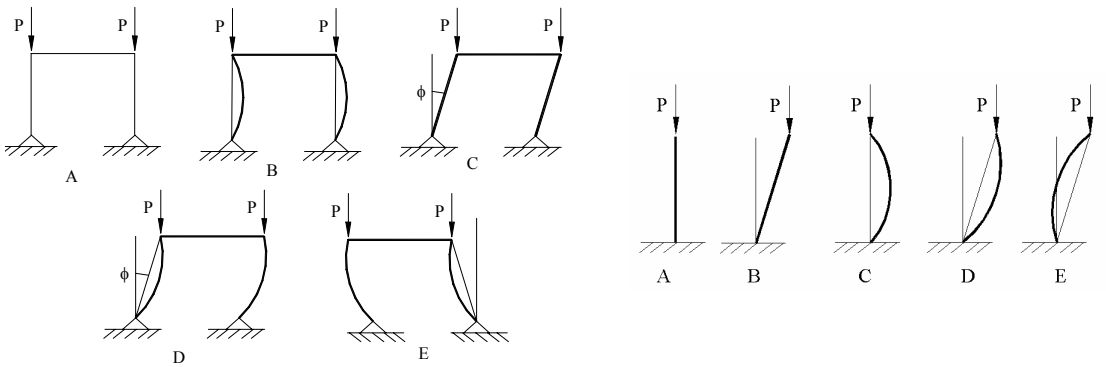

Figure 3. Different patterns of imperfection in a frame and a cantilever.

The consistent internal forces are:

$$N = EA\frac{du}{dx}$$

$$Qy = -EIz\frac{d^3v}{dx^3} - My\frac{d(\theta_x + \theta_{xi})}{dx} - P\frac{d(v + v_i)}{dx}$$

$$Qz = -EIy\frac{d^3w}{dx^3} - P\frac{d(w + w_i)}{dx}$$

$$Mx = -EIa\frac{d^3\theta_x}{dx^3} + GIt\frac{d\theta_x}{dx} - My\frac{d(v + v_i)}{dx} - \mathrm{Pr}_0^2\frac{d(\theta_x + \theta_{xi})}{dx}$$

$$My = -EIy\frac{d^2w}{dx^2}$$

$$Mz = EIz\frac{d^2v}{dx^2}$$

$$Bi = EIa\frac{d^2\theta_x}{dx^2}$$

The relationship between forces and displacements (Figure 4), stiffness matrix is given by:

Axial (The shortening due to bowing effects is neglected):

$$\begin{Bmatrix} f_{x1} \\ f_{x2} \end{Bmatrix} = \begin{bmatrix} \frac{EA}{L} & \frac{-EA}{L} \\ \frac{-EA}{L} & \frac{EA}{L} \end{bmatrix} \begin{Bmatrix} u_1 \\ u_2 \end{Bmatrix} + \begin{Bmatrix} f_{ex1} \\ f_{ex2} \end{Bmatrix}$$

Strong bending:

$$\begin{Bmatrix} f_{z1} \\ M_{y1} \\ f_{z2} \\ M_{y2} \end{Bmatrix} = \frac{k^2EIy}{2-2c-kLs} \begin{bmatrix} sk & c-1 & -sk & c-1 \\ c-1 & \frac{s-kLc}{k} & 1-c & \frac{kL-s}{k} \\ -sk & 1-c & sk & 1-c \\ c-1 & \frac{kL-s}{k} & 1-c & \frac{s-kLc}{k} \end{bmatrix} \begin{Bmatrix} w_1 \\ \theta_{y1} \\ w_2 \\ \theta_{y2} \end{Bmatrix} + \begin{Bmatrix} f_{ez1} \\ M_{ey1} \\ f_{ez2} \\ M_{ey2} \end{Bmatrix}$$

$$c = \cos(kL);\ s = sen(kL)$$

Weak bending coupled with torsion:

$$\begin{Bmatrix} f_{y1} \\ M_{x1} \\ M_{z1} \\ Bi_1 \\ f_{y2} \\ M_{x2} \\ M_{z2} \\ Bi_2 \end{Bmatrix} = [A][B]^{-1} \cdot \begin{Bmatrix} v_1 \\ \theta_{x1} \\ \theta_{z1} \\ \phi_1 \\ v_2 \\ \theta_{x2} \\ \theta_{z2} \\ \phi_2 \end{Bmatrix} + \begin{Bmatrix} f_{ey1} \\ M_{ex1} \\ M_{ez1} \\ Bi_{e1} \\ f_{ey2} \\ M_{ex2} \\ M_{ez2} \\ Bi_{e2} \end{Bmatrix}$$

$$[A]=\begin{bmatrix} 0 & 0 & 0 & 0 & 0 & P & 0 & My \\ 0 & 0 & 0 & 0 & 0 & My & 0 & -GIt + Pr_o^2 \\ 0 & -EIz\mu^2 & 0 & -EIz\beta^2 & 0 & 0 & 0 & 0 \\ 0 & -EIa\eta\mu^2 & 0 & -EIa\psi\beta^2 & 0 & 0 & 0 & 0 \\ 0 & 0 & 0 & 0 & 0 & -P & 0 & -My \\ 0 & 0 & 0 & 0 & 0 & -My & 0 & GIt - Pr_o^2 \\ EIz\mu^2 sh & EIz\mu^2 ch & EIz\beta^2 sha & EIz\beta^2 cha & 0 & 0 & 0 & 0 \\ EIa\eta\mu^2 sh & EIa\eta\mu^2 ch & EIa\psi\beta^2 sha & EIa\psi\beta^2 cha & 0 & 0 & 0 & 0 \end{bmatrix}$$

$$[B]=\begin{bmatrix} 0 & 1 & 0 & 1 & 1 & 0 & 0 & 0 \\ 0 & \eta & 0 & \psi & 0 & 0 & 1 & 0 \\ \mu & 0 & \beta & 0 & 0 & 1 & 0 & 0 \\ \mu\eta & 0 & \beta\psi & 0 & 0 & 0 & 0 & 1 \\ sh & ch & sha & cha & 1 & L & 0 & 0 \\ \eta sh & \eta ch & \psi sha & \psi cha & 0 & 0 & 1 & L \\ \mu ch & \mu sh & \beta cha & \beta sha & 0 & 1 & 0 & 0 \\ \mu\eta ch & \mu\eta sh & \beta\psi cha & \beta\psi sha & 0 & 0 & 0 & 1 \end{bmatrix}$$

$$ch=\cosh(\mu L);\ sh=senh(\mu L);\ cha=\cosh(\beta L);\ sha=senh(\beta L)$$

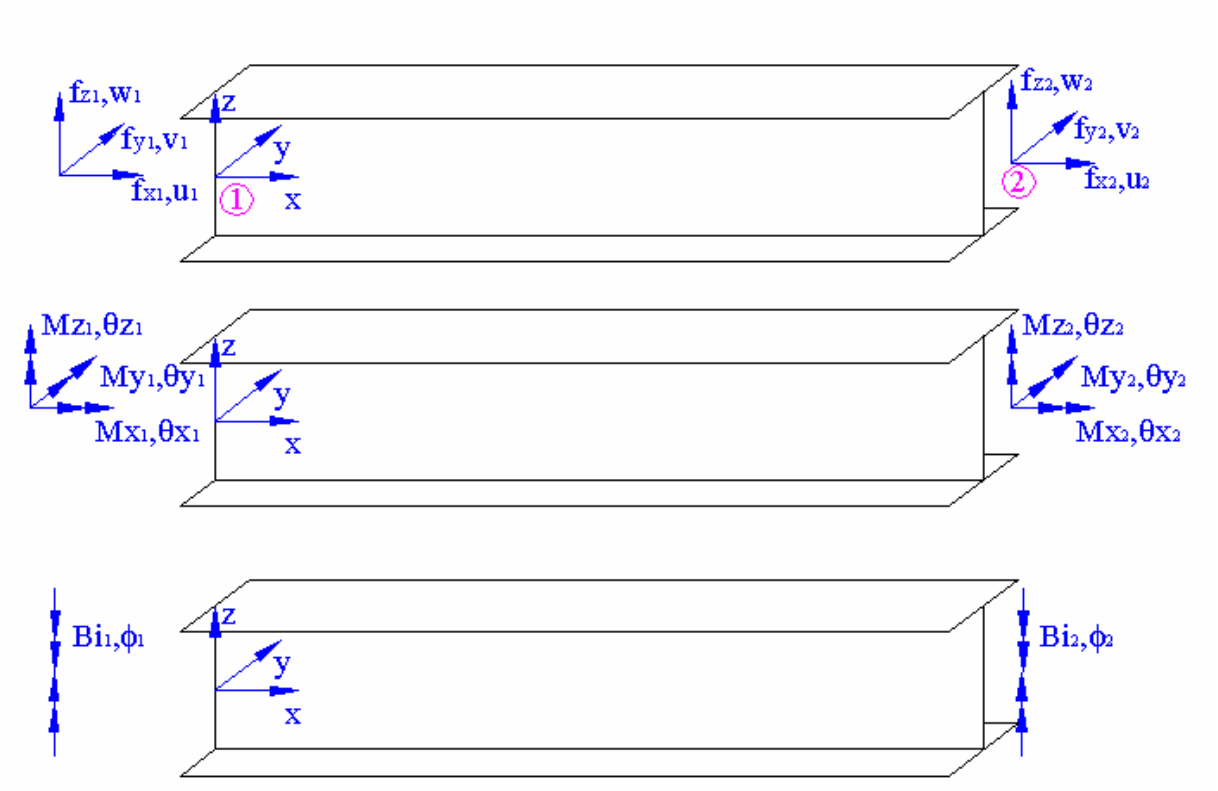

Figure 4. Forces and displacements

To apply the finite element method the first variation of the potential for a double symmetric section is used:

$$\delta V^e = \int \left(EAu'_p u' + EIyw''_p w'' + EIzw''_p v'' + GI_T \theta_{xp}{}' \theta_x{}' + EIa\theta_{xp}{}'' \theta_x{}'' \right) dx - f_{x1}u_{p1} - f_{y1}v_{p1} - f_{z1}w_{p1}$$
$$- f_{x2}u_{p2} - f_{y2}v_{p2} - f_{z2}w_{p2} - M_{x1}\theta_{xp1} - M_{y1}\theta_{yp1} - M_{z1}\theta_{zp1} - M_{x2}\theta_{xp2} - M_{y2}\theta_{yp2} - M_{z2}\theta_{zp2}$$
$$- Bi_1\phi_{p1} - Bi_2\phi_{p2} - \int_L \left(p_x u_p + p_y v_p + p_z w_p + m_x \theta_{xp} \right) dx - \int My \left[\left(v'+ v'_i \right) \theta_{xp}{}' + \left(\theta_x{}' + \theta_{xi}{}' \right) v'_p \right] dx$$
$$- \int P \left(\left(v'+ v'_i \right) v_p{}' + \left(w'+ w'_i \right) w_p{}' + ro^2 \left(\theta_x{}' + \theta_{xi}{}' \right) \theta_{xp}{}' \right) dx$$

The equilibrium equations of the structure will be:

$$\left([K_L] + [K_G] \right) \{ d_{NL} \} = \{ F_{ext} \} - [K_G] \{ d_{imp} \}$$

Simplified method to obtain the second order effects

The orthogonality properties of the buckling modes $\{\phi_{vi} ; \phi_{wi} ; \phi_{\theta xi}\}$ are for a general section, if $i \neq j$:

In a column, with primary axial forces {P}:

$$\int P \left(\phi'_{vi}\phi'_{vj} + \phi'_{wi}\phi'_{wj} + ro^2 \phi'_{\theta_x i}\phi'_{\theta_x j} + 2zc\phi'_{vi}\phi'_{\theta xj} - 2yc\phi'_{wi}\phi'_{\theta xj} \right) dx = \{ \phi_j \}^T [K_{GN}] \{ \phi_i \} = 0$$

$$\int_L \left[EI_y \phi''_{wi}\phi''_{wj} + EI_z \phi''_{vi}\phi''_{vj} + GIt\phi'_{\theta xi}\phi'_{\theta xj} + EI_a \phi''_{\theta xi}\phi''_{\theta xj} \right] dx = \{ \phi_j \}^T [K_L] \{ \phi_i \} = 0 \; ro^2 = \frac{Iy + Iz}{A} + yc^2 + zc^2$$

In a beam, with primary strong bending {My}:

$$\int_L \left[2My \left(\beta y \phi'_{\theta xj}\phi'_{\theta xi} + \phi''_{vi}\phi_{\theta xj} \right) \right] dx = \{ \phi_j \}^T [K_{GM}] \{ \phi_i \} = 0$$

$$\int_L \left[EI_z \phi''_{vi}\phi''_{vj} + GIt\phi'_{\theta xi}\phi'_{\theta xj} + EI_a \phi''_{\theta xi}\phi''_{\theta xj} \right] dx = \{ \phi_j \}^T [K_L] \{ \phi_i \} = 0$$

$$\beta y = \frac{1}{2 \cdot Iy} \iint_A z \left(y^2 + z^2 \right) dA - zc$$

In a beam-column, with primary axial and strong bending {P, My}:

$$\int \left[2My \left(\beta y \phi'_{\theta xj}\phi'_{\theta xi} + \phi''_{vi}\phi_{\theta xj} \right) + P \left(\phi'_{vi}\phi'_{vj} + \phi'_{wi}\phi'_{wj} + ro^2 \phi'_{\theta_x i}\phi'_{\theta_x j} + 2zc\phi'_{vi}\phi'_{\theta xj} - 2yc\phi'_{wi}\phi'_{\theta xj} \right) \right] dx =$$
$$= \{ \phi_j \}^T [K_{GNM}] \{ \phi_i \} = 0$$

$$\int_L \left[EI_y \phi''_{wi}\phi''_{wj} + EI_z \phi''_{vi}\phi''_{vj} + GIt\phi'_{\theta xi}\phi'_{\theta xj} + EI_a \phi''_{\theta xi}\phi''_{\theta xj} \right] dx = \{ \phi_j \}^T [K_L] \{ \phi_i \} = 0$$

where $\beta y = \frac{1}{2Iy} \iint_A z \left(y^2 + z^2 \right) dA - zc$, yc, zc are the shear center coordinates.

The nonlinear displacements can be expressed using these properties as:

$$\{ d_{NL} \} = \{ d_L \} + \sum_{j=1}^{n} \frac{a_j}{\left(\mu_j - 1 \right)} \{ \phi_j \} + \frac{F_{actgeo}}{\left(\mu_1 - 1 \right)} \{ \phi_1 \} \approx \{ d \} + \frac{a_1 + F_{actgeo}}{\left(\mu_1 - 1 \right)} \{ \phi_1 \}$$

$$\{ a_j \} = \frac{\{ \phi_j \}^T \{ F_{ext} \}}{\{ \phi_j \}^T [K_L] \{ \phi_j \}}$$

where F_{actgeo} define the magnitude of the imperfection and the coefficient a_j gives the expression of the linear displacements $\{d_L\}$ as a linear combination of the buckling modes.

In a structure with primary bending moments and axial forces that may induce buckling, the nonlinear displacements can be obtained as:

$$\{d_{NL}\} = \{d_L\} + \frac{a_{1MN}}{(\mu_{1MN} - 1)}\{\phi_{1MN}\} + \frac{F_{actgeo}}{(\mu_{1MN} - 1)}\{\phi_{1MN}\}$$

$$\{a_{1MN}\} = \frac{\int \left[EI_y w''\phi''_{w1} + EI_z v''\phi''_{v1} + GIt\theta_x'\phi'_{\theta x1} + EI_a\theta_x''\phi''_{\theta x1} \right] dx}{\int \left[EI_y \phi''^{\,2}_{w1} + EI_z \phi''^{\,2}_{v1} + GIt\phi'^{\,2}_{\theta x1} + EI_a \phi''^{\,2}_{\theta xi} \right] dx} = \frac{\{\phi_{1MN}\}^T \{F_{ext}\}}{\{\phi_{1MN}\}^T [K_L] \{\phi_{1MN}\}}$$

The nonlinear displacements can be expressed in a simplified way, consistently with the Eurocode where an imperfection is defined for axial effects $F_{actgeoN}$ and for strong bending (implicitly through χ_{LT}) effects $F_{actgeoM}$, as:

$$\{d_{NL}\} \approx \{d_L\} + \frac{a_{1N}}{(\mu_{1N} - 1)}\{\phi_{1N}\} + \frac{F_{actgeoN}}{(\mu_{1N} - 1)}\{\phi_{1N}\} + \frac{a_{1M}}{(\mu_{1M} - 1)}\{\phi_{1M}\} + \frac{F_{actgeoM}}{(\mu_{1M} - 1)}\{\phi_{1M}\}$$

where the nonlinear displacements $\{d_{NL}\}$ are the linear $\{d_L\}$ plus the secondary effects due to the imperfection $\frac{F_{actgeoN}}{(\mu_{1N} - 1)}\{\phi_{1N}\}$ and second order effects $\frac{a_{1N}}{(\mu_{1N} - 1)}\{\phi_{1N}\}$ due to axial forces, plus the secondary effects due to the imperfection $\frac{F_{actgeoM}}{(\mu_{1M} - 1)}\{\phi_{1M}\}$ and second order effects $\frac{a_{1M}}{(\mu_{1M} - 1)}\{\phi_{1M}\}$ (this effect is not considered by the current standards) due to strong bending moments.

So if we want to study with the simplified proposal the example in Figure 5 with primary axial and strong bending moments, 3 key analysis must be performed a linear, initial instability analysis with axial forces and a initial stability analysis with strong bending moments.

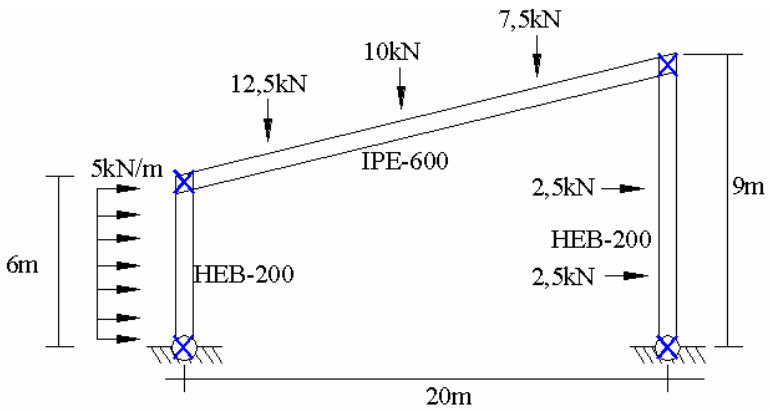

Figure 5.1. Example with axial and bending moment

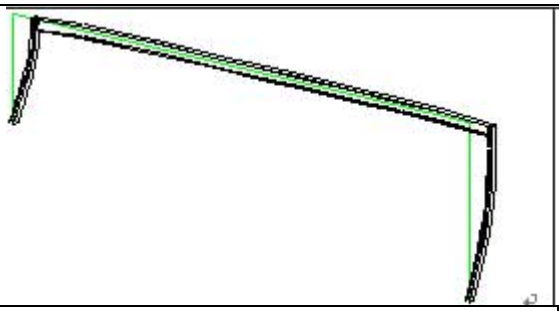

Figure 5.2 Buckling mode considering axial forces

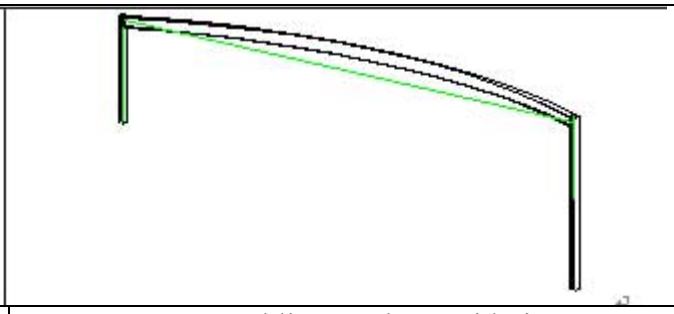

Figure 5.3 Buckling mode considering strong bending moment

Simplified method to obtain the geometric equivalent imperfection

To generalize Dutheil´s method, the collapse loads obtained by the current standards with only primary axial forces or bending moment are accepted.

The scaling factor of the geometric imperfection is obtained by equating the collapse load obtained with the proposed method considering only primary axial ($Factgeo_N$) forces or bending moment ($Factgeo_M$) with the one's obtained by the current standards (Figure 6).

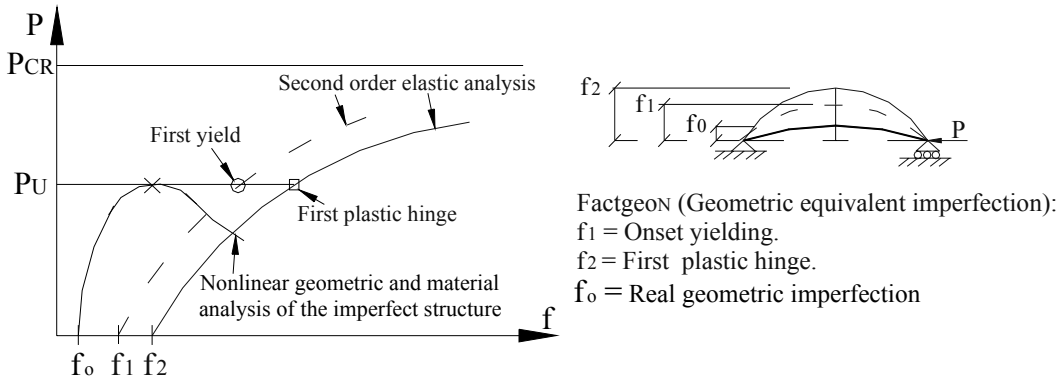

Figure 6. Calculate the geometric equivalent imperfection

So two imperfections are obtained:

A- considering only primary axial forces ($Factgeo_N$).

B- considering only primary strong bending moments ($Factgeo_M$).

Case A. Only axial forces (Figure 7):

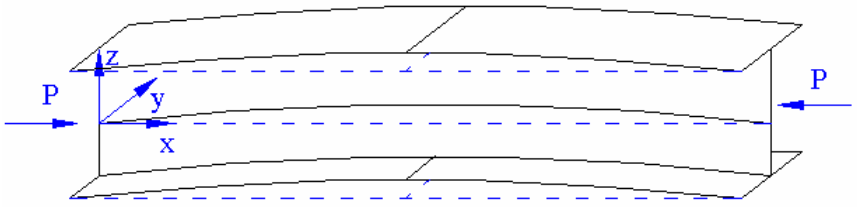

Figure 7. Considering only axial force

From the initial instability analysis with only axial forces $\left(\left[K_L\right]+\mu_{1N}\left[K_{GN}\right]\right)\{\phi_{1N}\}=\{0\}$, the first buckling load $\mu_{1N}=\mu_{cr\_N}$ and buckling mode $\{\phi_{1N}\}$ are obtained.

To calculate the collapse load $\mu_{collapse\_N}$ considering only the axial internal forces, the collapse load of each column are obtained according to:

The Spanish standard (EA-95) $P_U^{KB}=\dfrac{A^{KB}\sigma_e}{\omega^{KB}}$

The Eurocode 3 as $P_U^{KB}=\dfrac{A^{KB}\sigma_e\chi^{KB}}{\gamma_{m1}}$

where the superscript KB denotes the column number KB, and ω, χ depend on the normalized slenderness $\bar{\lambda}^{KB} = \sqrt{\frac{A\sigma_e}{\mu_{1N} P_{KB}}}$, see Buckling curve (Figure 8).

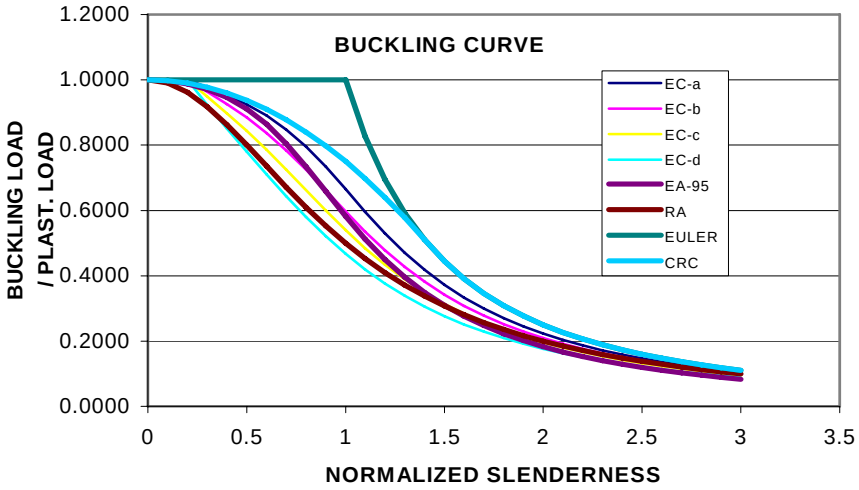

Figure 8. Buckling curves

Hence $\mu^{KB}_{collapse\_N} = \frac{A^{KB}\sigma_e}{P_{KB}\varpi^{KB}}$; $\mu^{KB}_{collapse\_N} = \frac{A^{KB}\sigma_e\chi^{KB}}{P_{KB}\gamma_{m1}}$

And the collapse load of the structure is $\mu_{collapse\_N}$ = minimum $\{\mu^{1}_{collapse\_N}, \ldots, \mu^{NB}_{collapse\_N}\}$

The initial stability analysis gives the buckling modes and the secondary internal forces developed when the structure has an imperfection given by the first buckling mode. This can be calculated at the collapse load of the structures $\mu_{collapse\_N}$ as:

$$Mys = -EIy\frac{F_{actgeoN}}{\gamma - 1}\frac{d^2\phi_w}{dx^2}$$

$$Mzs = EIz\frac{F_{actgeoN}}{\gamma - 1}\frac{d^2\phi_v}{dx^2}$$

$$Bis = EIa\frac{F_{actgeoN}}{\gamma - 1}\frac{d^2\phi_{\theta x}}{dx^2}$$

$$\gamma = \frac{\mu_{cr\text{最}ica\_N}}{\mu_{collapse\_N}}$$

The geometric imperfection ($Factgeo_N$) is obtained imposing the collapse condition for $\mu_{collapse\_N}$, of the structure with the primary {N} and secondary {M_{ZS}, M_{YS}, Bi_S} internal forces calculated:

$$\frac{N_{KB}\cdot\mu_{collapse\_N}}{N^{KB}_{el}} + \frac{M^{KB}_{ZS}}{M^{KB}_{zel}} + \frac{M^{KB}_{YS}}{M^{KB}_{yel}} + \frac{Bi^{KB}_{s}}{Bi^{KB}_{el}} \le 1$$

In case that the section is class 2 this will be given by the formation of the first plastic hinge (a more accurate result can be obtained using the appropriate cross section interaction formulae):

$$\frac{N_{KB}\cdot\mu_{collapse\_N}}{N^{KB}_{pl}} + \frac{M^{KB}_{ZS}}{M^{KB}_{zpl}} + \frac{M^{KB}_{YS}}{M^{KB}_{ypl}} + \frac{Bi^{KB}_{s}}{Bi^{KB}_{pl}} \le 1$$

Example nº1: A simply supported beam-column with out of plane buckling restrained is studied, geometry definition and loading in Figure 9.

$$\{d_{NL}\} \approx \{d_L\} + \frac{a_{1N}}{(\mu_{1N}-1)}\{\phi_{1N}\} + \frac{F_{actgeoN}}{(\mu_{1N}-1)}\{\phi_{1N}\}$$

$$\{\phi_{1N}\} = \{\phi_v\} = \left\{\operatorname{sin}\left(\frac{\pi \cdot x}{L}\right)\right\} \;\; ; \;\; F_{actgeoN} = \frac{\sigma_e (1-\chi) Wz}{Pcr\left(\frac{1}{\gamma - 1}\right)}$$

Hence

$$v \approx \frac{M}{2EIz} x(L-x) + \left(\frac{4ML^2}{\pi^3 EIz} + \frac{\sigma_e (1-\chi) Wz}{Pcr\left(\frac{1}{\gamma - 1}\right)} \right) \frac{sen\left(\frac{\pi x}{L}\right)}{(\mu_1 - 1)}$$

where $Pcr = \dfrac{\pi^2 EIz}{L^2}$

The "exact" solution is:

$$v = \frac{M}{P}\left[\left(\frac{sen(kx)}{\tan(kL)} - \cos(kx) - \frac{x}{L} + 1\right) - \left(\frac{sen(kx)}{sen(kL)} - \frac{x}{L}\right)\right] + \frac{F_{actgeoN}}{(\mu_{1N}-1)}\{\phi_{1N}\}; \; k = \sqrt{\frac{P}{EIz}}$$

In Figure 9 can be appreciated that the internal bending moments are the primary ones plus the amplification of this due to the axial force plus the ones due to the imperfection.

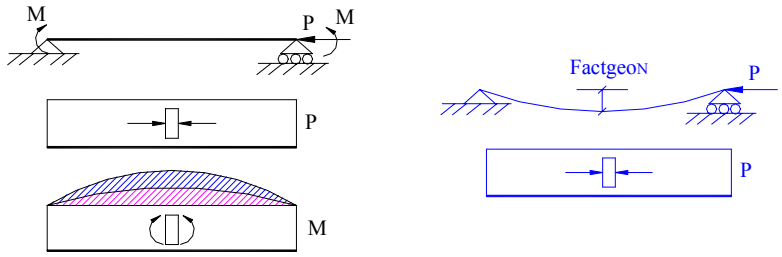

Figure 9. Example 1

Case B. Only strong bending moment (Figure 10):

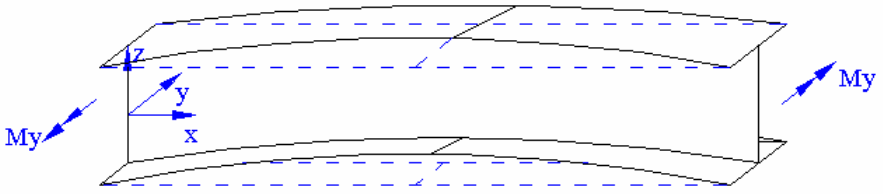

Figure 10. Considering only strong bending moments.

From the initial instability analysis with only strong bending moments $\left([K_L] + \mu_{1M}[K_{GM}]\right)\{\phi_{1M}\} = \{0\}$, the first buckling load $\mu_{1M} = \mu_{cr\text{最}ca\_M}$ and buckling mode $\{\phi_{1M}\}$ are obtained.

To calculate the collapse load considering only the bending moments $\mu_{collapse\_M}$, the collapse load of each beam are obtained according to:

The Eurocode 3 as $M_U^{KB} = \dfrac{Wy^{KB}\sigma_e\chi_{LT}{}^{KB}}{\gamma_{m1}}$

where χ_{LT} depend on $\bar{\lambda}^{KB} = \sqrt{\dfrac{W\sigma_e}{\mu_{1M}My_{KB}}}$

Hence $\mu_{collapse\_M}^{KB} = \dfrac{Wy^{KB}\sigma_e\chi_{LT}{}^{KB}}{My_{KB}\gamma_{m1}}$

And the collapse load of the structure is $\mu_{collapse\_M}$ = minimum $\{\ \mu_{collapse\_M}^{1}\ , \ldots ,\ \mu_{collapse\_M}^{NB}\ \}$

The initial stability analysis gives the buckling modes and the secondary internal forces developed when the structure has an imperfection given by the first buckling mode. These can be calculated at the collapse load of the structures $\mu_{collapse\_M}$ as:

$$Mzs = EIz\frac{F_{actgeoM}}{\gamma - 1}\frac{d^2\phi_v}{dx^2}$$

$$Bis = EIa\frac{F_{actgeoM}}{\gamma - 1}\frac{d^2\phi_{\theta x}}{dx^2}$$

$$\gamma = \frac{\mu_{cr\,\text{elástica\_}M}}{\mu_{collapse\_M}}$$

The geometric imperfection ($Factgeo_M$) is obtained imposing the collapse condition of the structure with the primary $\{M_Y\}$ and secondary $\{M_{ZS}, Bi_S\}$ internal forces:

$$\frac{M_Y^{KB}\mu_{collapse\_M}}{M_{yel}^{KB}} + \frac{M_{ZS}^{KB}}{M_{zel}^{KB}} + \frac{Bi_S^{KB}}{Bi_{el}^{KB}} \le 1$$

In case that the section is class 2 this will be given by the formation of the first plastic hinge (a more accurate result can be obtained using the appropriate cross section interaction formulae):

$$\frac{M_Y^{KB}\mu_{collapse\_M}}{M_{ypl}^{KB}} + \frac{M_{ZS}^{KB}}{M_{zpl}^{KB}} + \frac{Bi_S^{KB}}{Bi_{pl}^{KB}} \le 1$$

Example nº2 : A simply supported beam under strong bending moment and a sinusoidal distributed load p_y is studied .Geometry definition and loading in Fig. 11.

$$\{d_{NL}\} \approx \{d_L\} + \frac{a_{1M}}{(\mu_{1M} - 1)}\{\phi_{1M}\} + \frac{F_{actgeoM}}{(\mu_{1M} - 1)}\{\phi_{1M}\}$$

$$\{\phi_{1M}\} = \begin{Bmatrix}\phi_v\\ \phi_{\theta x}\end{Bmatrix} = \begin{Bmatrix}\sin\left(\dfrac{\pi x}{L}\right)\\ \dfrac{\pi^2 EIz}{\dfrac{L^2}{Mcr}}\sin\left(\dfrac{\pi x}{L}\right)\end{Bmatrix};\ F_{actgeoM} = \frac{\sigma_e(1-\chi_{LT})(\gamma-1)}{\gamma_{m1}Pz\left[\dfrac{1}{W_{zel}} + \dfrac{EIa\pi^2}{W_{Biel}McrL^2}\right]}$$

$$a_{1M} = \frac{\int\left(EIzv''\phi_{v1}'' + GIt\theta_x'\phi_{\theta x1}' + EIa\theta_x''\phi_{\theta x1}''\right)\cdot dx}{\int\left(EIz\left(\phi_{v1}''\right)^2 + GIt\left(\phi_{\theta x1}'\right)^2 + EIa\left(\phi_{\theta x1}''\right)^2\right)\cdot dx} = \frac{\dfrac{\pi^2 Mzo}{2L}}{\dfrac{\pi^4 EIz}{L^3}} = \frac{1}{2}\frac{L^2 Mzo}{\pi^2 EIz}$$

Hence:

$$\begin{Bmatrix} v \\ \theta_x \end{Bmatrix} = \frac{Mzo}{Pz} sen\left(\frac{\pi x}{L}\right) \left[\begin{Bmatrix} 1 \\ 0 \end{Bmatrix} + \left(\frac{1}{2(\mu_1 - 1)} + \frac{\dfrac{\sigma_e (1-\chi_{LT})(\gamma - 1)}{\gamma_{m1} Mzo \left[\dfrac{1}{W_{zel}} + \dfrac{EIa\pi^2}{W_{Biel} McrL^2} \right]}}{(\mu_1 - 1)} \right) \begin{Bmatrix} 1 \\ \dfrac{Pz}{Mcr} \end{Bmatrix} \right]$$

where $Mcr = \dfrac{\pi^2 EIz}{L^2} \sqrt{\left(\dfrac{Ia}{Iz} + \dfrac{L^2 GIt}{\pi^2 EIz} \right)}$; $Pz = \dfrac{\pi^2 EIz}{L^2}$

The "exact" solution is:

$$\begin{Bmatrix} v \\ \theta_x \end{Bmatrix} = \frac{Mz_o \sin\left(\dfrac{\pi x}{L}\right)}{Mcr^2 - My^2} \begin{Bmatrix} \left(GIt + \dfrac{\pi^2 EIa}{L^2} \right) \\ My \end{Bmatrix} + \frac{F_{actgeoM}}{(\mu_{1M} - 1)} \{\phi_{1M}\}$$

In Figure 11 can be appreciated that the internal weak bending moments are the primary ones plus the amplification of this due to the strong bending moments plus the ones due to the imperfection. Secondary bimoments and torsion appear. In the current standards only the effects of the imperfection are considered.

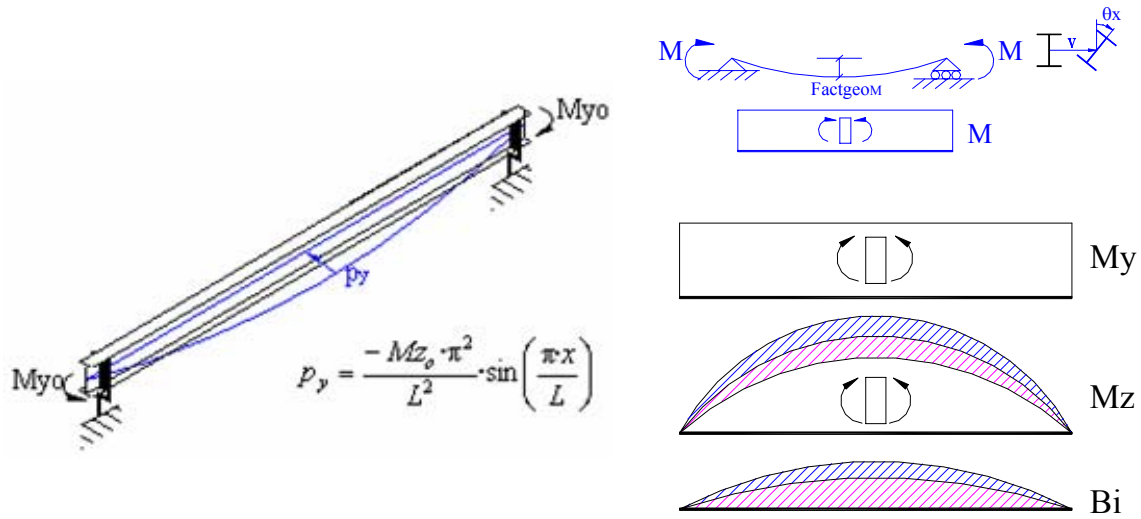

Figure 11. Example 2

$$\frac{M_Z^{KB} + M_{ZSM}^{KB}}{M_{zel}^{KB}} + \frac{M_Y^{KB}}{M_{yel}^{KB}} + \frac{Bi^{KB} + Bi_{SM}^{KB}}{Bi_{el}^{KB}} \leq 1$$

3. DESIGN IMPLEMENTATION

The implementation of this method is simple as it can be seen in the flow diagram of Figure 12. The steps followed are the described in section nº2.

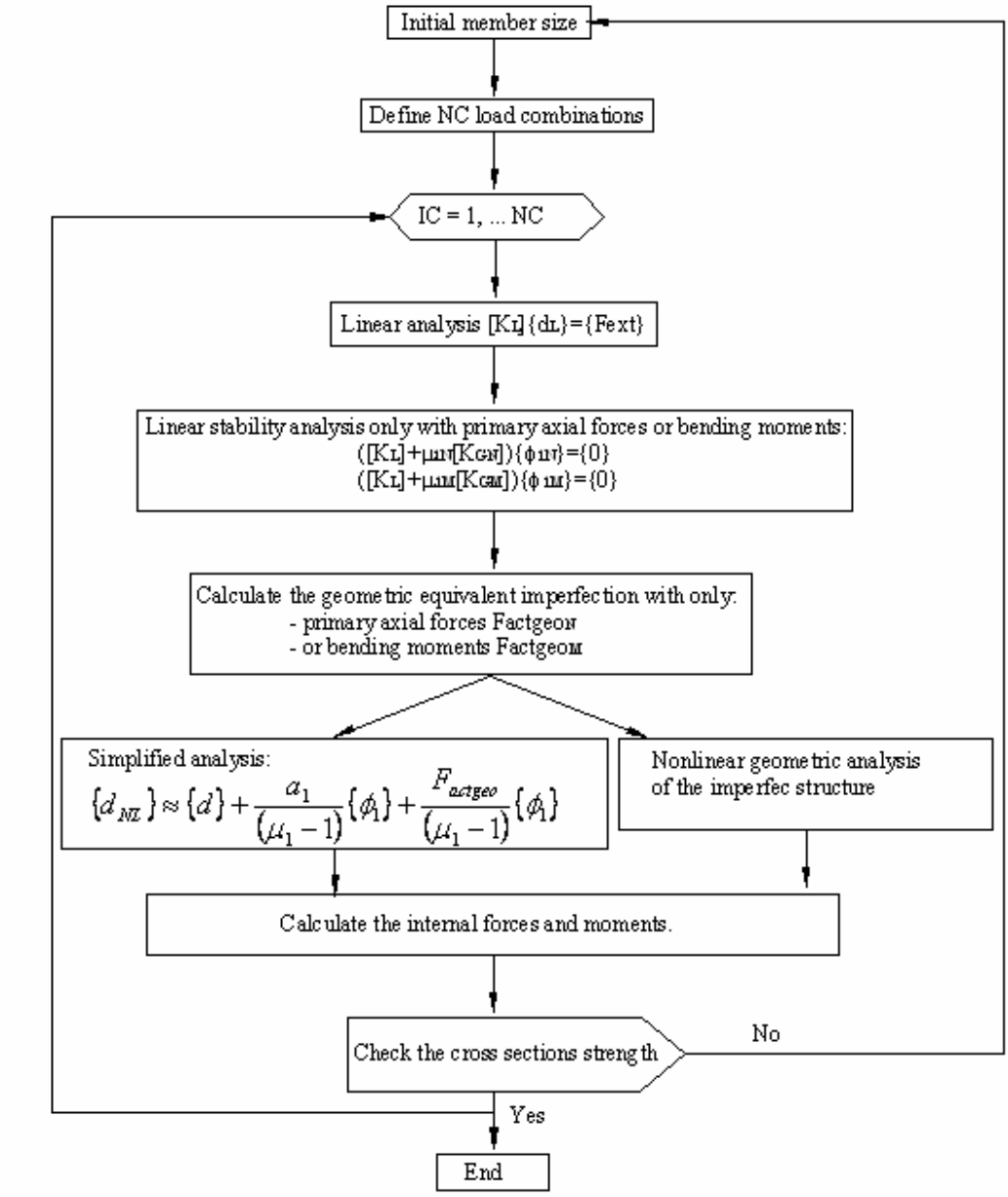

Figure 12. Design implementation

If the simplified method is chosen only the cross section strength check has to be made. For Class 3 sections:

$$\frac{N_{KB}}{N_{el}^{KB}} + \frac{M_Z^{KB} + M_{ZSN}^{KB} + M_{ZSM}^{KB}}{M_{zel}^{KB}} + \frac{M_Y^{KB} + M_{YSN}^{KB}}{M_{yel}^{KB}} + \frac{Bi^{KB} + Bi_{SN}^{KB} + Bi_{SM}^{KB}}{Bi_{el}^{KB}} \leq 1$$

Where N^{KB}, Mz^{KB}, My^{KB} y Bi^{KB} are the internal forces, while Mz_{SN}^{KB}, My_{SN}^{KB} y Bi_{SN}^{KB} s are the secondary effects due to the imperfection and second order effects due to axial forces. Mz_{SM}^{KB} y Bi_{SM}^{KB} are the secondary effects due to the imperfection and second order effects due to strong bending moments.

4. EXAMPLES

Several examples are presented to clarify some of the ideas behind the proposed methodology, in first place the geometric imperfection obtained according to 2.3 are compared with the one´s obtained with current standards, in second place the second order effects associated to the buckling modes are plotted for a 2 span beam, at last the results for pitched roof frames are summarized.

Geometric equivalent imperfection proposal vs Eurocode 3

4.1.1 Steel frames

4.1.1-A One story frame

The purpose of this example is to compare the proposed geometric imperfection (Figures 13 and 14) in a one story frame with the EC-3 proposal (Figure 15) $\phi = k_c k_s \phi_0$ where $\phi_1 = \frac{1}{200}$. The columns are HEB-200 and the beam is IPE-400.

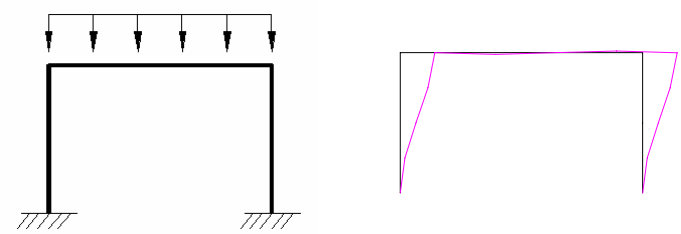

Figure 13. Loading, geometry and buckling mode. Fixed base

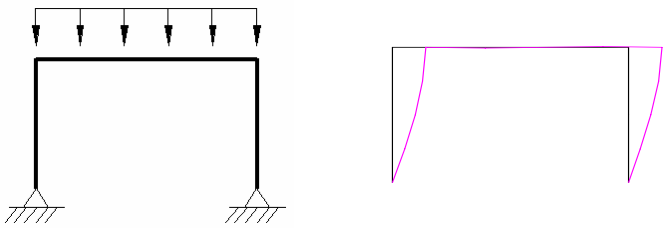

Figure 14. Loading, geometry and buckling mode. Pinned base

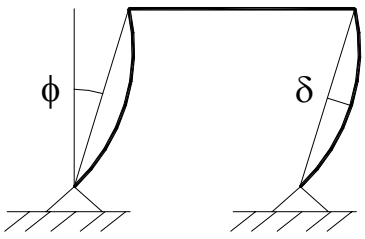

Figure 15. Geometric imperfection according to Eurocode

As can be seen for fixed column (Figure 13) there is a qualitative (shape) and quantitative difference $\phi_{EC\text{-}3}$=1/200 and $\phi_{PROPOSAL}$=1/370. While for pinned based column (Figure 14) there is only a small quantitaive difference $\phi_{EC\text{-}3}$=1/200 and $\phi_{PROPOSAL}$=1/160.

4.1.1-B Two story frame

The same conclusions than for a one story are obtained. As can be seen for fixed column (Figure 16) there is a qualitative and quantitative difference with eurocode's proposal. While for pinned based column (Figure 17) there is a small qualitative difference.

According to the EC-3 two imperfection patterns can be used (Figure 18), it can be shown that pattern A is worst as it is close to the first buckling mode.

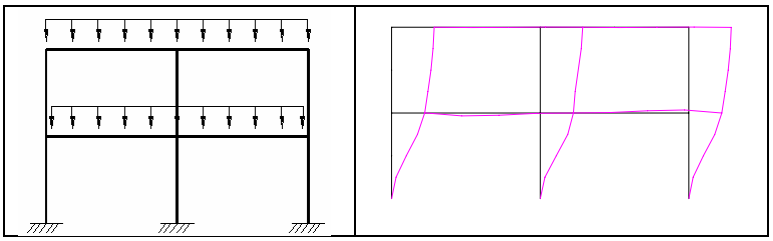

Figure 16. Loading, geometry and buckling mode. Fixed base

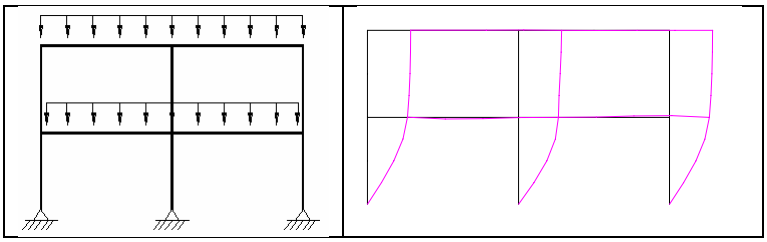

Figure 17. Loading, geometry and buckling mode. Pinned base

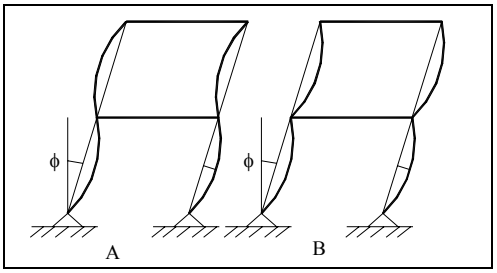

Figure 18. Two posible imperfection patterns

4.1.1-C Vogel 2 frame (Figure 19):

For this frame the geometric equivalent imperfection are also compared.

According to Eurocode the inter-storey drift imperfection is given by:

$\phi = k_c k_s \phi_0$

$$\phi_1 = ... = \phi_6 = \sqrt{0.5 + \frac{1}{3}}\sqrt{0.2 + \frac{1}{6}}\frac{1}{200} = 0.9 \cdot 0.6 \cdot \frac{1}{200} = \frac{1}{362}$$

According to the proposal the inter-storey drift imperfection is given by:

$$\phi_1 = \frac{0.009}{3.75} = \frac{1}{416};\ \phi_2 = \frac{(0.028 - 0.009)}{3.75} = \frac{1}{200};\ \phi_3 = \frac{(0.05 - 0.028)}{3.75} = \frac{1}{172};\ \phi_4 = \frac{(0.066 - 0.05)}{3.75} = \frac{1}{238};$$

$$\phi_5 = \frac{(0.08 - 0.066)}{3.75} = \frac{1}{268};\ \phi_6 = \frac{(0.083 - 0.08)}{3.75} = \frac{1}{1250}$$

There is an important qualitative difference, while the eurocode give the same interstorey drift imperfection to all the storeys, in the proposal this change (like in the buckling mode).

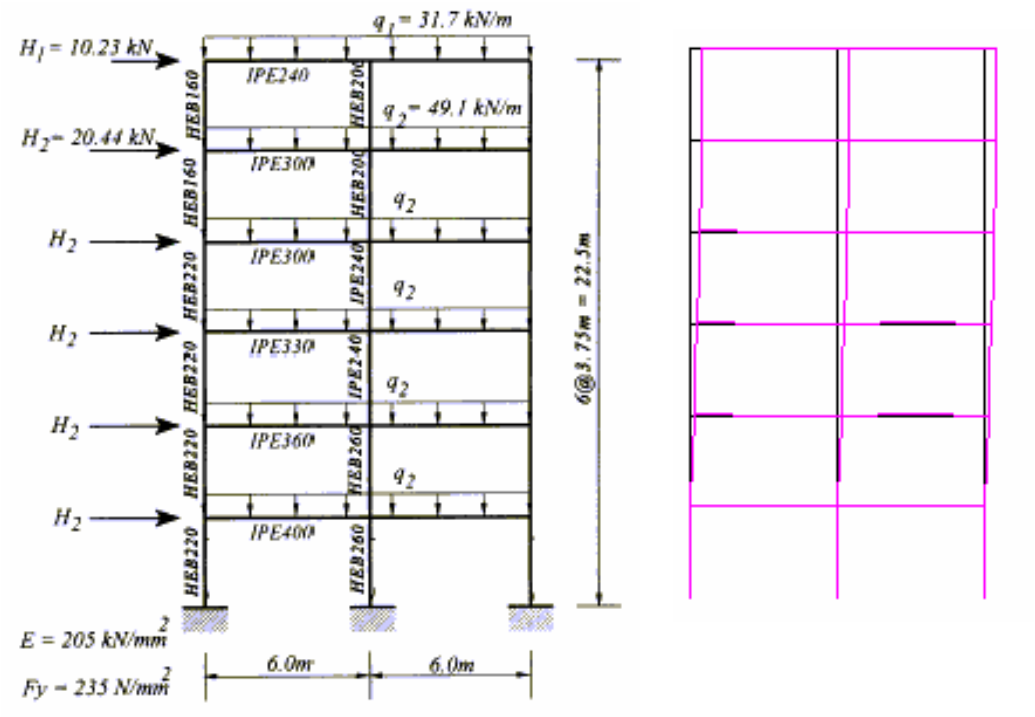

Figure 19. Loading, geometry definition and buckling mode.

4.1.1-D Orbison Frame modified (Figure 20)

The orbison frame has been modified duplicating the height in the 4 story, in this case the worst imperfection associated to the structure is a torsional global mode see Figure 20. This kind of imperfection can be easily taken into account with the methodology proposed.

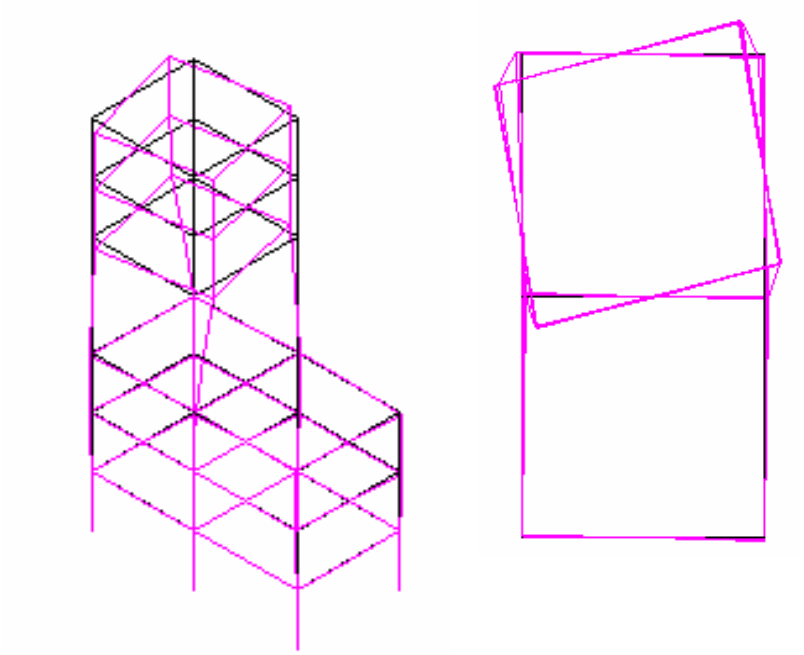

Figure 20. Geometric equivalent imperfection shape

4.1.2 Arches

Parametric studies have been done for fixed and simply supported arch structures. The imperfection is compared with the given by the Spanish standard for steel bridges (RPM-95) [6]. As can be seen Figure 22 in RPM-95 the imperfection is independent of the slenderness. For the studies a cross section Hollow square section # 400x400x10(mm) has been used. The geometry of the arches are parabolic given by $y = 4 \cdot f \cdot x \cdot (L-x)/L^2$:

f/L	Analysed cases					
0.1	1/10	2/20	3/30	4/40	5/50	6/60
0.2	2/10	4/20	6/30	8/40	10/50	12/60

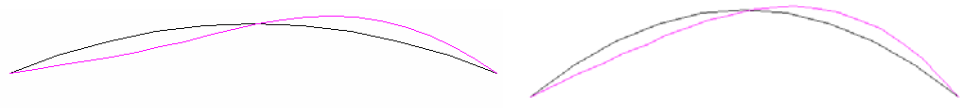

Figure 21. Geometric equivalent imperfection shape

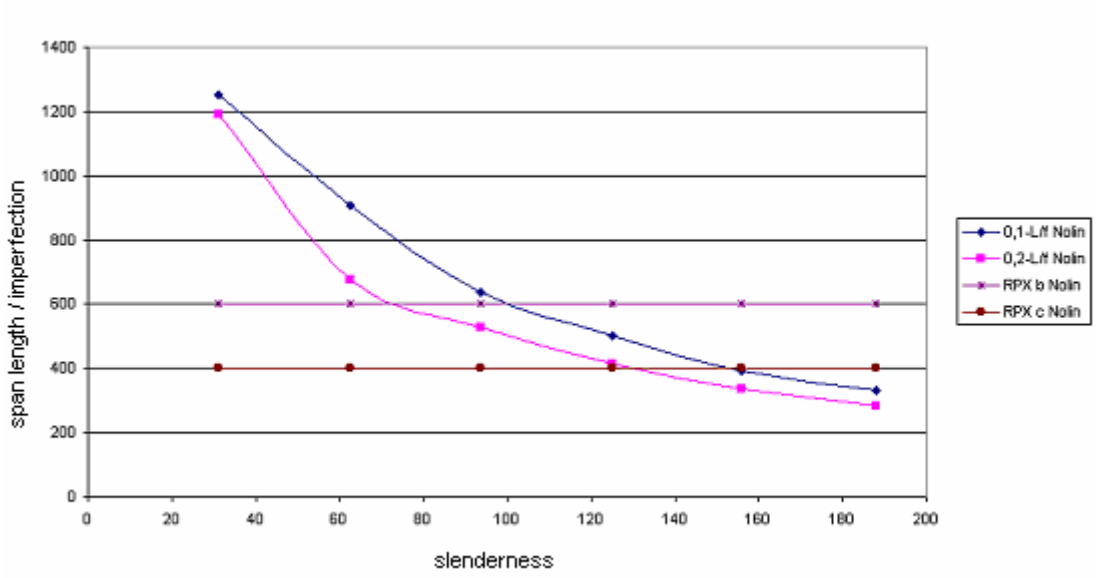

Figure 22. Comparison {span length/imperfection} vs slenderness, proposal vs RPM

The magnitude of the geometric equivalent imperfection must be dependent on the arch slenderness, and not independent as it is proposed by the RPM-95.

Secondary effects associated with the first buckling mode (Figure 23)

In a 2 span beam the buckling modes and the associated bending moment and shear force are obtained. These parameters are studied for different values of $\alpha=P_2/P_1$ α= 0, 1, 10, 100. The length of each span is 8m, and the inertia is $Iz = 551cm^4$.

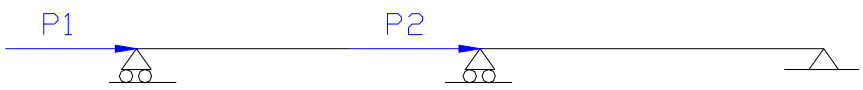

Figure 23. Loading, geometry definition

In Figure 24 the buckling modes and stresses are ploted α=0 (blue), α=1 (black), α=10 (green), α=100 (red).

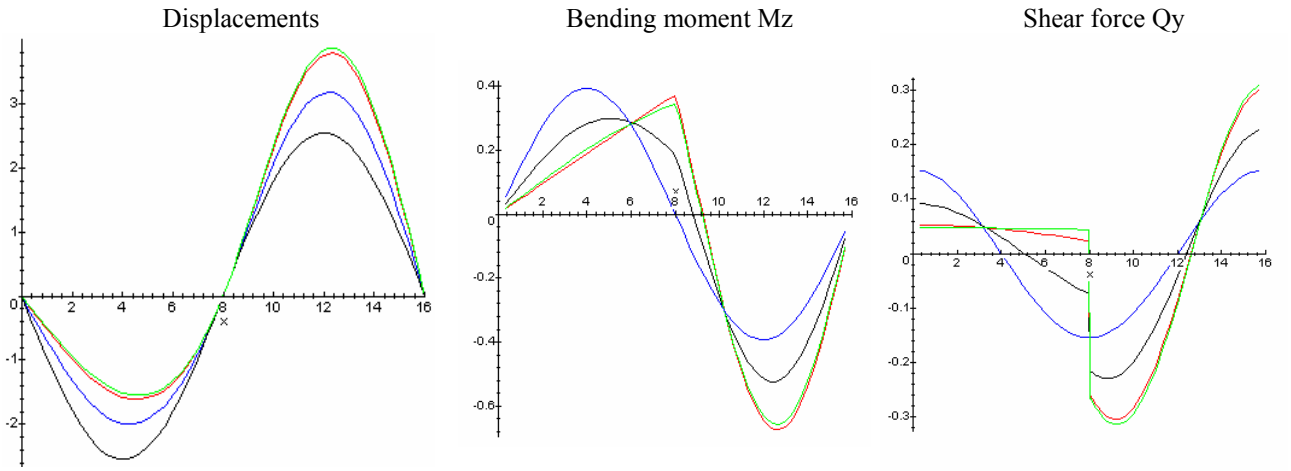

Figure 24. Geometric imperfection shape and associated bending moments and shear forces.

Pitched roof frames

Parametric studies have been done for fixed and simply supported structures, and it can be concluded that 2 buckling modes (Figure 25) are necessary, to obtain accurate results in this kind of structure.

$$\{d_{NL}\} = \{d_L\} + \frac{a_{1N}}{(\mu_{1N} - 1)}\{\phi_{1N}\} + \frac{a_{2N}}{(\mu_{2N} - 1)}\{\phi_{2N}\} + \max\left\{\frac{F_{actgeoN\_1}}{(\mu_{1N} - 1)}\{\phi_{1N}\}, \frac{F_{actgeoN\_2}}{(\mu_{2N} - 1)}\{\phi_{2N}\}\right\}$$

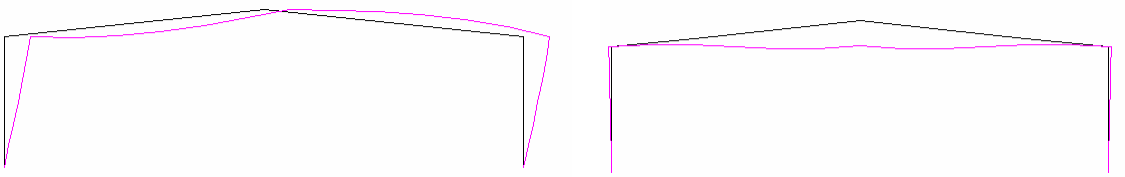

Figure 25. Usual buckling modes $\{\phi_1; \phi_2\}$ of the pitched roof frames

5. CONCLUSIONS AND FURTHER WORK

In this paper, a practical second-order advanced analysis has been developed to estimate accurately the ultimate limit state of slender steel structures, performing the analysis of an structure with a geometric equivalent imperfection using only a linear and an initial stability analysis, further details are given in [7] . The main conclusions are:

- A simplified method to evaluate the second order effects induced by axial forces and bending moments using the orthogonality properties of the buckling modes has been proposed, in the current standards the second order effects due to strong bending moments are neglected. Also an analytical solution for the analysis of imperfect structures under primary constant axial forces and strong bending moment is presented.

- A generalization of Dutheil´s theory, consistent with current standards, is presented to evaluate the geometric equivalent imperfection in any kind of structure accounting for all the key factors

influencing steel frame behavior. In some codes the proposed member imperfection {δ} for the global analysis is taken independent of the slenderness to facilitate the definition of the imperfect structure, this idea goes in the right direction but, leads to inconsistent results when compared in the simply supported column with the numerical and experimental records, it is known that the imperfection depends on the slenderness as in Perry-Robertson or Dutheil formula.

- The buckling phenomenon is associated to movements exhibiting an understandable physical background and transparency, versus the use of interaction formulae with auxiliary coefficients (ω in EA-95, χ in EC-3).

- In the present proposal the internal forces are:
  - The linear internal forces (In the structure without imperfections)
  - The amplification of the linear internal forces induced by the primary axial forces.
  - The secondary effects induced by the axial load in the imperfect structure.
  - The amplification of the linear internal forces induced by the primary strong bending moments.
  - The secondary effects induced by the strong bending moments in the imperfect structure.

- The strength check is made at the section level with the "real" internal forces obtained from the analysis, avoiding complex interaction formulae at the member level.

- Buckling is analysed as a global problem, instead of a problem only related to the members with primary axial or bending internal forces, taking into account the interaction between the members of the structure.

- The method is applied to steel frames, pitched roof frames and arches. Comparing the results with the one's obtained with current standards (EA-95, EC-3, RPM-95):
  - Frames: The Eurocode by means of member and frame imperfection tries to approach to buckling mode imperfection. Presenting the disadvantage that in a complex case is not clear which should be the direction of these imperfections.
  - Pitched roof frames: It is necessary to work with two buckling modes to obtain accurately the second order effects.
  - Arches: Simply supported, fixed and statically determinate (three hinge) arches have been studied, the conclusions are similar for all of them. The magnitude of the geometric equivalent imperfection is dependent on the arch slenderness, and not independent as it is proposed by the RPM-95.

NOTATION

E = Young modulus
Iz = Inertia about z axis
Iy = Inertia about y axis
A = Area
G = Shear modulus
It = Torsional modulus
Ia = Warping modulus
p_x = Distributed load in direction x (axial)

p_y = Distributed load in direction y
p_z = Distributed load in direction z
m_x = Distributed load in direction x
u = Displacement in direction x
v = Displacement in direction y
w = Displacement in direction z
θx = Torsional rotation
In the displacement the subscript "p" denotes perturbation, "i" imperfection.
N = Axial force
My = Bending moment about axis y (strong)
Mz = Bending moment about axis z (weak)
Bi = Bimoment
Mx = Torsional moment
Qy = Shear force in direction y
Qz = Shear force in direction z
$[K_L]$ = Linear stiffness matrix
$[K_G]$ = Geometric stiffness matrix
$[K_{GN}]$ = Geometric stiffness matrix, considering only axial forces
$[K_{GM}]$ = Geometric stiffness matrix, considering only strong bending moment
$[K_{GNM}]$ = Geometric stiffness matrix, considering axial forces and strong bending moment
$\{d_{imp}\}$ = Movements that define the geometric imperfection
$\{F_{ext}\}$ = External forces
ϕ_{vi} = Displacement in direction y of the buckling mode i
ϕ_{wi} = Displacement in direction z of the buckling mode i
$\phi_{\theta xi}$ = Torsional rotation of the buckling mode i
$\{\phi_1\}$ = First buckling mode
$\{\phi i\}$ = Buckling mode i
Wy = Section modulus about axis y
Wzel = Elastic section modulus about axis z

REFERENCES

[1] ENV 1993-1-1, "Eurocode 3: Design of steel structures, Part 1.1: general rules and rules for buildings", CEN, 1992.

[2] Chen, W.F. and Atsuta, T., "Theory of beam columns Vol. 2: Space behaviour and design". Mc Graw Hill, U.S.A., 1976.

[3] Chan, S.L. and Zhou, Z.H., "Second order analysis of frame using a single imperfect element per member", Journal of Structural Engineering, ASCE, 1995, 121(6), pp.939-945.

[4] Kim, S.E. and Chen, W.F., "Design guide for steel frames using advanced analysis program", Engineering Structures, 1999, 21, pp.352–364.

[5] Clarke, M.J., Bridge, R.Q., Hancock, G.J. and Trahair, N.S., "Advanced analysis of steel building frames", Journal of Constructional Steel Research, 1992, 23, pp.1-29.

[6] RPM-95, "Recomendaciones para el proyecto de puentes metálicos para carreteras". Ed. Ministerio de fomento, 1996.

[7] Aguero, A., "Metodo aproximado para estimar el estado limite ultimo en entramados metalicos esbeltos", Tesis Doctoral, Valencia, Spain. Ed. By Proquest, 2003.

[8] Crisfield, M.A., "Non-linear finite element analysis of solids and structures", volume 2, John Wiley and Sons, 1997.

[9] Culver, C.G., “Initial imperfections in Biaxial Bending Equations”, Journal of the structural Division, ASCE, 1966, 92(ST2), Proc. Paper 4772, April, pp.63-83.
[10] Timoshenko, S.P. and Gere, J.M., “Theory of elastic stability”, McGraw Hill, New York, 1961.
[11] Trahair, N.S., “Flexural-torsional buckling of structures”, E&FN SPON, 1993
[12] Zienkiewicz, O.C. and Taylor, R., “The finite element method Solid Mechanics”, Volume II, Butterworth-Heinemann, 2000.

ADVANCED ANALYSIS AS A NEW DIMENSION FOR STRUCTURAL STEEL DESIGN

S.L. Chan[1] and W.F. Chen[2]

[1]*Department of Civil and Structural Engineering, The Hong Kong Polytechnic University*

[2]*Department of Civil Engineering, Hawaii University, USA*

Abstract: As an alternative to the prescriptive design based on individual member capacity check, performance-based design by direct simulation of structural system behaviour under ultimate loads is developed, both in concept and in computer implementation. The method has been proposed as an alternative design against the conventional prescriptive design using equations in codes with somewhat unreliable assumptions.

This paper discusses the implementation of the method to ultimate design of a benchmark plane frame and a stadium constructed for the East Asian Game 2005 in Macau. The results show the advantages of the method in efficiency, economy and safety. The approach represents a new design practice for engineers in the 21st century.

This practical advanced analysis will result in a more uniform reliability and safety for the designed frames such that redundant members will not be over-designed and key members under-designed. Research along the line of more accurate simulation should be carried out in future rather than refining the prescriptive member-based design formulae. Although general purpose finite element packages developed decades ago are, in principle, able to design steel structures by non-linear analysis using beam-column and shell elements, their daily application to civil engineering structures is impractical as many design code requirements cannot be simulated directly and automatically.

Keywords: Second-order analysis, advanced analysis, P-Δ–δ effects, elastic analysis, plastic analysis and design.

1. INTRODUCTION

In the conventional structural design, the effective length and bending moment are assumed and determined and then used with the prescriptive design rules. The error connected with the assumption of effective length factor (L_e/L) can be very large and the method is limited to types of structures such as those with elastic critical load factor greater than 3 for Eurocode-3 [1], 4 in BS5950 [2] and 5 in AS4100 [3].

Buckling is an interactive member and system behaviour that the buckling strength of a member relies on the member and system stiffness. For example, a wind-cross in a portal frame in Figure 1 assists the whole structure as well as every member against buckling. This characteristic is different from stress computation by a linear analysis where the stress in a column is not much affected by the stress of another member far from this column and the St. Venant principle holds.

Elastic and elastic-plastic analysis of steel frames have been carried out extensively by many researchers. Chen and his co-workers [4,5] developed a series of analytical tools for accurate analysis of steel frames with different levels and scope of application. A unified approach was proposed by White and Hajjar [6]. Barreto and Camotim [7] developed a procedure for computer-aided design of steel frames. Liew et al. [8] and Xu [9] formulated design and analysis procedure for general steel frames. Li and Li [10] derived tapered element for non-linear analysis. Goncalves and Camotim [11] suggested a rational method of steel frame analysis and design. Recently, computational research on use of refined element for large deflection, small strain elastic or plastic analysis of slender frames is conducted by Chan and Zhou [12], Chan and Cho [13] and Gu and Chan [14]. The work gradually transforms the research on the topic of advanced analysis to a practical tool used in a typical design office with reasonable computer resource such as personal computers.

In recent years, construction boom in southern part of China including Hong Kong and Macau has lead to the need of application of the latest technology in structural steel design, not only for effective and economical use of material, but also for more accurate assessment of structural strength and stability and efficient design output to meet the demand of architects and project developers, as well as satisfying requirement for sustainable development which meets specific performance and safety requirements without over-designing with unnecessary material wastage.

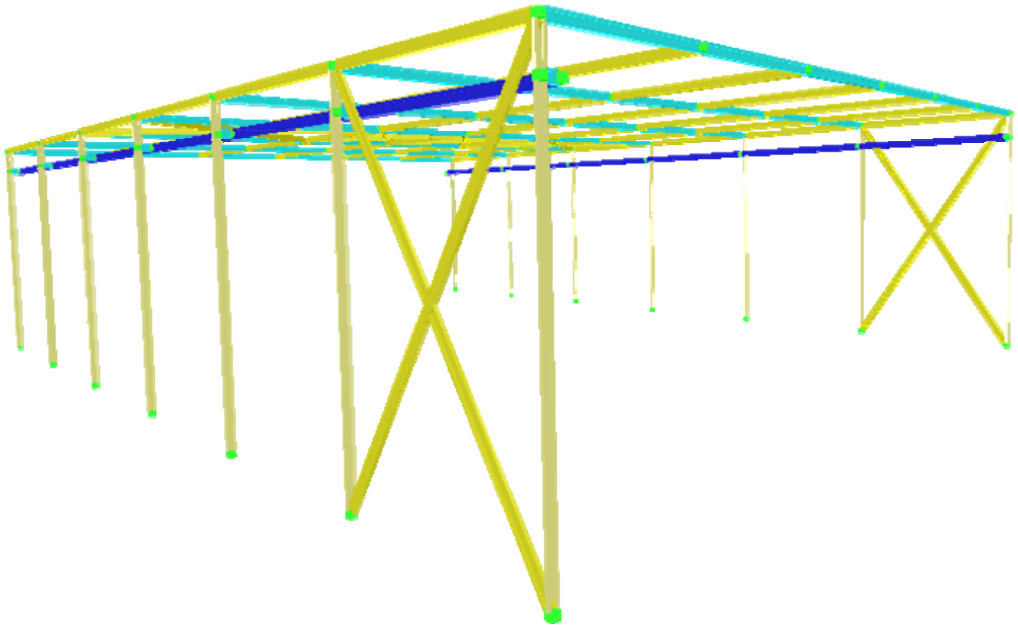

Figure 1. Wind braces in an end bay stiffens the complete portal indicating system buckling behaviour of frames

As an end product of nonlinear analysis carried out over decades, the performance-based non-linear structural design to ultimate limit state simulating the response of structures for determination of structural resistance is developed. For practical application, frame and member imperfections, which are normally considered implicitly in a first-order linear analysis and design charts, are required to be modelled explicitly in a second-order analysis. This requirement leads to significant more effort in computer program development.

It has been noted that second-order P-Δ-only elastic analysis has limited application since the method only assists to reduce the effort for moment amplification in sway frames and individual member design is still needed. As the P-δ effect considered in design curves in most national design codes only accounts for the initial curvature but not normally for the load-induced P-δ moment, the approach is not always on the safe side because of missing of P-δ moment due to load on members.

On the other hand, methods allowing for the section capacity check in place of individual member design have the advantages of convenience in use, as well as safety in covering P-δ moment induced by loads along members. As it does not require use of charts in design codes, the design is more efficient. When the extended P-Δ–δ plastic hinge analysis is used, further advantage is gained for full utilization of plastic strength reserve. The greater safety of a robust structure with higher degree of redundancy over a “brittle” determinate structure can only be explored when one uses the plastic analysis and design.

From the past observation of steel structure collapses, plastic collapse failure of structural members is uncommon even under extreme loads such as the seismic force during the Northridge earthquake in USA in 1994. Instead, instability, buckling and connection failure was more commonly reported. Thus, it is justifiable to make use of plastic strength reserve in structural members in design and resource should be placed more on checks and design against robustness, buckling and connection fracture.

Furthermore, the latest design codes including the AISC code [3], the Eurocode-3 [1] and the Hong Kong codes [15] have provided a legal basis for practical applications. This safety can further be ensured by calibrating of the buckling strength of single members against the results by conventional design, as indicated in a calibrating exercise in this paper.

On the other hand, with the availability of the more scientific design method of advanced analysis, the mis-use of “guess” effective length to practical design may lead to professional negligence in case of structural collapse. The extension of the present method to other limit states such as the structural fire engineering and seismic design is natural by modifying the material properties and time dependent nature of loads.

So far as the user-friendliness of the new method is concerned, the authors noted that it is more efficient since one needs not assume an effective length factor for all members individually for different load cases. This leads to a significant saving of time and effort spent on designing a structure. Although second-order plastic analysis for seismic design using a time history approach has been advocated for years, its routine use in basic design of member size appears to be uncommon in design office because of lack of robustness in iteration convergence, calibration and reliability, making the method to remain as a checking tool instead of a basic design suite. In contrast to this, the present codified is a candidate for replacing the manual effective length method in basic design for member sizing, affecting the work nature of engineers in their daily design practice.

2. LIMITATION OF THE FIRST-ORDER LINEAR ANALYSIS

As the first-order linear analysis considers the equilibrium condition at undeformed stage and ignores any material yielding in the analysis, it cannot detect any nonlinear effects due to buckling and material yield. To safeguard failure against nonlinear geometrical effects or material yield, post-analysis and member-based design must be carried out to ensure adequate member strength. Some types of buckling like snap-through buckling in Figure 2 are due to system instability and the first-order linear analysis and design concept can hardly be applied. Also, partly braced frame such as the one in Figure 3 can hardly be designed economically or safely by the method.

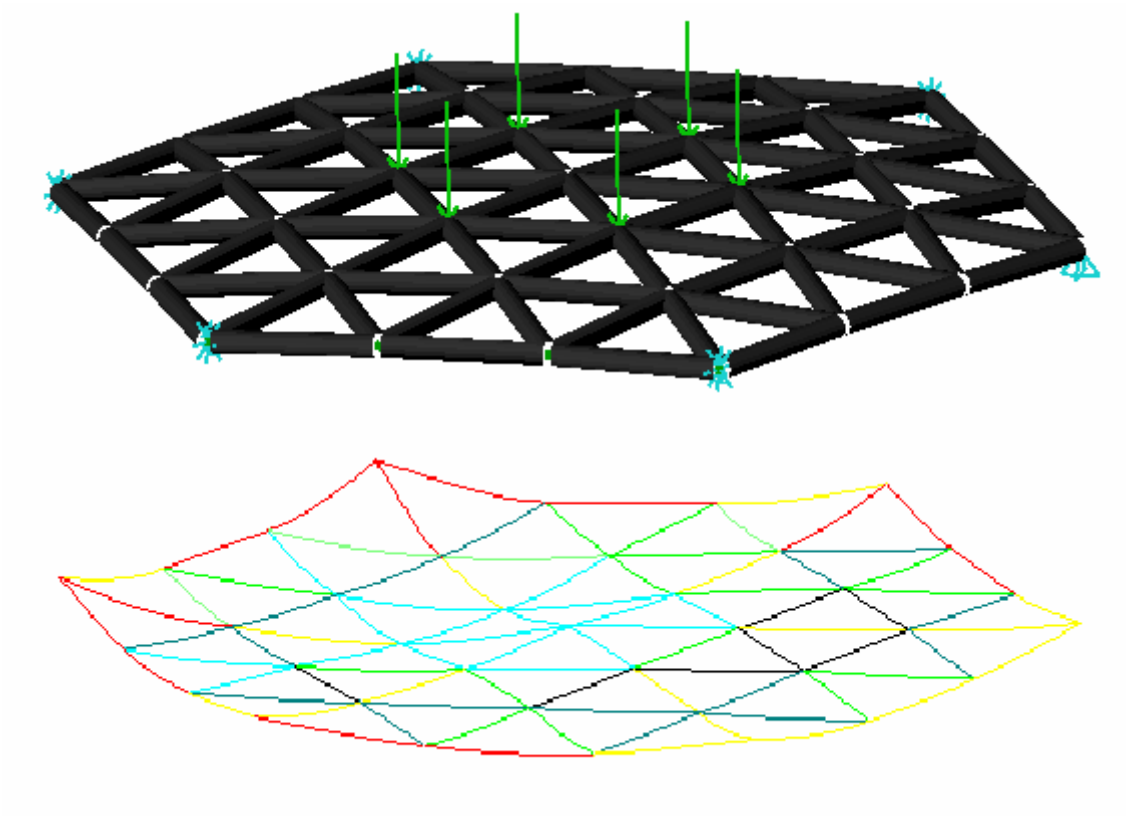

Figure 2. Snap-through system buckling behaviour

Practicing engineers quite often encounter a problem of determining an effective length factor for some members among a hundred or a thousand compression elements in a steel frame. The structural members with problematic design include the commonly used leaning columns in sway frames, dome, scaffolds and towers where additional restraining and bracing members from slabs and walls are absent.

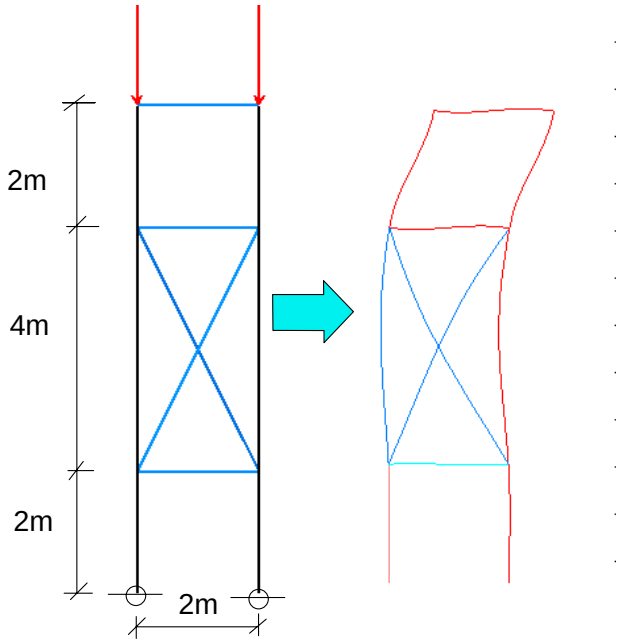

Figure 3. Locally-braced steel frame under heavy vertical loads
Should the effective length be 2m, 4m, 6m or 8m ?

3. SECOND-ORDER P-Δ-δ ELASTIC OR THE FIRST-PLASTIC HINGE ANALYSIS

Second-order analysis can further be classified into P-Δ-only and P-Δ–δ analysis. The former more simple P-Δ–only analysis considers only change of nodal coordinates while the latter second-order P-Δ–δ analysis considers both the P-Δ effect and P-δ effect due to member curvature. In order to permit the section capacity check, one must allow for sway deflection in frames and bowing in members in an analysis. Their imperfections in the form of out-of-plumbness and member initial curvature must also be accounted for.

The latest Hong Kong Steel Code [15] and the Eurocode-3 [1] have explicit requirements for these two imperfections. When these imperfections and load-induced second-order effects are considered, effective length and bending moment diagram plots are no longer required in the complete design process. This leads to a significant saving in design effort and in improving design efficiency, as well as a more rational distribution of material to members by realizing the ultimate strength and its influence to overall structural behaviour and stability.

In the analysis, every member is checked along its length by the section capacity check as,

$$\frac{P}{p_y A} + \frac{(M_y + P\Delta_y + P\delta_y)}{M_{Yy}} + \frac{(M_z + P\Delta_z + P\delta_z)}{M_{Zy}} = \varphi \le 1 \qquad (1)$$

where

Δ = nodal displacement due to out-of-plumbness frame imperfections plus sway induced by loads in the frame

δ = displacement due to member curvature / bowing due to initial imperfection and load at ends and along member length of a member. This is calculated using a curved member [12].

A = cross sectional area

p_y = design strength

M_{Yy}, M_{Zy} = yield moments about principal Y- and Z-axes (i.e. $M_{iy}=p_y Z_i$, Z=elastic modulus)

M_y, M_z = external moments about principal Y- and Z-axes

φ = section capacity factor. If $\varphi > 1$, member fails in section capacity check

For first plastic hinge design, the design load is considered to have been reached when ϕ is equal to 1. For collapse load analysis, a plastic hinge will then be inserted into the member end and the analysis continues until a plastic collapse mechanism is formed.

3.1 Imperfections in general

The Eurocode 3 [1] and the Hong Kong Steel Code [15] give detailed guidelines on method of the second-order analysis allowing for initial imperfections in frames and in members. In summary, one must consider frame and member imperfections as follows.

3.2 Frame out-of-plumbness imperfection

Frame imperfections can be considered by notional force or imperfect structural geometry obtained by an elastic critical analysis, as shown in Figure 4. For permanent structures, notional force equal to 0.5% of vertical force is applied horizontally to the structure to simulate out-of-plumbness.

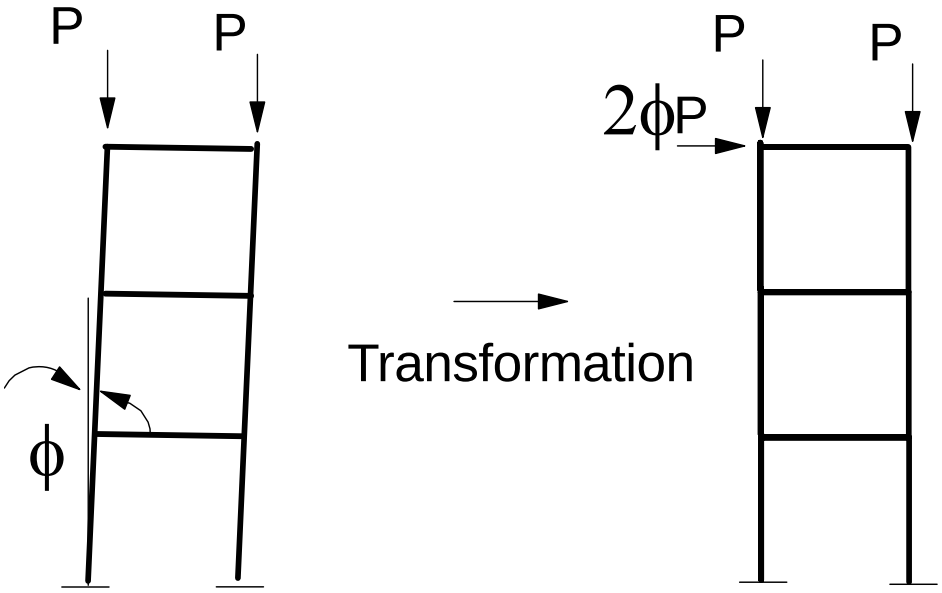

Figure 4a. Out-of-plumbness in actual structure **Figure 4b.** Equivalent notional forces

4. MEMBER BOWING IMPERFECTION

Member imperfections must be considered by use of initially curved element or several straight elements to model a member. In both methods, the direction of curvature of a member should be in the adverse direction which follows the buckling direction. The use of several straight elements to model a member is not only to predict a more accurate buckling load calculation since straight element using cubic Hermite function cannot predict accurately the buckling load by one-element-per-member [16], but it is also used to approximate the location of maximum bending moment in a beam-column.

Curved element based on stability function or PEP element allows for changing member curvature under load permits differentiation of shape function to locate the maximum bending moment as,

$$V = \frac{\partial M}{\partial x} = \frac{\partial^3 v}{\partial x^3} = 0 \qquad (2)$$

in which V is the shear, v is the lateral displacement, M is the bending moment along a member and x is coordinate along the line joining the two end nodes.

Note that if displacement v from a cubic function is used, shear force V in Equation 1 becomes a constant and location of zero shear for maximum moment along a member cannot be determined. On the other hand, the stability function for curved members proposed by Gu and Chan [14] allows for the trible differentiation for maximum moment so that the zero shear location can be determined.

4.1 Choice of element

It is important to select a suitable element for second-order analysis of practical structures of which the number of elements is usually much larger than the examples studied in most research papers. When used for analysis of practical frames, computational truncating error and efficiency become paramount important. The use of several elements to locate approximately the maximum moment is usually not a good approach for steel frame design, in a similar argument as use of a finite element package in modelling a frame by shell elements which can hardly be used in a typical design office.

A curved element possessing initial curvature is normally a much better choice in term of efficiency, robustness, reliability and accuracy. Zhou and Chan [16] proposed element suitable for plastic analysis and the element is refined here for plastic hinge analysis which is generally more suitable for large 3-dimensional structures. The PEP element is formulated on a higher order displacement function such that the stiffness matrix can predict the elastic buckling load accurately by one-element-per-member. Unlike the stability function, it does not require separated expressions for force in tension or in compression. The stiffness matrix is expressed as follows (see also Figure 5).

$$\begin{bmatrix} M_{b1} \\ M_{b2} \end{bmatrix} = \frac{EI}{L} \begin{bmatrix} K_{11} & -K_{12} \\ -K_{12} & K_{22} \end{bmatrix} \begin{bmatrix} \theta_{b1} \\ \theta_{b2} \end{bmatrix} \tag{3}$$

and

$$K_{11} = K_{22} = \frac{3(80)^2 + 800q + \left(\frac{61}{7}\right)q^2 + \left(\frac{23}{1{,}260}\right)q^3}{(80+q)^2} \tag{4}$$

$$K_{12} = \frac{48^2 + 288q + \left(\frac{29}{5}\right)q^2 + \left(\frac{11}{420}\right)q^3}{(48+q)^2} \tag{5}$$

in which M_{b1} and M_{b2} are nodal moments and θ_{b1} and θ_{b2} are conjugate rotations, K_{11}, K_{12} and K_{22} are stiffness coefficients. q is the non-dimensional axial force given by $q = \frac{PL^2}{EI}$, P is the axial force, EI is the flexural constant and L is the element length.

The element with springs at two ends can be written as,

$$\begin{bmatrix} M_{ci} \\ M_{bi} \\ M_{bj} \\ M_{cj} \end{bmatrix} = \begin{bmatrix} S_i & -S_i & & \\ -S_i & S_i + K_{ii} & -K_{ij} & \\ & -K_{ij} & S_j + K_{jj} & -S_j \\ & & -S_j & S_j \end{bmatrix} \begin{bmatrix} \theta_{ci} \\ \theta_{bi} \\ \theta_{bj} \\ \theta_{cj} \end{bmatrix} \tag{6}$$

in which M_{ci} is the moment at connection and node "i", M_{bi} is the moment at end node "i" of the beam. θ_{ci} is conjugate rotation to moment M_{ci} and S_i is the spring stiffness at connection "i" obtained from the simple formula combining the effect of semi-rigid connection and plastic hinge as,

$$S_i = \frac{S_{ci} S_{pi}}{S_{ci} + S_{pi}} \tag{7}$$

in which S_{ci} and S_{pi} are respectively spring stiffness for semi-rigid connection and plastic hinge at node "i".

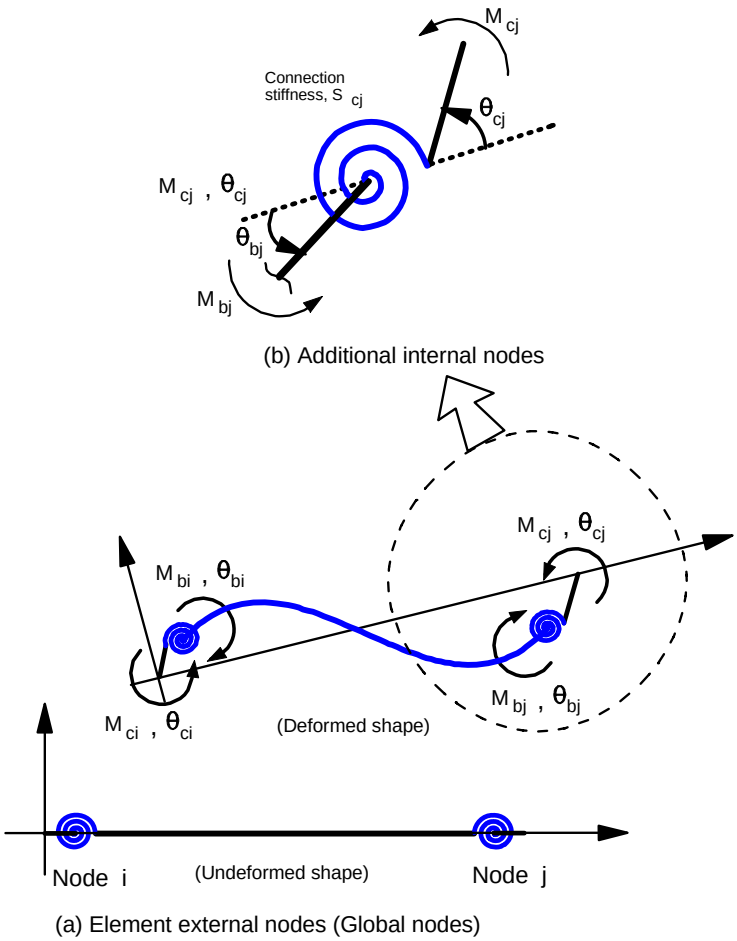

Figure 5. Beam-column element with end connection springs

After static condensation of Equation (2) for easy programming, the compact stiffness equation can be obtained as,

$$\begin{bmatrix} M_{c1} \\ M_{c2} \end{bmatrix} = \left\{ \begin{bmatrix} S_1 & 0 \\ 0 & S_2 \end{bmatrix} - \frac{\begin{bmatrix} S_1 & 0 \\ 0 & S_2 \end{bmatrix} \begin{bmatrix} S_1 + K_{11} & -K_{12} \\ -K_{12} & S_2 + K_{22} \end{bmatrix} \begin{bmatrix} S_1 & 0 \\ 0 & S_2 \end{bmatrix}}{(S_1 + K_{11})(S_2 + K_{22}) - K_{12}^2} \right\} \begin{bmatrix} \theta_{ci} \\ \theta_{cj} \end{bmatrix} \tag{8}$$

In the analysis, the element is monitored on sectional strength using equation (1). Once the section capacity factor (ϕ) is larger than 1, the plastic hinge stiffness S_p at the end closer to the section with ϕ larger than 1 is assigned a very small number for simulation of plastic hinge and the analysis is continued until the large deflection plastic collapse mechanism is formed. If higher accuracy is required, the member with ϕ close to 1 or, in computer implementation, when ϕ is larger than 0.8, the member is sub-divided into several elements for better modeling of plastic behaviour. However, from several studied numerical examples for practical frames, this sub-division is unnecessary with small difference in most cases.

If we consider both the P-δ and P-Δ effects, we then need not assume an effective length and the load capacity of a structure can then be determined by checking the sectional strength along a member.

4.2 Calibration against codes

It is obvious that the magnitude of imperfection in the proposed method affects the buckling strength of a column or a beam-column. The values of imperfections have been rationally calibrated against the existing buckling curves in design codes and the following values were obtained and used in the new Hong Kong Steel Code [15].

δ_0/L = 1/500 for curves "a"
= 1/400 for curves "b"
= 1/300 for curves "c"
= 1/200 for curves "d"

Figure 6 below shows an example of buckling design curve of a section against the Hong Kong Steel Code [15] curve "a". Similar good results can be obtained for other buckling curves or in fact buckling curves in other national codes by adjusting the δ_0. Note that δ_0 is not only for modelling of geometrical imperfection, but it is also used to consider the equivalent material imperfection due to residual stress and their values are obtained by curve-fitting of various buckling curves in codes or in test series.

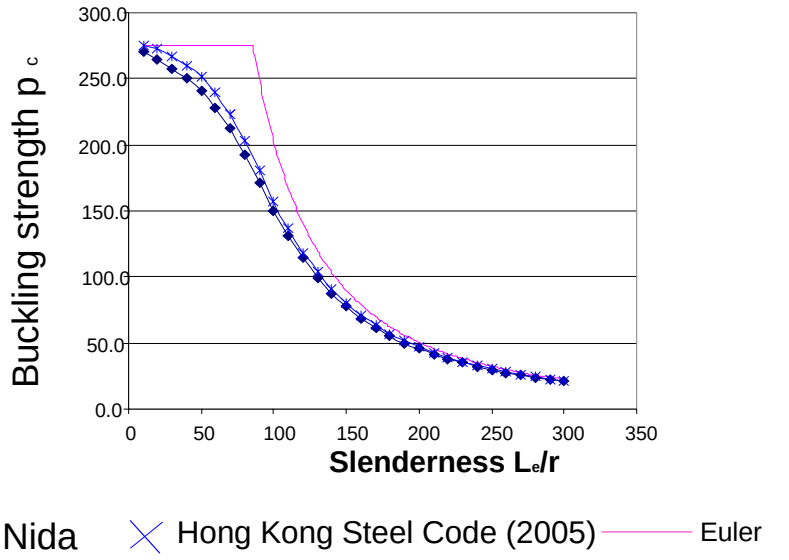

Figure 6. Buckling design curves for Curve "a" for hollow sections

5. EXAMPLES

Two examples are given here to demonstrate the application of the design method for hypothetical and real structures. The software Nida is used for all the two examples as most software available in market at the time of article is limited to P-Δ only analysis using straight cubic elements.

As mentioned previously, the use of several straight elements can theoretically model a member for accurate but approximated location of section with maximum combined axial force and moment check in Equation 1. This finite element approach was noted to be deficient in many practical applications because of easy divergence due to use of numerous elements leading to truncating numerical error, especially when the limit load is approached. A simple test is suggested for finding of the buckling strength of a pin-fixed imperfect column against the code-permitted load as in the calibration exercise in the last section.

Example 1 Design of a portal braced at one storey

The example below is an illustrative problem for second-order analysis of a simple plane frame. A similar problem was used in the USA as a benchmark example for verifying the accuracy of a design method since the effective length is not obvious. The size of the members is shown in Figure 7 and the steel grade is taken as 275 N/mm^2 and the frame is under a pair of vertical point loads of 500 kN each. Elastic modulus is used for the section capacity check in Equation 1.

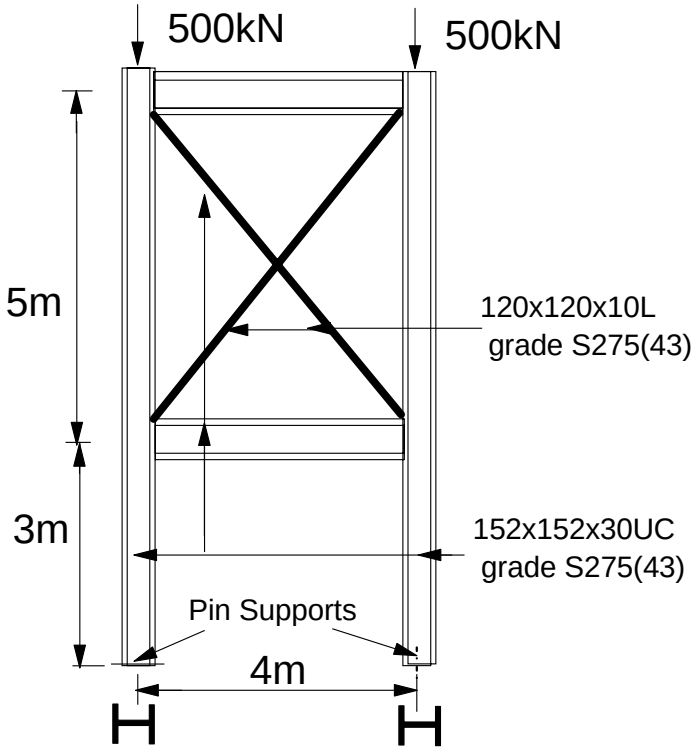

Figure 7. Plane frame braced at upper storey

The direct use of hand method is very uneconomical here since the lower storey makes the frame to be classified as sway while the upper storey column use this effective length factor for design. Further, the whole frame has a low elastic critical load factor of 1.77 to prohibit the use of the first-order linear analysis. This type of structure can be common for supporting heavy loads on top and providing high clearance at lower storey.

In the analysis, a horizontal notional force of 0.5% of the vertical load is applied to the level of the vertical load. However, for braced system such as the one discussed here, the notional force may not generate an effect as severe as using the buckling mode as imperfection shape, since the force is transferred by braces to other parts of the structure and thus the magnitude of the top deflection is not so significant.

The ultimate load of the frame is obtained from Figure 8 as 0.99 which is represented by the peak or limit load in the load vs. deflection plot. If the buckling mode imperfection of magnitude equal to 0.5% of the frame height or 40mm is used, the collapse load as the limit load in the load vs. deflection curve becomes 0.80 which is 19% below the notional force method (see Figure 9). The selected node obtained from a buckling analysis for applying the initial displacement is at the top node.

The load vs deflection curves by notional force method and by buckling mode as imperfection are indicated in Figures 9 and 10. The collapse loads are close to the first yield load since it has little redundancy after buckling of the first column. This indicates the plastic strength reserve is

dependent on structural redundancy. The right hand lower column fails first, followed by the column opposite.

The frame is re-analyzed and restrained at top by a lateral tie to other rigid structure. The application of notional force here is meaningless since it is absorbed by the fixed support. The initial shape is again taken as the buckling mode shape with magnitude equal to 0.5% of the height of the structure or 40mm. The load resistance of the frame is similar and equal to 0.98 of the design load. The load vs. deflection path is depicted in Figure 10.

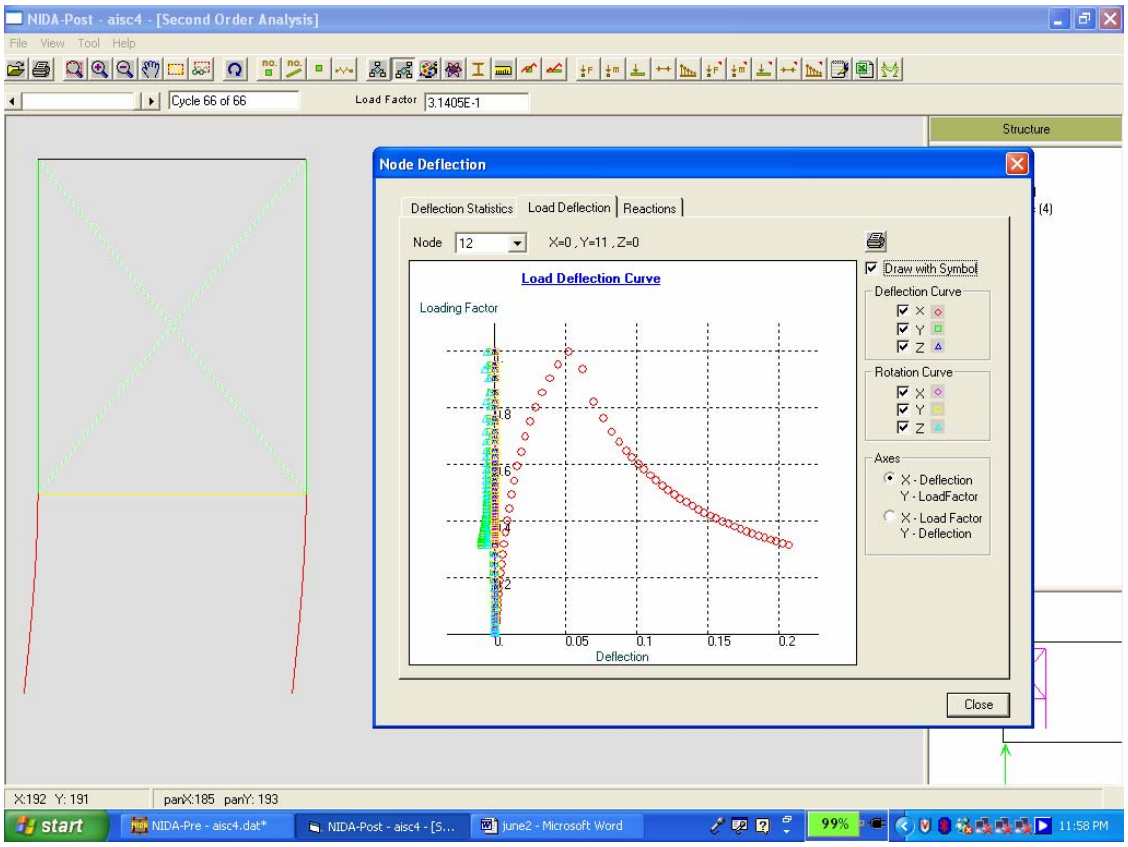

Figure 8. The load vs. deflection curve of partly braced frame by the notional force method (only the solution points are spotted and the curve[not shown] is obtained by joining these points)

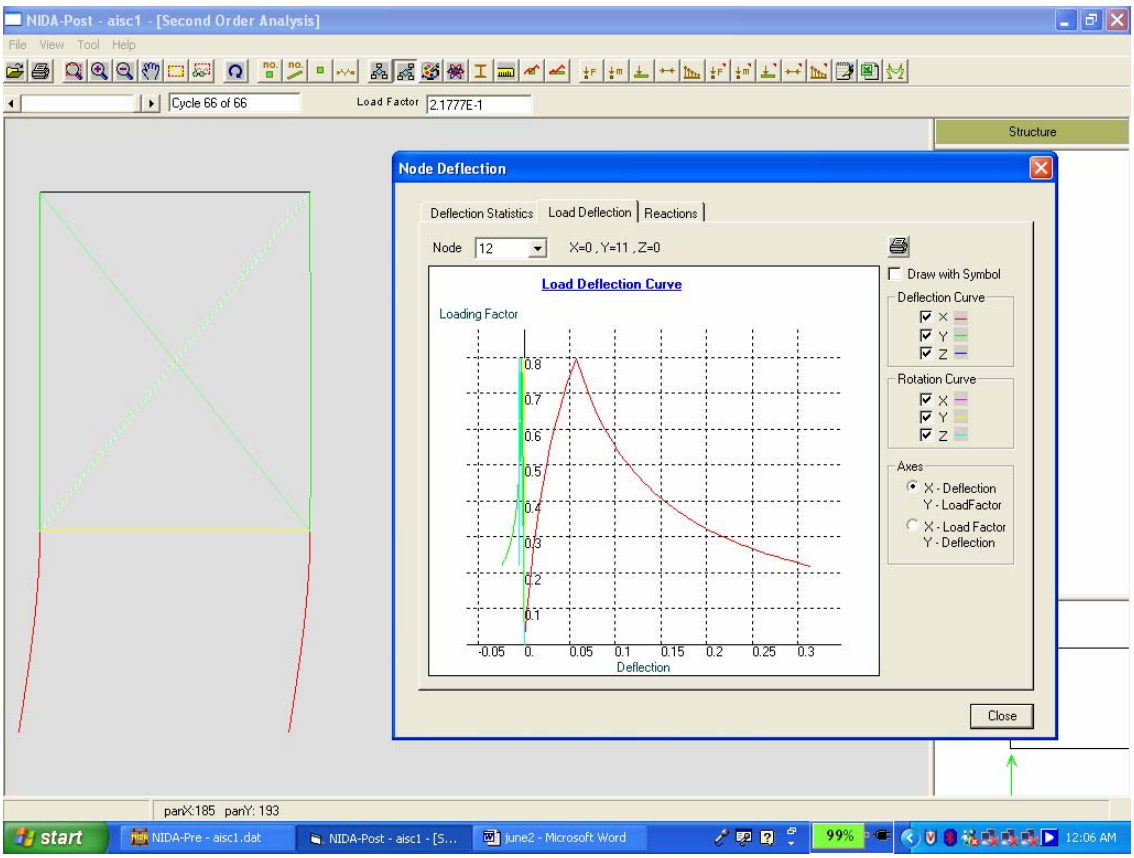

Figure 9. Load vs. deflection path of partly braced frame by the elastic eigen-buckling mode imperfection

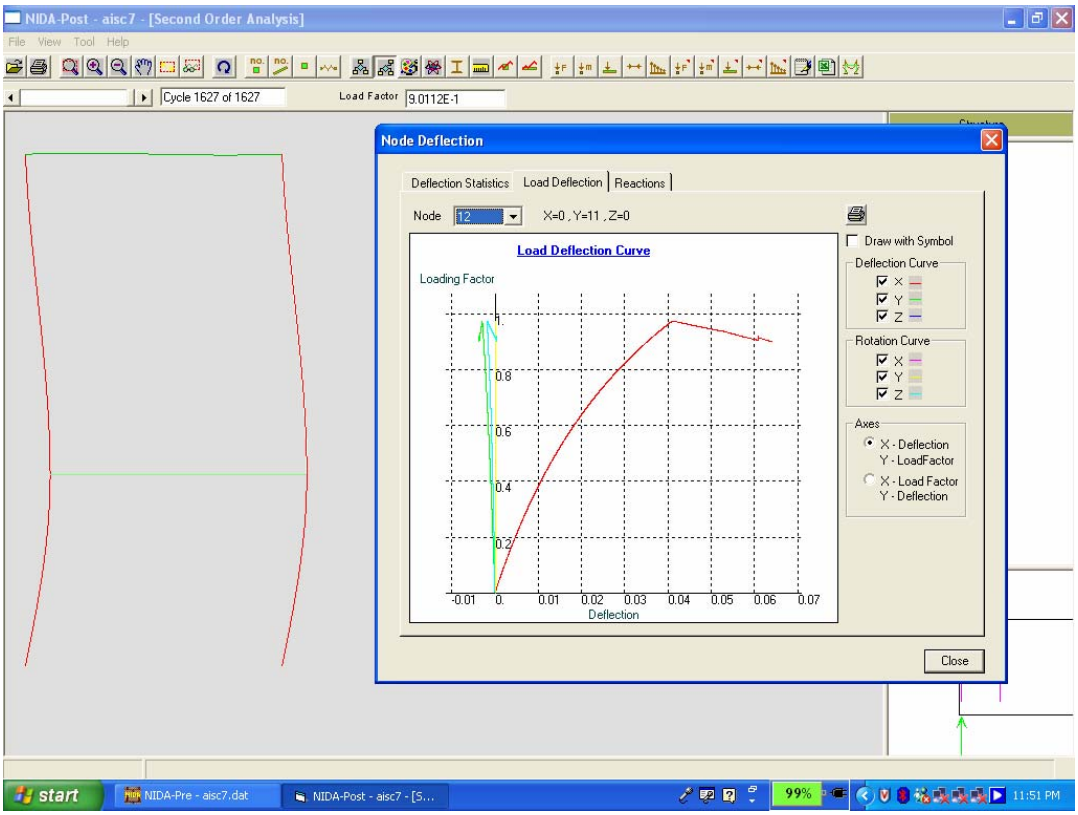

Figure 10. Load vs deflection curve of unbraced but tied-at-top frame

From the results of this example, it can be seen that inclusion of initial imperfection is important in determining the resistance of a structure. The recommended use of 0.5% of storey height for permanent structures and 1% for temporary structure are commonly used in practice. Engineers should inspect structures against excessive imperfections to prevent unexpected collapse.

Example 2 Advanced analysis of a bracket-ball stadium

A bracket ball stadium of 48m(L)x40.4m(W)x16.7m(H) is designed by the advanced analysis. The steel grade used is S355J and all are hollow sections. The computer model of the structure is indicated in Figure 11 with photographs on the structure during early and late construction stages are shown in Figures 12 and 13. All connections between members are welded and assumed rigid in the analysis model.

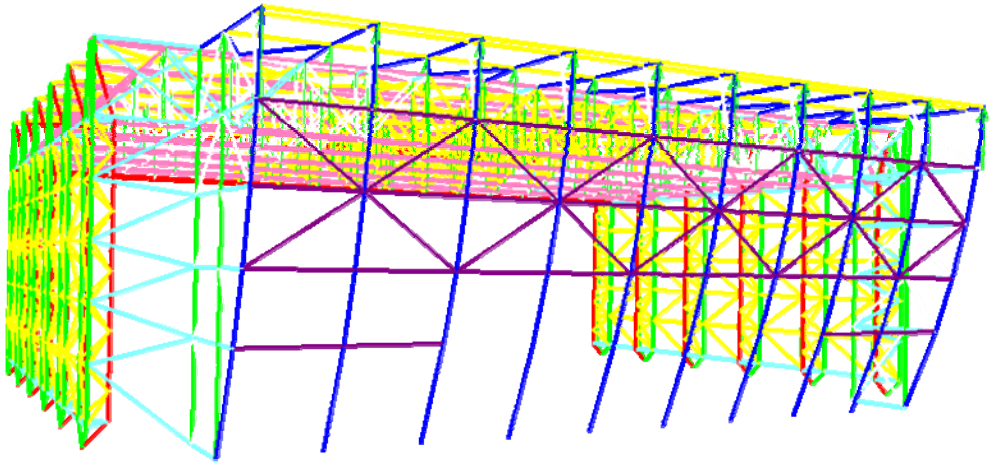

Figure 11. Computer model of the stadium

For simplicity, only the load case consisted of live loads of 1.5 kPa, dead loads of self weigh plus 0.75 kPa for accessories and wind load parallel to the longer dimension is considered. All load factors used are 1.2. The second-order plastic hinge analysis is used in the present design. Notional force is not applied to the frame as it is smaller than wind load.

Figure 12. Stadium under construction

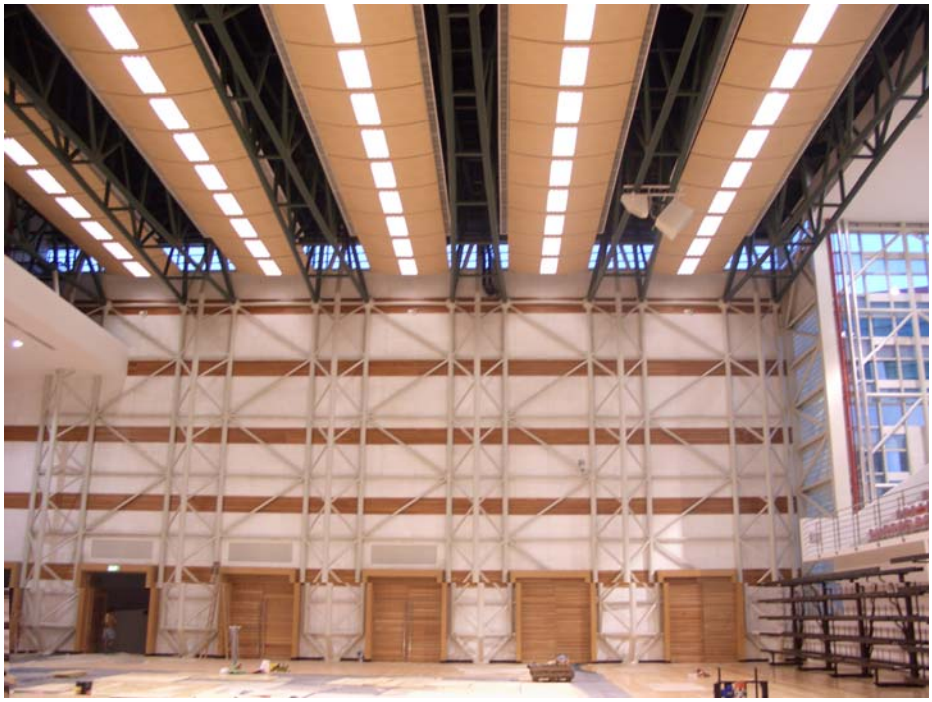

Figure 13. Inside view of the completed stadium

First plastic hinge is formed at 80% of the design load and the deflection curves become flat at a load factor of 1.06 of the design load. This implies around 26% strength reserve can be obtained when advanced or second-order plastic hinge analysis is used. Figure 14 shows the red members possessing plastic hinges at the maximum load factor.

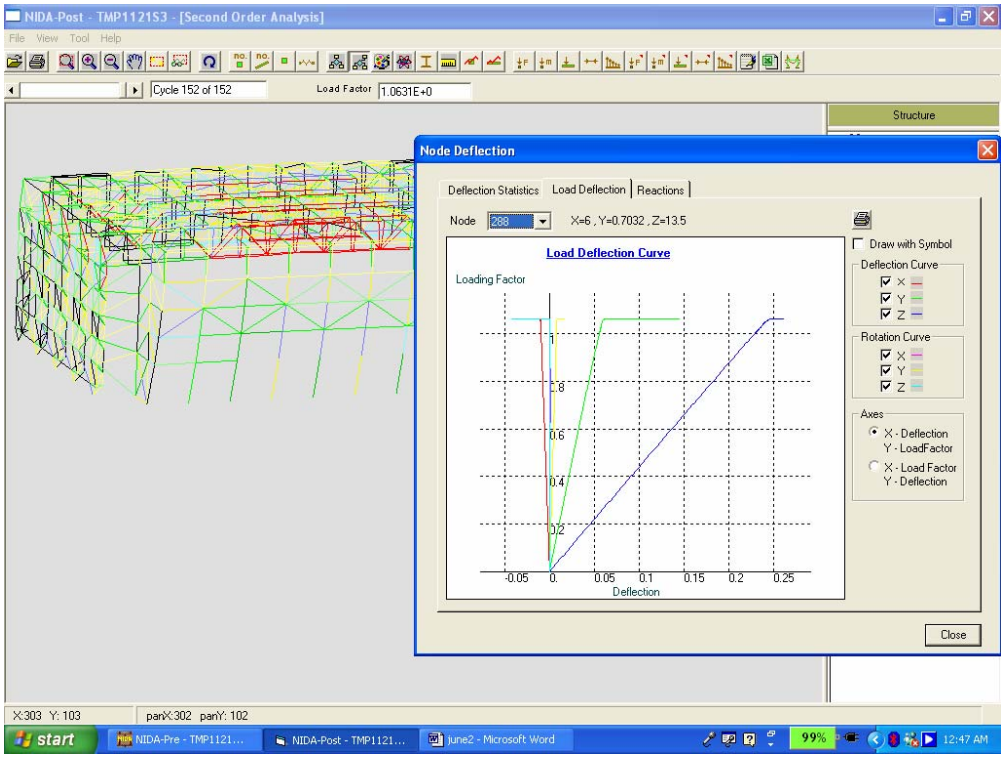

Figure 14. Plot for maximum load of the stadium indicating around 20% plastic strength reserve after the first plastic hinge

When using the elastic or first plastic hinge analysis, engineers are frustrated when an obviously redundant member fails in section capacity check but the first plastic hinge design does not permit further increase in design load. Significant gain in economy can be achieved if we fix the plastic strength of the member and continue the incremental load analysis. More importantly, material used for constructing the frame can be better distributed when the ultimate behaviour is known. This influence of a member yielding may be detrimental for determinate structures such as the frame in example 1 and the level of structural robustness can be assessed scientifically by the present design method.

Furthermore, the design speed is significantly improved by the present method since one needs not assume effective length factor (L_e/L) for each member for safety and economy. The complete analysis and design process take 2 minutes and 12 seconds for a load case when using a portable personal computer of 1.6 GHz and the computer time will obviously be further reduced when faster computers are used and available.

When using the first order linear analysis with all members having an effective length factor (L_e/L) of 1.0 which is a normal value adopted by engineers when buckling mode is uncertain, the design load resistance factor is only 0.46 of the design load. This is significantly less than the first-plastic hinge load of 0.80 and the collapse load factor of 1.06.

6. CONCLUSIONS

This paper presents an alternative and robust practical design method allowing for moment re-distribution after the first plastic hinge in steel structures. The method has been applied to accurate and reliable buckling analysis and design of real steel structures of moderate size and for design allowing for plastic strength reserve after the first plastic hinge.

As all structures have different levels of integrity, robustness and plastic strength reserve, the proposed method can be used to identify the ultimate collapse strength instead of the strength at first-plastic moment in a structure and to improve building scheme, as well as to enhance safety and economy through better understanding of structural behaviour at various limit states.

The authors further suggested no yielding and excessive deflection should be allowed at working or serviceability limit load and the structure should not collapse under the factored ultimate limit load. The computer method for determination of this collapse load allowing for the effects of member buckling, system instability, and formation of plastic hinges is detailed in this paper with an illustrative example of practical application.

From the authors' experience designing a number of steel structures, the "advanced analysis" was noted to be more efficient and convenient. The time required for assessing the effective length factor (L_e/L) for all compression members is saved. In some cases, the effective length factor (L_e/L) may be impossible to determine using code method. However, it appears that most engineers may require to attend an additional course on training of concept and computational skill on non-linear second-order and advanced analysis, which is not covered by general civil engineering courses.

7. ACKNOWLEDMENT

The first author would like to express his sincere thanks to Mr. Eddie Wong of Eddie Wong and Associates Limited for his kind permission of using one of the steel structures constructed for the East Asian Game in Macau as the second example as an illustrative example in this paper.

REFERENCES

[1] European Standard, Eurocode 3, “Design of steel structures”, En1993-3-1-1, 2003.

[2] British Standards Institution, BS5950, “Structural Use of Steel in Building”, Part 1, 2000.

[3] Australian Standards AS4100, “Steel Structures”, Standards Association of Australia, Sydney, Australia, 1996.

[4] Chen, W.F. and Lui, E.M., “Stability design of steel frames”, CRC, Boca Raton, 1991, pp.380.

[5] Liew, J.Y.R., White, D.W. and Chen, W.F., “National load plastic-hinge method for frame design”, Journal of Structural Engineering, ASCE, 1990, 120(5), pp.1434-1454.

[6] White, D.W. and Hajjar, J.F., “Buckling Models and Stability Design of Steel Frames: a Unified Approach”, Journal of Constructional Steel Research, 1997, 42(3), pp.171-207.

[7] Barreto, V. and Camotim, D., “Computer-Aided Design of Structural Steel Plane Frames According to Eurocode 3”, Journal of Constructional Steel Research, 1998, 46(1-3), pp.367-368.

[8] Liew, J.Y.R., Chen, W.F., Chen, I.H., “Advanced inelastic analysis of frame structures”, Journal of Constructional Steel Research, 2000, 55(1-3), pp.245-265.

[9] Xu, L., “The buckling loads of unbraced PR frames under non-proportional loading”, Journal of Constructional Steel Research, 2002, 58(4), pp.443-465.

[10] Li, G.Q. and Li, J.J., “A tapered Timoshenko-Euler beam element for analysis of steel portal frames”, Journal of Constructional Steel Research, 2002, 58(12), pp.1531-1544.

[11] Goncalves, R. and Camotim, D., “Design of plane steel frames – towards a rational approach”, Advanced Steel Construction, June, 2005, 1(1), pp.105-128.

[12] Chan, S.L. and Zhou, Z.H., “Non-linear integrated design and analysis of skeletal structures by 1 element per member”, Engineering Structures, 2000, 22, pp.246-257.

[13] Chan, S.L. and Cho, S.H., “Second-order P-delta analysis and design of angle trusses allowing for imperfections and semi-rigid connections”, Advanced Steel Construction, June, 2005, 1(1), pp.151-171.

[14] Gu, J.X. and Chan, S.L., “Design of frames with imperfect members and global geometry by second-order analysis with section capacity check”, International Journal for Numerical Methods in Engineering, 2005, 62, pp.601-615.

[15] Buildings Department, “Code of Practice for the Structural Use of Steel”, Hong Kong, 2005.

[16] Zhou, Z.H. and Chan, S.L., “Elastoplastic and large deflection analysis of steel frames by one element per member. Part 1: One hinge along member”, Journal of Structural Engineering, ASCE, 2004, 130(4), pp.538-544.

ADVANCED STEEL CONSTRUCTION

An International Journal

Volume 1 Number 2 September 2005

CONTENTS

Technical Papers